

Nanocrystals for Electronic and Optoelectronic Applications

Guest Editors: Ting Zhu, Sylvain G. Cloutier, Iliia Ivanov,
Kenneth L. Knappenberger Jr., Istvan Robel, and Fan Zhang





Nanocrystals for Electronic and Optoelectronic Applications

Nanocrystals for Electronic and Optoelectronic Applications

Guest Editors: Ting Zhu, Sylvain G. Cloutier, Ilia Ivanov, Kenneth L. Knappenberger Jr., Istvan Robel, and Fan Zhang



Copyright © 2012 Hindawi Publishing Corporation. All rights reserved.

This is a special issue published in "Journal of Nanomaterials." All articles are open access articles distributed under the Creative Commons Attribution License, which permits unrestricted use, distribution, and reproduction in any medium, provided the original work is properly cited.

Editorial Board

Katerina Aifantis, Greece
Nageh K. Allam, USA
Margarida Amaral, Portugal
Xuedong Bai, China
L. Balan, France
Enrico Bergamaschi, Italy
Theodorian Borca-Tasciuc, USA
C. Jeffrey Brinker, USA
Christian Brosseau, France
Xuebo Cao, China
Shafiul Chowdhury, USA
Kwang-Leong Choy, UK
Cui ChunXiang, China
Miguel A. Correa-Duarte, Spain
Shadi A. Dayeh, USA
Ali Eftekhari, USA
Claude Estournes, France
Alan Fuchs, USA
Lian Gao, China
Russell E. Gorga, USA
Hongchen Chen Gu, China
Mustafa O. Guler, Turkey
John Zhanhu Guo, USA
Smrati Gupta, Germany
Michael Harris, USA
Zhongkui Hong, USA
Michael Z. Hu, USA
David Hui, USA
Y.-K. Jeong, Republic of Korea
Sheng-Rui Jian, Taiwan
Wanqin Jin, China
Rakesh K. Joshi, India
Zhenhui Kang, China
Fathallah Karimzadeh, Iran
Alireza Khataee, Iran
Do Kyung Kim, Republic of Korea
Kin Tak Lau, Australia
Burtrand Lee, USA
Benxia Li, China
Jun Li, Singapore
Shijun Liao, China
Gong Ru Lin, Taiwan
J.-Y. Liu, USA
Jun Liu, USA
Tianxi Liu, China
Songwei Lu, USA
Daniel Lu, China
Jue Lu, USA
Ed Ma, USA
Gaurav Mago, USA
Santanu K. Maiti, Israel
Sanjay R. Mathur, Germany
A. McCormick, USA
Vikas Mittal, UAE
Weihai Ni, Germany
Sherine Obare, USA
Edward Andrew Payzant, USA
Kui-Qing Peng, China
Anukorn Phuruangrat, Thailand
Ugur Serincan, Turkey
Huaiyu Shao, Japan
Donglu Shi, USA
Suprakas Sinha Ray, South Africa
Vladimir Sivakov, Germany
Marinella Striccoli, Italy
Bohua Sun, South Africa
Saikat Talapatra, USA
Nairong Tao, China
Titipun Thongtem, Thailand
Somchai Thongtem, Thailand
Valeri P. Tolstoy, Russia
Tsung-Yen Tsai, Taiwan
Takuya Tsuzuki, Australia
Raquel Verdejo, Spain
Mat U. Wahit, Malaysia
Shiren Wang, USA
Yong Wang, USA
Ruibing Wang, Canada
Cheng Wang, China
Zhenbo Wang, China
Jinquan Wei, China
Ching Ping Wong, USA
Xingcai Wu, China
Guodong Xia, Hong Kong
Zhi Li Xiao, USA
Ping Xiao, UK
Shuangxi Xing, China
Yangchuan Xing, USA
N. Xu, China
Doron Yadlovker, Israel
Ying-Kui Yang, China
Khaled Youssef, USA
Kui Yu, Canada
William W. Yu, USA
Haibo Zeng, China
Tianyou Zhai, Japan
Renyun Zhang, Sweden
Yanbao Zhao, China
Lianxi Zheng, Singapore
Chunyi Zhi, Japan

Contents

Nanocrystals for Electronic and Optoelectronic Applications, Ting Zhu, Sylvain G. Cloutier, Ilia Ivanov, Kenneth L. Knappenberger Jr., Istvan Robel, and Fan Zhang
Volume 2012, Article ID 392742, 2 pages

Developing Quantum Dot Phosphor-Based Light-Emitting Diodes for Aviation Lighting Applications, Fengbing Wu, Dawei Zhang, Shuzhen Shang, Yiming Zhu, Songlin Zhuang, and Jian Xu
Volume 2012, Article ID 629157, 5 pages

Temperature Dependence of Electrical Characteristics of Carbon Nanotube Field-Effect Transistors: A Quantum Simulation Study, Ali Naderi, S. Mohammad Noorbakhsh, and Hossein Elahipanah
Volume 2012, Article ID 532625, 7 pages

Synthesis of SnO₂-ZnO Core-Shell Nanowires and Their Optoelectronic Properties, Ko-Ying Pan, Yu-Hung Lin, Po-Sheng Lee, Jyh-Ming Wu, and Han C. Shih
Volume 2012, Article ID 279245, 6 pages

Employing Photoassisted Ligand Exchange Technique in Layered Quantum Dot LEDs, Wenjia Hu, Shuai Gao, Paras N. Prasad, Jingkang Wang, and Jian Xu
Volume 2012, Article ID 719169, 5 pages

Facile Synthesis of Colloidal CuO Nanocrystals for Light-Harvesting Applications, Yee-Fun Lim, Joshua J. Choi, and Tobias Hanrath
Volume 2012, Article ID 393160, 6 pages

Gold Nanoparticle Sensor for the Visual Detection of Pork Adulteration in Meatball Formulation, M. E. Ali, U. Hashim, S. Mustafa, Y. B. Che Man, and Kh. N. Islam
Volume 2012, Article ID 103607, 7 pages

Fluorescent Properties of ZnO Nanostructures Fabricated by Hydrothermal Method, Zhiwei Dong, Bing Han, Shixiong Qian, and Deying Chen
Volume 2012, Article ID 251276, 5 pages

Study of Structural and Optical Properties of Zinc Oxide Rods Grown on Glasses by Chemical Spray Pyrolysis, Erdal Sonmez, Serdar Aydin, Mehmet Yilmaz, Mustafa Tolga Yurtcan, Tevhit Karacali, and Mehmet Ertugrul
Volume 2012, Article ID 950793, 5 pages

Editorial

Nanocrystals for Electronic and Optoelectronic Applications

**Ting Zhu,¹ Sylvain G. Cloutier,² Ilia Ivanov,³ Kenneth L. Knappenberger Jr.,⁴
Istvan Robel,⁵ and Fan Zhang⁶**

¹ Philips Lumileds, San Jose, CA 95131, USA

² University of Delaware, Newark, DE 19716, USA

³ Oak Ridge National Lab, Oak Ridge, TN 37831, USA

⁴ Florida State University, Tallahassee, FL 32306, USA

⁵ Los Alamos National Laboratory, Los Alamos, NM 87545, USA

⁶ Cree Inc., Santa Barbara, CA 93117, USA

Correspondence should be addressed to Ting Zhu, txz902@gmail.com

Received 23 January 2012; Accepted 23 January 2012

Copyright © 2012 Ting Zhu et al. This is an open access article distributed under the Creative Commons Attribution License, which permits unrestricted use, distribution, and reproduction in any medium, provided the original work is properly cited.

Electronic and optoelectronic devices, from computers and smart cell phones to solar cells, have become a part of our life. Currently, devices with featured circuits of 45 nm in size can be fabricated for commercial use. However, further development based on traditional semiconductor is hindered by the increasing thermal issues and the manufacturing cost. During the last decade, nanocrystals have been widely adopted in various electronic and optoelectronic applications. They provide alternative options in terms of ease of processing, low cost, better flexibility, and superior electronic/optoelectronic properties. By taking advantage of solution-processing, self-assembly, and surface engineering, nanocrystals could serve as new building blocks for low-cost manufacturing of flexible and large area devices. Tunable electronic structures combined with small exciton binding energy, high luminescence efficiency, and low thermal conductivity make nanocrystals extremely attractive for FET, memory device, solar cell, solid-state lighting/display, photodetector, and lasing applications. Efforts to harness the nanocrystal quantum tunability have led to the successful demonstration of many prototype devices, raising the public awareness to the wide range of solutions that nanotechnology can provide for an efficient energy economy. This special issue aims to provide the readers with the latest achievements of nanocrystals in electronic and optoelectronic applications, including the synthesis and engineering of nanocrystals towards the applications and the corresponding device fabrication, characterization and computer modeling.

This special issue contains eight papers, in which four papers discuss the nanocrystal applications in electronic and

optoelectronic devices. They are followed by three papers regarding the synthesis and characterization of the optical and optoelectronic properties of nanomaterials. The last one introduces an interesting application of nanoparticles in food science benefiting from their optical properties.

In the paper, “*Facile synthesis of colloidal CuO nanocrystals for light-harvesting applications*”, Y.-F. Lim et al. present a synthesis of CuO nano-crystals by a facile alcoholthermal route, which enables the processing of these materials by solution. They also demonstrate a bilayer solar cell comprising of CuO nanocrystals and phenyl-C61-butyrac acid methyl ester (PCBM) with a power conversion efficiency of 0.04%, indicating the potential of this material for light-harvesting applications.

In the paper entitled “*Developing quantum dot phosphor-based light emitting diodes for aviation lighting applications*”, J.-M. Wu et al. investigated the feasibility to use quantum dot (QD) phosphor-based LED in night vision imaging systems for aviation applications. In their proof-of-concept experiment, they have demonstrated the great potential of QD phosphor-based LEDs in cockpit illumination and back light source of monitor screens, as well as the LED indicator lights of aviation panels.

In the paper entitled “*Temperature dependence of electrical characteristics of carbon nanotube field-effect transistors: a quantum simulation study*”, S. M. Noorhakhsh et al. investigate the attributes of carbon nanotube field-effect transistors (CNTFET) in different temperatures by a 2-dimensional full quantum simulation. It has shown that temperature increase results in higher subthreshold swing and low

on-off current ratio. The results are considered to be useful for design considerations in those devices.

In the paper entitled “*Employing photo-assisted ligand exchange technique in layered quantum dot LEDs*,” W. Hu et al. present a photo-assisted ligand exchange approach to replace the oleic acid ligand molecules over PbSe quantum dots (QDs). The surface-treated QDs are used to fabricate thin-film QD-LEDs, which results in improved LED performance over the untreated QD-LEDs.

In the paper entitled “*Synthesis of SnO₂-ZnO core-shell nanowires and their optoelectronic properties*,” K.-Y. Pan et al. present a method of synthesizing core/shell semiconductor nanowires using a step-by-step atomic layer deposition process. The hybrid SnO₂-ZnO nanowires have significantly improved conductance and faster photoresponse compared to pure SnO₂ nanowires, making them more suitable for optoelectronic applications.

In the paper entitled “*Fluorescent properties of ZnO nanostructures fabricated by hydro-thermal method*,” Z. Dong et al. synthesized ZnO nanorods with mean diameter of 200 nm on different substrates by hydrothermal method. They investigated the nanorod fluorescent properties by linear and nonlinear excitation as well as Raman spectrum.

In the paper entitled “*Study of structural and optical properties of zinc oxide rods grown on glasses by chemical spray pyrolysis*,” E. Sonmez et al. investigate morphological and optical properties of zinc oxide rods prepared by spray pyrolysis. The results indicate that spray pyrolysis is a cheap and viable technique for producing high quality ZnO rods for optical applications.

In the final paper “*Gold nanoparticle sensor for the visual detection of pork adulteration in meatball formulation*,” M. E. Ali et al. use gold nanoparticles as colorimetric sensor to detect pork adulteration in beef/chicken preparations. The method is cheap, reliable, and simple, depending on the color change of 20 nm gold nanoparticles following salt addition. The result can be further confirmed by the absorption spectroscopy. The A_{1L} optical mode was found important to the fluorescent properties of ZnO materials.

*Ting Zhu
Sylvain G. Cloutier
Ilia Ivanov
Kenneth L. Knappenberger Jr.
Istvan Robel
Fan Zhang*

Research Article

Developing Quantum Dot Phosphor-Based Light-Emitting Diodes for Aviation Lighting Applications

Fengbing Wu,¹ Dawei Zhang,¹ Shuzhen Shang,¹ Yiming Zhu,¹
Songlin Zhuang,¹ and Jian Xu^{1,2}

¹Engineering Research Center of Optical Instrument and System, University of Shanghai for Science and Technology, No. 516 JunGong Road, Shanghai 200093, China

²Department of Engineering Science and Mechanics, Pennsylvania State University, University Park, PA 16802, USA

Correspondence should be addressed to Jian Xu, jianxu@engr.psu.edu

Received 10 October 2011; Revised 4 January 2012; Accepted 4 January 2012

Academic Editor: Sylvain G. Cloutier

Copyright © 2012 Fengbing Wu et al. This is an open access article distributed under the Creative Commons Attribution License, which permits unrestricted use, distribution, and reproduction in any medium, provided the original work is properly cited.

We have investigated the feasibility of employing quantum dot (QD) phosphor-based light-emitting diodes (LEDs) in aviation applications that request Night Vision Imaging Systems (NVIS) compliance. Our studies suggest that the emerging QD phosphor-based LED technology could potentially be superior to conventional aviation lighting technology by virtue of the marriage of tight spectral control and broad wavelength tunability. This largely arises from the fact that the optical properties of semiconductor nanocrystal QDs can be tailored by varying the nanocrystal size without any compositional changes. It is envisioned that the QD phosphor-based LEDs hold great potentials in cockpit illumination, back light sources of monitor screens, as well as the LED indicator lights of aviation panels.

1. Introduction

The essence of Night Vision Imaging Systems (NVIS) compliance in aviation lighting technology is to ensure that the pilots can successfully operate avionic systems when wearing NVIS goggles under cockpit illumination conditions. This paper reports the feasibility of employing quantum dot (QD) phosphor-based light-emitting diodes (LEDs) in aviation applications that request Night Vision Imaging Systems (NVIS) compliance.

NVIS technology refers to the application of photoelectron systems that perform image information transformation, enhancement, processing, display, and other physical processes. At the heart of such a system is an image intensifier which enhances the infrared signals under low-level-light (LLL) conditions. The third generation NVIS uses Gallium Arsenide photocathode image enhancement tube. The maximum response falls in the near-infrared wavelength. A typical product is the AN/AVS-6 LLL night vision system [1]. The system needs to install filters to reduce the influence of visible light. The filters can be divided into two generic types,

that is, Class A with the maximum response wavelengths between 625~930 nm and Class B with the maximum response wavelengths between 665~930 nm [2].

While pilots rely on the visible illumination to read aviation panels and display screens in cockpits, the light sources also produce some radiation in near-infrared (IR) regime [3]. Although the influence of visible light to AN/AVS-6 has been greatly reduced by employing Class A or B filters, the infrared radiation from the cockpit light sources often overlaps with the NVIS spectral response. The near-IR radiance entering the aperture of pilots' NVIS goggles will severely compromise the use of NVIS, making the goggles glaring, and sometimes even burning the image intensifier tube. It is therefore necessary to lower the degree of near-infrared radiation significantly using NVIS-compatible lighting technology.

The aviation standard usually uses a set of parameters to characterize the cockpit lighting for NVIS compatibility, that is, NVIS radiance, color limits, and visible light transmittance [3]. Among them, the NVIS radiance and color limits are the most critical indicators.

The NVIS radiance can always be calculated by the following formula:

$$\text{NVIS radiance (NR}_{A \text{ or } B}\text{) at specified luminance} \\ = S \int_{450}^{930} G_{A \text{ or } B}(\lambda)N(\lambda)d\lambda, \quad (1)$$

where $G_A(\lambda)$ = relative NVIS response of Class A equipment, $G_B(\lambda)$ = relative NVIS response of Class B equipment, $N(\lambda)$ = spectral radiance of lighting component ($W/\text{sr} \times \text{cm}^2 \times \text{nm}$), S = scaling factor.

The basic requirements of NVIS radiance is $-1.0 \leq \text{NR} \leq 1.7E - 10$.

The colors and color limits are determined by the following formula:

$$(u' - u'_1)^2 + (v' - v'_1)^2 \leq r^2, \quad (2)$$

where u' & v' = 1976 UCS chromaticity coordinates of the test article, u'_1 & v'_1 = 1976 UCS chromaticity coordinates of the center point of the specified color area, r = radius of the allowable circular area on the 1976 UCS chromaticity diagram for the specified color.

These lighting colors and limits are designated as “NVIS GREEN A,” “NVIS GREEN B,” “NVIS YELLOW,” “NVIS RED,” and “NVIS WHITE” [3], and NVIS white is the most common color of the light sources in aviation applications.

Colloidal compound QDs have recently been introduced to the white LED technology as a new family of phosphor materials with many superior properties [4–7]. Due to strong quantum confinement, semiconductor QDs, such as core/shell CdSe/(Zn, Cd)S QDs, are characterized by sharp exciton absorption features, extremely high luminescence efficiency (~90–95%), and size-tunable emission color spanning the entire visible spectrum [8]. QDs of the same chemical composition and different size can therefore be employed to provide multiple spectral components in white LEDs output, with improved color qualities and aging performance [9]. Perhaps the most significant potential of QD phosphors lies in the fact that the extremely narrow emission band of monodisperse QDs populations (FWHM~15–30 nm) [10]. II–VI compound-based QD-LEDs have produced color-saturated emissions of much higher spectral purities than those of liquid crystal displays (LCDs) and organic light emitting diodes (OLEDs) and even 30% greater than bulky cathode ray tubes (CRTs) that are still favored for their excellent color rendition. It is therefore possible to fine tailor the color rendering index (CRI), color temperature as well as the NVIS radiance of white QD phosphor-based LEDs in order to meet the strict spectral requirements in a variety of special LED applications.

In the present work, white emission from QD phosphor-based LEDs is achieved by depositing a layer of solution-processed QD film, composed of multi-color Cd(S, Se)/(Zn, Cd)S quantum dots, on top of the emissive surfaces of blue-emitting nitride LEDs [11–15]. Unlike traditional fluorescent lamps where only one type of UV-sensitive broadband phosphor is employed, QD phosphor-based LEDs produce white light by mixing two compensating colors (blue and yellow/orange) or several primary colors (red, yellow, green,

and blue). By varying the nanocrystal sizes or adjusting the compound composition, the luminescence spectrum of the monodisperse quantum dots can cover the entire visible light spectrum. It is therefore possible to obtain spectrally-adjustable white light QD phosphor-based LEDs by integrating multicolor QD phosphors in the LED device. Finally, by engineering the surfactant molecules of the nanocrystals, it is possible to further enhance the fluorescence quantum yield and make the QDs more photochemical stable, leading to enhanced efficiency and output luminance of white QD phosphor-based LEDs [16, 17].

2. Methods

When QD phosphor-based LEDs are used as the light sources in the aircraft cockpit, it is important to make the LED output compatible with NVIS requirements. This sets rigorous limits on the emission spectra of the LEDs, especially on the reddish side of the band. For traditional white fluorescent lighting systems employed in the aircraft cockpit, the NVIS Radiance Class B (NRB) is measured $\sim 1 \times 10^{-6}$ (0.1 ft), which is much higher than the specified threshold ($2.2E - 9$) of NVIS white. The high NRB of the traditional lighting systems arises from the broadband emission of the UV-sensitive phosphors and can only be reduced via filters [18–22]. On the other hand, the NRB of the existing commercial white LEDs falls in the range of $1 \times 10^{-7} \sim 1 \times 10^{-8}$, which is still one or two orders of magnitude lower than the NVIS threshold. This arises from the fact that the downconversion of blue radiation to yellow/green and red in conventional LEDs was accomplished with $\text{Y}_3\text{Al}_5\text{O}_{12}:\text{Ce}^{3+}$ and Eu^{2+} doped nitridosilicates phosphors coated on top of the InGaN QW LEDs for color mixing in the white output. While the luminescence of the blue-sensitive $\text{Y}_3\text{Al}_5\text{O}_{12}:\text{Ce}^{3+}$ and Eu^{2+} doped nitridosilicates phosphors exhibits spectrally narrower band than the UV-sensitive phosphors in fluorescence lamps, there is still an appreciable near-IR portion ($\lambda \geq 650 \text{ nm}$) in the luminescence spectrum of the blue-sensitive phosphors. Hence it is still necessary to implement filtering techniques with conventional white LEDs in order to meet the NVIS requirement.

By selecting the QD size, it is possible to precisely control the residual emission of the white light QD phosphor-based LEDs in near-IR regime. Hence it is feasible to fabricate high-luminous-efficiency white QD-LED chips that are compatible with NVIS without any filters. The spectral overlap between the output of QD phosphor-based LEDs and that of the night vision systems can be minimized. These QD phosphor-based LEDs hold great potentials in cockpit illumination, back light sources of monitor screens, as well as the LEDs indicator lights of aviation panels.

2.1. Calculation. In the present study, the NRB of a QD phosphor-based LED was calculated to illustrate the NVIS-compatibility of QD phosphor-based LEDs. In this device, the blue emission of 450 nm-peak wavelength of an InGaN QW LED is mixed with the yellow–orange luminescence of CdSe/CdS/ZnS core-shell QDs to produce “complimentary white” in the QD phosphor-based LED output. Figure 1(a)

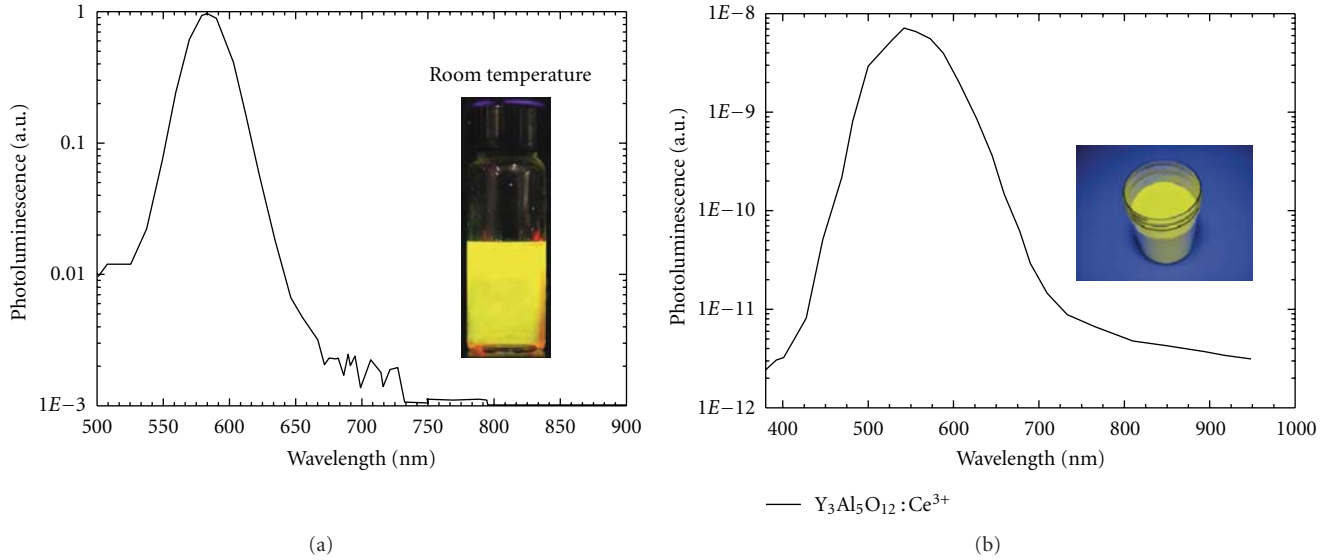


FIGURE 1: (a) The luminescence spectrum of yellow CdSe/CdS/ZnS core-shell QDs that is used in the calculation. (b) The luminescence spectra of $Y_3Al_5O_{12}:Ce^{3+}$ phosphor that is used in the calculation.

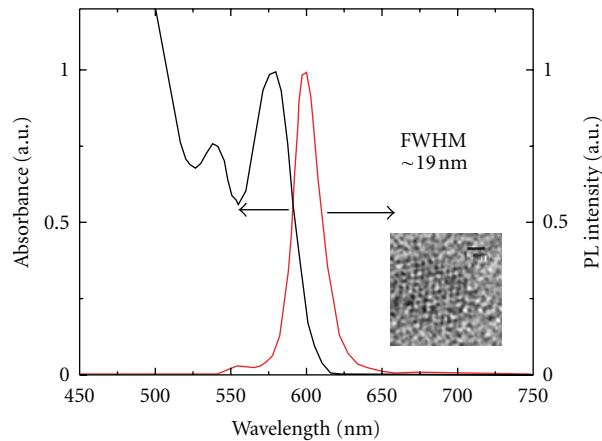


FIGURE 2: Absorption and luminescence spectra of orange-red-emitting CdSe/CdS/ZnS core-shell QDs used in the proof-of-concept experiment. The inset shows the HRTEM image of an individual QD.

shows the luminescence spectrum of the QDs employed in the calculation. For the sake of comparison, the fluorescence spectrum of $Y_3Al_5O_{12}:Ce^{3+}$ phosphor is also plotted in Figure 1(b). Calculation using (1) shows that the NVIS radiance for Class B detection systems (NRB) of the QD phosphor-based LEDs can be as low as $4E-10$ at 0.1 ft brightness, which is far below the threshold radiance for Night Vision Imaging Systems (NVIS). Even at a high brightness (0.5 ft), the NRB ($2.0E-9$) of QD phosphor-based LEDs still complies with the NVIS requirement. In comparison, the NRB of an LED with $Y_3Al_5O_{12}:Ce^{3+}$ phosphor was calculated to be $\sim 6 \times 10^{-8}$ at 0.1 ft brightness.

2.2. Experiments. In a proof-of-concept experiment, we have fabricated QD phosphor-based LEDs by mist-depositing orange-emitting CdSe/CdS/ZnS core-shell QDs over the

emissive surface of InGaN QW LEDs [23]. The QDs employed in our study are orange-red CdSe/CdS/ZnS core-shell structures, which were synthesized following the method developed by Dr. Peng's group (CdSe-(Cd, Zn)S) [24]. Nearly monodisperse QDs were produced and stored in toluene solutions. Transmission electron microscopy was conducted to determine the lattice structure and dimensions of the QDs as shown in the inset of Figure 2. Nearly identical spherical crystalline particles are observed. The particles in the high resolution TEM micrographs show well-resolved lattice fringes with a measured lattice spacing similar to the bulk CdSe structure. The high-quality of the QDs was also manifested by the sharp exciton absorption features and narrow FWHM bandwidth of photoluminescence (~ 19 nm) of the QDs (Figure 2).

The QDs were dispersed in toluene solution for mist deposition, and the thickness of the QDs was precisely

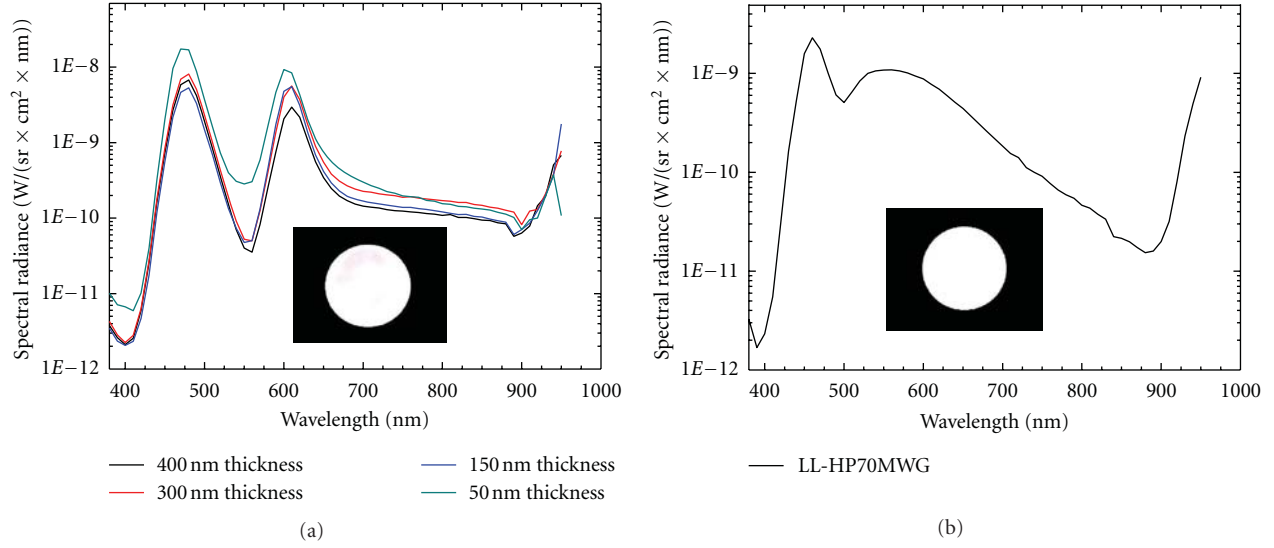


FIGURE 3: (a) The output spectra of QD phosphor-based LEDs with different QD film thicknesses. The inset shows a portion of the emissive surface of the white QD phosphor-based LED. (b) The output spectrum of a commercial LED. The inset shows a portion of the white emissive surface of the commercial LED.

TABLE 1: The NVIS radiance of a QD-LED and a commercial white LED.

Model	UCS 1976 chromaticity coordinates	Tested NVIS ($W/(sr \times cm^2 \times nm)$)	Specified NVIS ($W/(sr \times cm^2 \times nm)$)
QD-LEDs Thickness ~400 nm	$u' = 0.2315$ $v' = 0.3815$	NRB = $1.652E - 08$	
QD-LEDs Thickness ~300 nm	$u' = 0.2665$ $v' = 0.4089$	NRB = $1.673E - 08$	NRB $\leq 1.0E - 09$
QD-LEDs Thickness ~150 nm	$u' = 0.2979$ $v' = 0.4368$	NRB = $1.335E - 08$	
QD-LEDs Thickness ~50 nm	$u' = 0.2481$ $v' = 0.3918$	NRB = $9.420E - 09$	
Commercial White LED (LL-HP70MWG)	$u' = 0.1950$ $v' = 0.4626$	NRB = $1.300E - 07$	NRB $\leq 1.0E - 09$

controlled by varying the deposition time, the flux of the carrier gas, and the concentration of the QDs solution. A deposition rate of ~ 100 nm/min for the formation of QDs films over the emissive surface of nitride LEDs is used in the present work. In processing white QD-LEDs, a type of InGaN-QW-based blue chips was used with a peak emission at $\lambda \sim 469$ nm, and a layer of orange-red QDs was deposited as the phosphor to produce complimentary white output. For the measurement, a Night Vision Display Test and Measurement System (OL 770-NVS, Gooch & Housego) was utilized to characterize the output spectra and to determine the NVIS radiance of the QD phosphor-based LED devices under study. Figure 3(a) plots the output spectra of QD phosphor-based LEDs configured with 50 nm, 150 nm, 300 nm, and 400 nm-thick QD phosphor films, respectively. The measured NVIS radiance was summarized in Table 1.

For comparison, we also measured the spectral response and NVIS radiance of a commercial white LED (Lucky Light LL-HP70MWG) that use ceramic phosphor ($Y_3Al_5O_{12}:Ce^{3+}$), which have also been included in Figure 3(b) and Table 1.

3. Results and Discussion

It is evident from our measurement results that the NRB of the commercial white LEDs falls in the range of 10^{-7} , which is significantly off the NVIS specification without filters. On the other hand, the NVIS radiance of QD phosphor-based LEDs was found as low as $9.420E - 09$ for a QD thickness of 50 nm, which is more than an order of magnitude lower than that of commercial white light LEDs (1.3×10^{-7}). While it is still slightly higher than the NVIS requirement, it is envisioned that NRB of QD phosphor-based LEDs can be further

reduced by blue shifting the luminescence wavelength of the deposited QD phosphors from orange-red into yellow-orange or even yellow regime. As the spectral maxima of the QDs are shifted further away from the near-IR regime, there will be reduced overlap between the QD-LED emission and NVIS spectral response, and hence the reduced NRB value. Our measurement results also suggest the NVIS radiance increases along with the increasing thickness of the QD film. It is suspected that reabsorption-induced red shift of QD emission becomes more serious in thicker QD films, which accounts for the observed increase in NVIS radiance. Further investigation is currently underway to verify this hypothesis.

4. Conclusions

In summary, our calculation and proof-of-concept experiment suggest that white QD phosphor-based LEDs can be tailored to exhibit higher compatibility with NVIS than commercial LEDs. It is therefore envisioned that the QD phosphor-based LEDs hold great potentials in cockpit illumination, back light sources of monitor screens, as well as the LED indicator lights of aviation panels.

Acknowledgments

The work at University of Shanghai for Science and Technology is supported by NSFC under Grant 61078007, Shanghai Municipal Education Commission and Shanghai Education Development Foundation under Shu Guang Project 10SG46, Science and Technology Commission of Shanghai Municipality under Grants 11530502200 and 1052nm07100, and Program for New Century Excellent Talents in University. The work at the Penn State University is being supported by the National Science Foundation under Grants CMMI-0729263 and ECCS 0824186.

References

- [1] P. Wan-cong, *Foreign Military Low-Light-Level (LLL) Night Vision Equipment*, Weapon Industry Press, Beijing, China, 1991.
- [2] Armament Standard Press of Commission of Science Technology and Industry for National Defense, *GJB1394-92 Aircraft NVIS-Compatible Interior Lighting System*, Armament Standard Press of Commission of Science Technology and Industry for National Defense, Beijing, China, 1994.
- [3] Department of Defense, *MIL-STD-3009 Lighting, Aircraft, Night Vision Imaging System (NVIS) Compatible*, Department of Defense, Washington, DC, USA, 2001.
- [4] S. V. Kershaw, M. Harrison, A. L. Rogach, and A. Kornowski, "Development of IR-emitting colloidal II–VI quantum-dot materials," *IEEE Journal on Selected Topics in Quantum Electronics*, vol. 6, no. 3, pp. 534–543, 2000.
- [5] S. Coe-Sullivan, W.-K. Woo, J. S. Steckel, M. Bawendi, and V. Bulović, "Tuning the performance of hybrid organic/inorganic quantum dot light-emitting devices," *Organic Electronics*, vol. 4, no. 2–3, pp. 123–130, 2003.
- [6] J. S. Steckel, P. Snee, S. Coe-Sullivan et al., "Color-saturated green-emitting QD-LEDs," *Angewandte Chemie—International Edition*, vol. 45, no. 35, pp. 5796–5799, 2006.
- [7] J. S. Steckel, J. P. Zimmer, S. Coe-Sullivan, N. E. Stott, V. Bulović, and M. G. Bawendi, "Blue luminescence from (CdS)ZnS core-shell nanocrystals," *Angewandte Chemie—International Edition*, vol. 43, no. 16, pp. 2154–2158, 2004.
- [8] Q. Sun, Y. A. Wang, L. S. Li et al., "Bright, multicoloured light-emitting diodes based on quantum dots," *Nature Photonics*, vol. 1, no. 12, pp. 717–722, 2007.
- [9] H. S. Chen, C. K. Hsu, and H. Y. Hong, "InGaN–CdSe–ZnSe quantum dots white LEDs," *IEEE Photonics Technology Letters*, vol. 18, no. 1, pp. 193–195, 2006.
- [10] S. Chaudhary, M. Ozkan, and W. C. W. Chan, "Trilayer hybrid polymer-quantum dot light-emitting diodes," *Applied Physics Letters*, vol. 84, no. 15, pp. 2925–2927, 2004.
- [11] M. Achermann, M. A. Petruska, D. D. Koleske, M. H. Crawford, and V. I. Klimov, "Nanocrystal-based light-emitting diodes utilizing high-efficiency nonradiative energy transfer for color conversion," *Nano Letters*, vol. 6, no. 7, pp. 1396–1400, 2006.
- [12] M. C. Schlamp, X. Peng, and A. P. Alivisatos, "Improved efficiencies in light emitting diodes made with CdSe(CdS) core/shell type nanocrystals and a semiconducting polymer," *Journal of Applied Physics*, vol. 82, no. 11, pp. 5837–5842, 1997.
- [13] B. O. Dabbousi, M. G. Bawendi, O. Onitsuka, and M. F. Rubner, "Electroluminescence from CdSe quantum-dot/polymer composites," *Applied Physics Letters*, vol. 66, pp. 1316–1318, 1995.
- [14] S. Coe, W.-K. Woo, M. Bawendi, and V. Bulović, "Electroluminescence from single monolayers of nanocrystals in molecular organic devices," *Nature*, vol. 420, no. 6917, pp. 800–803, 2002.
- [15] S. Chaudhary, M. Ozkan, and W. C. W. Chan, "Trilayer hybrid polymer-quantum dot light-emitting diodes," *Applied Physics Letters*, vol. 84, no. 15, pp. 2925–2927, 2004.
- [16] H. Yang, P. H. Holloway, and B. B. Ratna, "Photoluminescent and electroluminescent properties of Mn-doped ZnS nanocrystals," *Journal of Applied Physics*, vol. 93, no. 1, pp. 586–592, 2003.
- [17] C. B. Murray, C. R. Kagan, and M. G. Bawendi, "Synthesis and characterization of monodisperse nanocrystals and close-packed nanocrystal assemblies," *Annual Review of Materials Science*, vol. 30, pp. 545–610, 2000.
- [18] V. I. Klimov, *Semiconductor and Metal Nanocrystals Synthesis and Electronic and Optical Properties*, Marcel Dekker, New York, NY, USA, 1st edition, 2004.
- [19] Y. Xuan, D. Pan, N. Zhao, X. Ji, and D. Ma, "White electroluminescence from a poly(N-vinylcarbazole) layer doped with CdSe/CdS core-shell quantum dots," *Nanotechnology*, vol. 17, no. 19, pp. 4966–4969, 2006.
- [20] G. Moeller and S. Coe-Sullivan, "Quantum-dot light-emitting devices for displays," *Information Display*, vol. 22, no. 2, pp. 2–6, 2006.
- [21] P. O. Anikeeva, J. E. Halpert, M. G. Bawendi, and V. Bulović, "Electroluminescence from a mixed red-green-blue colloidal quantum dot monolayer," *Nano Letters*, vol. 7, no. 8, pp. 2196–2200, 2007.
- [22] R. D. New, R. L. Burgess, and S. K. Burgess, "Infrared filter system for fluorescent lighting," US, 0252507, 2004.
- [23] T. Zhu, K. Shanmugasundaram, F. Zhang et al., "Mist fabrication of light emitting diodes with colloidal nanocrystal quantum dots," *Applied Physics Letters*, vol. 92, no. 2, Article ID 023111, 3 pages, 2008.
- [24] X. Peng and L. Qu, "Control of photoluminescence properties of CdSe nanocrystals in growth," *Journal of the American Chemical Society*, vol. 124, no. 9, pp. 2049–2055, 2002.

Research Article

Temperature Dependence of Electrical Characteristics of Carbon Nanotube Field-Effect Transistors: A Quantum Simulation Study

Ali Naderi,¹ S. Mohammad Noorbakhsh,² and Hossein Elahipanah²

¹Electrical Engineering Department, Semnan University, Semnan, Iran

²Department of Electrical Engineering, Boroujen Branch, Islamic Azad University, Boroujen, Iran

Correspondence should be addressed to Hossein Elahipanah, elahipanah@ieee.org

Received 20 July 2011; Revised 15 December 2011; Accepted 3 January 2012

Academic Editor: Ilia Ivanov

Copyright © 2012 Ali Naderi et al. This is an open access article distributed under the Creative Commons Attribution License, which permits unrestricted use, distribution, and reproduction in any medium, provided the original work is properly cited.

By developing a two-dimensional (2D) full quantum simulation, the attributes of carbon nanotube field-effect transistors (CNTFETs) in different temperatures have been comprehensively investigated. Simulations have been performed by employing the self-consistent solution of 2D Poisson-Schrödinger equations within the nonequilibrium Green's function (NEGF) formalism. Principal characteristics of CNTFETs such as current capability, drain conductance, transconductance, and subthreshold swing (SS) have been investigated. Simulation results present that as temperature raises from 250 to 500 K, the drain conductance and on-current of the CNTFET improved; meanwhile the on-/off-current ratio deteriorated due to faster growth in off-current. Also the effects of temperature on short channel effects (SCEs) such as drain-induced barrier lowering (DIBL) and threshold voltage roll-off have been studied. Results show that the subthreshold swing and DIBL parameters are almost linearly correlated, so the degradation of these parameters has the same origin and can be perfectly influenced by the temperature.

1. Introduction

Among many materials that have been proposed to supplement and, in the long run, possibly succeed silicon as a basis for nanoelectronics, carbon nanotubes (CNTs) have attracted the most attention due to their extraordinary electronic and optical properties [1–3]. In addition to the efforts to develop new electronic devices, direct bandgap one-dimensional (1D) nanostructures are attracting attention because of the desire to base both electronic and optoelectronic technologies on the same material [1]. Among the different 1-D materials, single-walled CNTs [2] have desirable and distinctive device properties. In particular, electronic transport properties of single-wall CNTs have attracted considerable experimental and theoretical interest [4–10]. For example, CNT field effect transistors (CNTFETs) have generated considerable interest in the past few years because of their quasi-ideal electronic properties and have recently reached a high level of performance [11–14]. Transistor devices made of semiconductor single-wall CNT [2] can be considered as simple silicon MOS field-effect transistors with the silicon material replaced by the carbon nanotube structures. These devices are one of the current leading technologies to replace MOSFETs [15–17].

The MOSFET device characteristics and circuit behavior that changes with the variation in temperature were reported in many papers [18–23]. It is expected that the temperature plays key role in the CNTFET performance and characteristics. Hence, the CNTFET performance has to be predicted in different temperatures. According to the best of our knowledge, no comprehensive investigation on CNTFET device has been reported that includes the effects of change in temperature. Therefore, in this paper by varying temperature the attributes of these devices have been investigated. These attributes of CNTFETs in different temperatures have been investigated using two-dimensional (2D) quantum simulation. The simulations have been done by the self-consistent solution of 2D Poisson Schrödinger formalism [24]. The effects of varying temperature are investigated in terms of on-current, leakage off-current, on-/off-current ratio, transconductance characteristics, drain conductance, subthreshold swing (SS), threshold voltage roll-off, and drain-induced barrier lowering (DIBL).

2. CNTFET Structure and Simulation Method

A schematic cross-sectional view of the simulated cylindrical CNTFET is shown in Figure 1. The device has a zigzag

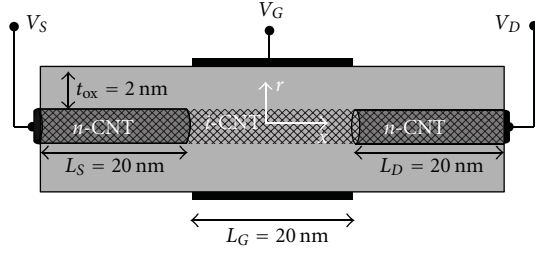


FIGURE 1: Schematic cross-sectional view of a coaxial carbon nanotube field-effect transistor (CNTFET) with cylindrical gate.

(13, 0) CNT structure with approximately 0.5 nm radius which is embedded in cylindrical gate insulator of HfO_2 with the thickness and dielectric constant (k) of 2 nm and 16, respectively [24]. The length and doping concentration of source and drain regions are 20 nm and 10^9 nm^{-1} , respectively. The channel is intrinsic and its length is 20 nm. There is no overlap between source (drain) and gate regions.

In order to simulate the device characteristics, a nonequilibrium Green's function (NEGF) formalism has been used and the Schrödinger and Poisson equations have self-consistently been solved. The band structure of CNT has been calculated by the tight-binding method. The NEGF method provides a sound approach for the simulation of the nanoscale system out of equilibrium. Poisson equation simulates gate control on channel and transport equation simulates charge transfer between source and drain. The Poisson equation is solved to obtain the electrostatic potential in the nanotube channel. By solving the Schrödinger equation within the NEGF method, the density of states and the charge of the surface of the CNT can be obtained. By using the calculated charge and solving the Poisson equation the new electrostatic potential is developed. The iteration between Poisson and Schrödinger equations continues until the self-consistency is achieved.

Because of symmetric properties, it is convenient to solve Poisson's equations in cylindrical coordinates. Since the potential and charge are invariant around the nanotube, the Poisson equation is essentially a 2D problem along the tube (z -direction) and the radial direction (r -direction) as Poisson equation is written as [25, 26]

$$\frac{\partial^2 u_j(r, z)}{\partial r^2} + \frac{1}{r} \frac{\partial u_j(r, z)}{\partial r} + \frac{\partial^2 u_j(r, z)}{\partial z^2} = \frac{-q}{\epsilon} \rho(r, z), \quad (1)$$

where $u_j(r, z)$ is the electrostatic potential, ϵ is the dielectric constant, and $\rho(r, z_j)$ is the net charge density distribution which includes the dopant density as well. The net charge distribution $\rho(r, z_j)$ is given by

$$\begin{aligned} \rho(r = r_{\text{CNT}}, z_j) &= p(z_j) - n(z_j) + N_D^+ - N_A^-, \\ \rho(r \neq r_{\text{CNT}}, z) &= 0, \end{aligned} \quad (2)$$

where r_{CNT} is CNT radius, N_D^+ and N_A^- are the ionized donor and acceptor concentrations, respectively. Then the computed electrostatic potential is used as input for the

Schrödinger equation that is solved by using NEGF formalism. The retarded Green's function is computed by the following equation [5]:

$$G_q(E) = \left[(E + i\eta^+)I - H - \sum_S - \sum_D \right]^{-1}, \quad (3)$$

where \sum_S and \sum_D are the self-energies of the source and drain respectively, η^+ is an infinitesimal positive value, E is the energy, I is the identity matrix, and H is the Hamiltonian of the CNT. The device Hamiltonian used in this paper is based on the atomistic nearest neighbor p_z -orbital tight binding approximation [27]. The cylindrical geometry of the device ensures symmetry in the angular direction, thus drastically simplifying the mode-space treatment of electron transport [28]. For an $(n, 0)$ zigzag CNT with quantum number q , the Hamiltonian matrix for the subband is given by.

$$H = \begin{bmatrix} U_1 & b_{2q} & & & \\ b_{2q} & U_2 & t & & 0 \\ & t & U_3 & b_{2q} & \\ & & \vdots & & \\ & & & b_{2q} & U_N \end{bmatrix}_{N \times N} \quad (4)$$

in which $b_{2q} = 2t \cos(\pi q/n)$, $t = 3 \text{ eV}$ is the nearest neighbor hopping parameter, and N is the total number of carbon rings along the device. Here, the diagonal element U_j corresponds to the on-site electrostatic potential along the tube surface obtained by solving the Poisson equation.

It is considered that a self-energy for semi-infinite leads as boundary conditions, and hence in these conditions, the CNT is connected to infinitely long CNTs at its ends. The source self-energy function (\sum_S) has all its entries zero except for the (1,1) element [28]:

$$\begin{aligned} \sum_S(1, 1) &= \frac{(E - U_1)^2 + t^2 + b_{2q}^2}{2(E - U_1)} \\ &\pm \frac{\sqrt{[(E - U_1)^2 + t^2 + b_{2q}^2]^2 - 4(E - U_1)^2 t^2}}{2(E - U_1)}. \end{aligned} \quad (5)$$

Similarly, \sum_D has only its (N, N) element nonzero, and it is given by an equation similar to above equation with U_1 replaced by U_N . After solving the Poisson equation and obtaining the electrostatic potential in the nanotube channel, this potential is used as input of transport equation. Self-consistency is achieved by iteration between Poisson and transport equation. The current is calculated by

$$I = \frac{2q}{h} \int T(E) [F(E - E_{\text{FS}}) - F(E - E_{\text{FD}})] dE. \quad (6)$$

This equation is Landaur-Buttiker formula. In this formula $T(E)$ is transmission coefficient, E_{FS} and E_{FD} are source and drain Fermi level, respectively, q is the electron charge, and h is Planck constant. $T(E)$ is calculated from the following equation:

$$T(E) = \text{trace}(\Gamma_S G \Gamma_D G^+), \quad (7)$$

where G is Green's function, $\Gamma_{S(D)}$ is the energy level broadening due to source (drain) contact and is calculated from below equation:

$$\Gamma_{S(D)} = i \left(\sum_{S(D)}^+ - \sum_{S(D)}^- \right) \quad (8)$$

In this paper the results are obtained from this simulation method.

3. Results and Discussion

In order to demonstrate the accuracy of quantum model, a CNTFET with the same configuration as that fabricated in [7] has been implemented. Figure 2 illustrates the simulated I_D - V_{GS} characteristic of the simulated CNTFET (line) and compares it with the experimental result (stars) in [7]. Even though the experimental data are usually highly affected by parasitic resistance, which is difficult to correctly model in the absence of enough information about experimental structure, the comparison presents that the simulation results are in reasonable agreement with the existing experimental data. The operational temperature of the transistor usually differs from room temperature due to current drive and device resistances. To investigate the influence of temperature on the attributes of CNTFETs, the temperature has been changed in the conventional operating interval from 250 to 500 K. The output characteristic of the predefined structure at border temperatures of the interval is illustrated in Figure 3. It can be seen from the figure that at low gate source voltages, for higher temperature (500 K), the drain current is higher. In spite of this, by increasing the gate source voltage, at low drain source voltage, for higher temperature (500 K) the drain current is less than lower temperature (250 K). In the saturation region by increasing the gate source voltage the drain current difference between high and low temperature reduces. It is evident from the figure that the drain current in the saturation region and $V_{GS} = 0.8$ for 250 K and 500 K are approximately equal. Figure 4(a) shows on-state current versus temperature at $V_{GS} = 0.8$ V and $V_{DS} = 0.8$ V. The on-state current increases when temperature increases. The slope of this increase is approximately constant. Also, the temperature variation of off-current is illustrated in Figure 4(b) at $V_{GS} = 0$ V and $V_{DS} = 0.8$ V bias conditions. It is observed from the figure that the off-current in $T = 500$ K is 150 times higher than $T = 250$ K. Therefore, in spite of the on-current increase, the device reliability declines due to large rise in leakage current.

Figure 5(a) shows the transconductance characteristics of the CNTFET with the gate length of 20 nm for two different temperatures at $V_{DS} = 50$ mV and $V_{DS} = 0.8$ V. Although the on-state current increases when the temperature is increased from 250 to 500 K, the off-state leakage current grows considerably faster than that of the on-state current which confirms the previous results. Drain conductance (g_d) depends on the drain current in on-state. So, increase in on-current results in increase in drain conductance. The dependence of drain conductance on temperature at $V_{GS} = 0.8$ V and $V_{DS} = 0.8$ V is shown in Figure 5(b). It is evident

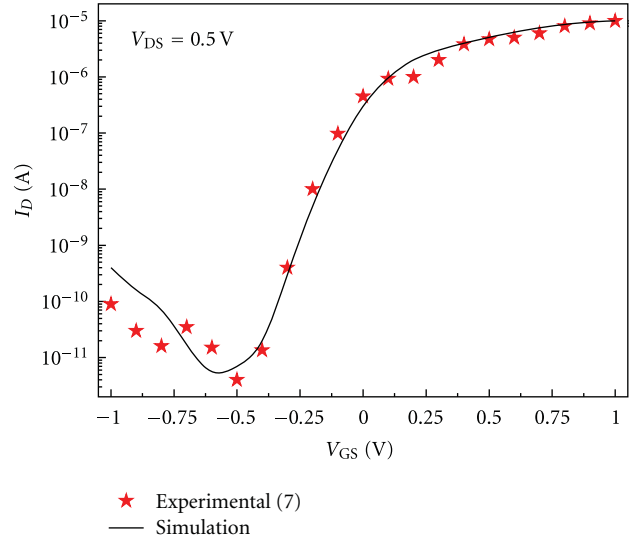


FIGURE 2: Comparison of the simulated I_D - V_{GS} characteristic with that measured experimentally in [7] at $V_{DS} = 0.5$ V.

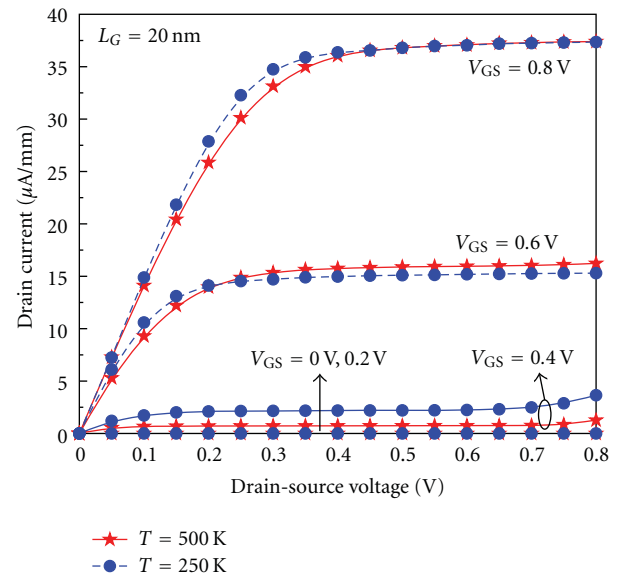
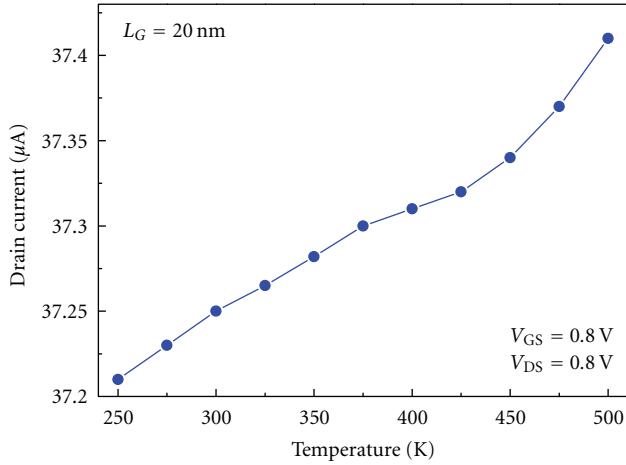


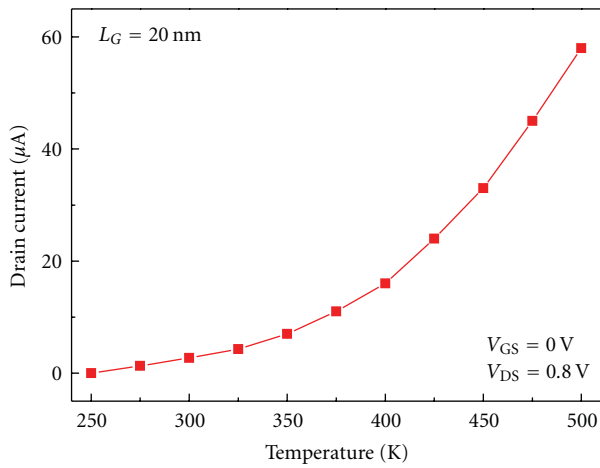
FIGURE 3: Comparison of the output characteristics (I_D - V_{DS}) of the CNTFET in 250 and 500 K for different gate biases.

from the figure that the drain conductance raises as the temperature increases by a factor of 2 from 250 to 500 K.

Figure 6(a) illustrates the off-state leakage current versus saturation current (I_{off} - I_{on}) of CNTFET when temperature is varied from 250 to 500 K. The saturation current (I_{on}) is the drain current at $V_{GS} = 0.8$ V and $V_{DS} = 0.8$ V and the leakage current (I_{off}) is the drain current at $V_{GS} = 0$ V and $V_{DS} = 0.8$ V. It can be seen that the current capability of CNTFET degrades as the temperature is increased. Figure 6(b) shows the simulated on-/off-current ratio (I_{on}/I_{off}) of CNTFET for different temperatures. The on-/off-current ratio of CNTFET is significantly reduced in higher temperatures. By increasing



(a)

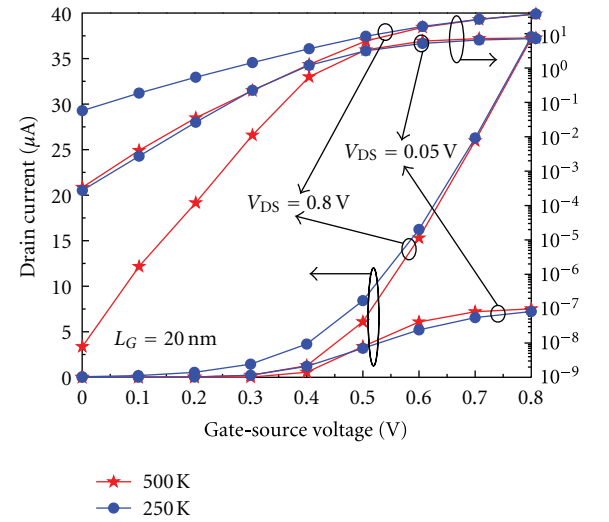


(b)

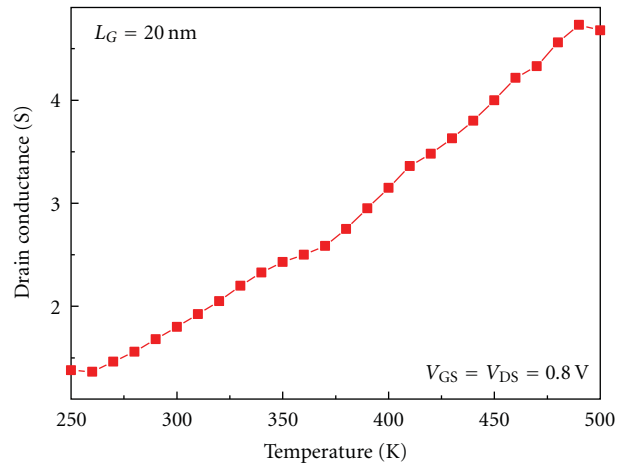
FIGURE 4: (a) On-state current versus temperature at $V_{GS} = 0.8$ V and $V_{DS} = 0.8$ V. (b) off-state current versus temperature at $V_{GS} = 0$ V and $V_{DS} = 0.8$ V.

the temperature the on-/off-current ratio decreases. It is apparent from the figure that the I_{on}/I_{off} ratio of 1.1×10^5 at 250 K reduces to 650.4 at 500 K which shows the undesirable effects of increasing temperature in the current drive of the device. This ratio for $T = 500$ K is 169 times lower than $T = 250$ K. This decrease is apparent and more noticeable between 250 and 310 K. After 310 K the reduction slope decreases and after 410 K the on-/off-current ratio is approximately constant. The results imply that increasing the temperature declines the gate control on channel, and therefore the current capability. It can be concluded from Figures 6(a) and 6(b) that the increment in temperature not only increases the on-state current but also leads to a higher off-state leakage current.

The threshold voltage (V_{th}) is one of the most important parameters of the nanoscale devices. The variations in leakage and on-state currents by temperature indicate that the device threshold voltage changes by temperature. Therefore, it is necessary to investigate the influence of



(a)



(b)

FIGURE 5: Variation of (a) transconductance (g_m) and (b) drain conductance (g_d) at $V_{DS} = 0.8$ V and $V_{GS} = 0.8$ V as a function of temperature.

temperature variation on the threshold voltage characteristic of CNTFETs. Figure 7 shows the threshold voltage variation of the CNTFET structure as a function of the temperature. It can be seen that by varying the temperature, the device shows an approximately large V_{th} variation which is undesirable for reliable CMOS applications.

It can be clearly observed that the slope of V_{th} variation increases when the temperature increases from 250 to 500 K. The CNTFET structure exhibits lower threshold voltage roll-off at lower temperatures. This is more noticeable that for temperatures higher than 310 K the reduction slope increases with an approximately flat slope. This indicates that the roll-off of the threshold voltage is more severe for higher temperatures due to the short channel effects.

The subthreshold swing is a key parameter for transistor miniaturization. A small subthreshold swing is required to provide an adequate value of the on-/off-current ratio.

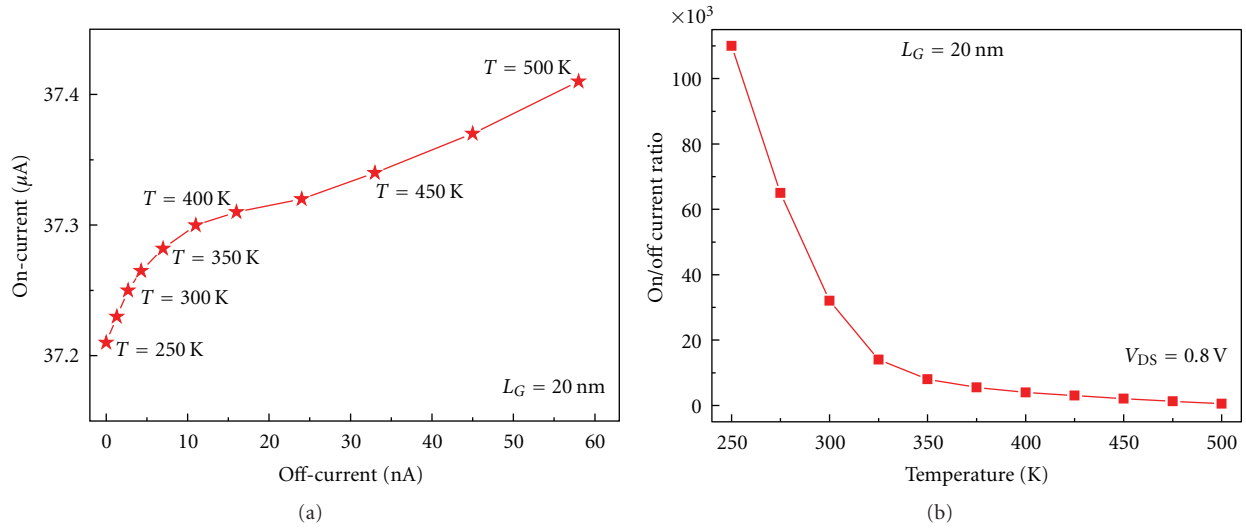


FIGURE 6: Temperature dependency of the (a) $I_{\text{off}}-I_{\text{on}}$ and (b) $I_{\text{on}}/I_{\text{off}}$ characteristics at $V_{DS} = 0.8\text{ V}$.

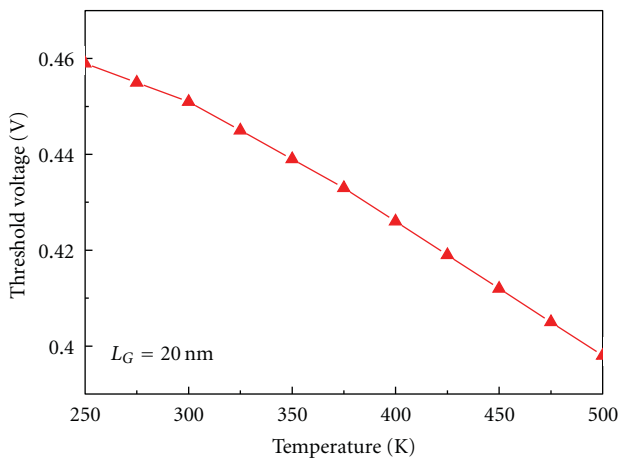


FIGURE 7: Threshold voltage variation characteristics as a function of temperature.

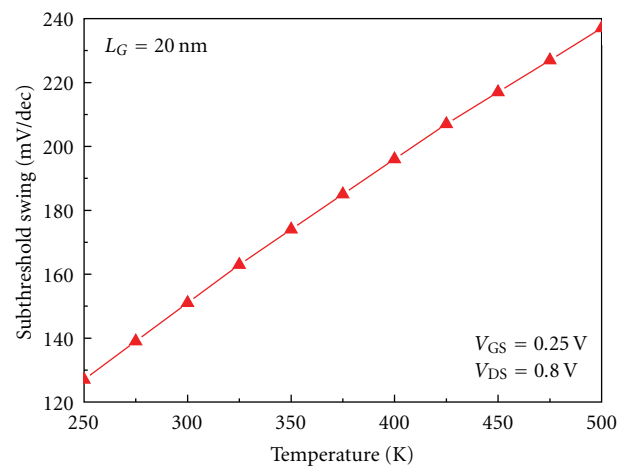


FIGURE 8: Subthreshold swing as a function of temperature.

Also, it is desired for low threshold voltage and low power operation FETs that scaled down to small sizes. The variation in subthreshold swing versus temperature for the CNTFET with 20 nm gate length is shown in Figure 8. It can be seen that the subthreshold swing increases with the increase in temperature. Approximately, the subthreshold swing increases by 4.35 mV in each temperature decade at $V_{GS} = 0.25\text{ V}$ and $V_{DS} = 0.8\text{ V}$ bias conditions.

As the channel length enters into the nanometer regime, many undesirable quantum and short-channel effects (SCEs) such as the threshold voltage roll-off and the DIBL become more apparent. These harmful effects cause deviation from the ideal performance of the CNTFETs. The DIBL effect is an electrostatic effect that can change the channel from a state of pinch-off to conduction and result in a substantial leakage current. It also shifts the threshold voltage and renders the gate ineffective in controlling the channel. Consequently, the

DIBL effect degrades the device performance which should be avoided in device and circuit design. As can be seen from Figure 9 by increasing temperature the undesirable DIBL effect significantly increases. It should be noted that the DIBL effect occurs when the barrier height for channel carriers at the edge of the source reduces due to the influence of drain electric field, upon application of a high drain voltage. Similar mechanism can take place when the temperature increases. Therefore the energy of carriers increases and a large number of carriers injected into the channel, leading to an increased drain off-current. The relationship between the subthreshold swing and DIBL parameters of CNTFET from 250 K to 500 K is presented in Figure 10. It is interesting to notice that the subthreshold swing and DIBL parameters are almost linearly correlated, confirming that the degradation of these parameters has the same origin and can be perfectly influenced by the temperature.

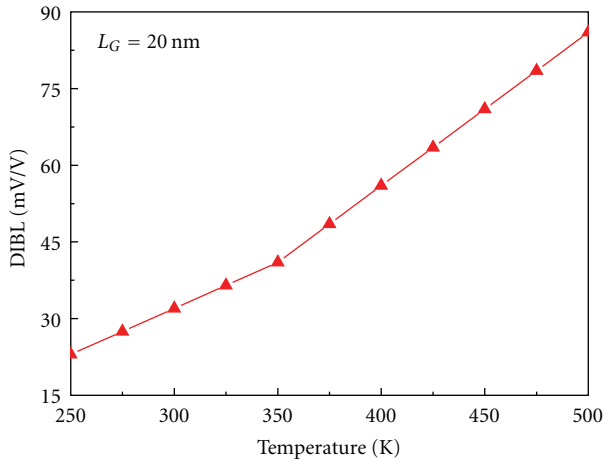


FIGURE 9: Drain-induced barrier lowering (DIBL) as a function of temperature.

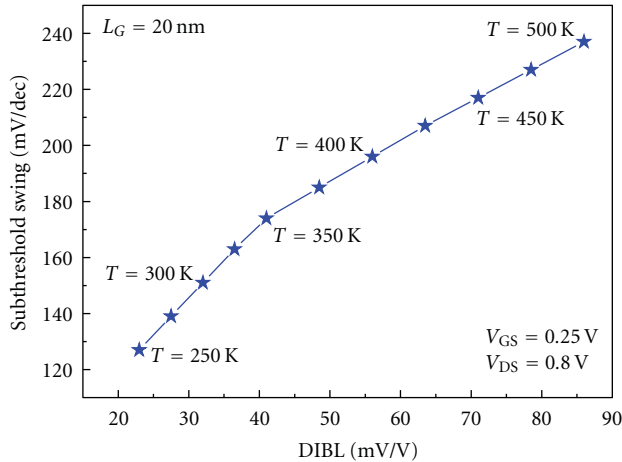


FIGURE 10: Relationship between the subthreshold swing and the DIBL parameters in different temperatures.

4. Conclusions

In this paper the attributes of carbon nanotube field-effect transistors (CNTFETs) by varying the temperature have been comprehensively investigated by developing a two-dimensional (2D) quantum simulation. By employing the nonequilibrium Green's function (NEGF) formalism and solving the Schrödinger and Poisson equations self-consistently, the influence of varying temperature on CNTFET performance in terms of on-current, off-current, on-/off-current ratio, transconductance, drain conductance characteristics, drain-induced barrier lowering (DIBL), threshold voltage, and subthreshold swing have been explained. The results show that the increase in temperature results in higher subthreshold swing and lower on-/off-current ratio. It is interesting to notice that the subthreshold swing and DIBL parameters are almost linearly correlated, confirming that the degradation of these parameters has the same origin and can be perfectly influenced by the temperature. These

achievements can be effectively used for design considerations in these devices.

References

- [1] P. Avouris and J. Chen, "Nanotube electronics and optoelectronics," *Materials Today*, vol. 9, no. 10, pp. 46–54, 2006.
- [2] P. L. McEuen, M. S. Fuhrer, and H. Park, "Single-walled carbon nanotube electronics," *IEEE Transactions on Nanotechnology*, vol. 1, no. 1, pp. 78–85, 2002.
- [3] S. Iijima, "Helical microtubules of graphitic carbon," *Nature*, vol. 354, no. 6348, pp. 56–58, 1991.
- [4] Q. Lu, D. Park, A. Kalnitsky et al., "Leakage current comparison between ultra-thin Ta₂O₅ films and conventional gate dielectrics," *IEEE Electron Device Letters*, vol. 19, no. 9, pp. 341–342, 1998.
- [5] R. Martel, T. Schmidt, H. R. Shea, T. Hertel, and P. Avouris, "Single- and multi-wall carbon nanotube field-effect transistors," *Applied Physics Letters*, vol. 73, no. 17, pp. 2447–2449, 1998.
- [6] S. J. Tans, A. R. M. Verschueren, and C. Dekker, "Room-temperature transistor based on a single carbon nanotube," *Nature*, vol. 393, no. 6680, pp. 49–52, 1998.
- [7] Y. M. Lin, J. Appenzeller, J. Knoch, and P. Avouris, "High-performance carbon nanotube field-effect transistor with tunable polarities," *IEEE Transactions on Nanotechnology*, vol. 4, no. 5, pp. 481–489, 2005.
- [8] Z. Arefinia and A. A. Orouji, "Novel attributes in scaling issues of carbon nanotube field-effect transistors," *Microelectronics Journal*, vol. 40, no. 1, pp. 5–9, 2009.
- [9] F. Assad, Z. Ren, D. Vasileska, S. Datta, and M. Lundstrom, "On the performance limits for Si MOSFET's: a theoretical study," *IEEE Transactions on Electron Devices*, vol. 47, no. 1, pp. 232–240, 2000.
- [10] K. Natori, "Ballistic metal-oxide-semiconductor field effect transistor," *Journal of Applied Physics*, vol. 76, no. 8, pp. 4879–4890, 1994.
- [11] J. Knoch, B. Lengeler, and J. Appenzeller, "Quantum simulations of an ultrashort channel single-gated n-MOSFET on SOI," *IEEE Transactions on Electron Devices*, vol. 49, no. 7, pp. 1212–1218, 2002.
- [12] Y. Naveh and K. K. Likharev, "Modeling of 10-nm-scale ballistic MOSFET's," *IEEE Electron Device Letters*, vol. 21, no. 5, pp. 242–244, 2000.
- [13] M. Bescond, N. Cavassilas, and M. Lannoo, "Effective-mass approach for n-type semiconductor nanowire MOSFETs arbitrarily oriented," *Nanotechnology*, vol. 18, no. 25, Article ID 255201, 2007.
- [14] R. S. Muller and T. I. Kamins, *Device Electronics for Integrated Circuits*, Wiley, New York, NY, USA, 1986.
- [15] G. Fiori, G. Iannaccone, and G. Klimeck, "Performance of carbon nanotube field effect transistors with doped source and drain extensions and arbitrary geometry," in *Proceedings of the IEEE International Electron Devices Meeting (IEDM '05)*, pp. 522–525, Washington, DC, USA, December 2005.
- [16] J. Guo, S. O. Koswatta, N. Neophytou, and M. Lundstrom, "Carbon nanotube field-effect transistors," *International Journal of High Speed Electronics and Systems*, vol. 16, no. 4, pp. 897–912, 2006.
- [17] A. Javey, R. Tu, D. B. Farmer, J. Guo, R. G. Gordon, and H. Dai, "High performance n-type carbon nanotube field-effect transistors with chemically doped contacts," *Nano Letters*, vol. 5, no. 2, pp. 345–348, 2005.

- [18] E. Amat, T. Kauerauf, R. Degraeve et al., "Competing degradation mechanisms in short-channel transistors under channel hot-carrier stress at elevated temperatures," *IEEE Transactions on Device and Materials Reliability*, vol. 9, no. 3, Article ID 5075549, pp. 454–458, 2009.
- [19] Y. Naveh, V. Sverdlov, and K. Likharev, "Nanoscale MOSFETs scaling," in *Proceedings of the 59th Annual Device Research Conference (DRC '01)*, pp. 61–62, Notre Dame, Ind, USA, June 2001.
- [20] H. Kawaura, T. Sakamoto, T. Baba et al., "Transistor operation of 30-nm gate-length EJ-MOSFETs," *IEEE Electron Device Letters*, vol. 19, no. 3, pp. 74–76, 1998.
- [21] B. Szelag, F. Balestra, and G. Ghibaudo, "Comprehensive analysis of reverse short-channel effect in silicon MOSFET's from low-temperature operation," *IEEE Electron Device Letters*, vol. 19, no. 12, pp. 511–513, 1998.
- [22] J. Xu and M. C. Cheng, "Design optimization of high-performance low-temperature 0.18 μm MOSFET's with low-impurity-density channels at supply voltage below 1 V," *IEEE Transactions on Electron Devices*, vol. 47, no. 4, pp. 813–821, 2000.
- [23] H. J. Huang, K. M. Chen, T. Y. Huang et al., "Improved low temperature characteristics of p-channel MOSFETs with $\text{Si}_{1-x}\text{Ge}_x$ s raised source and drain," *IEEE Transactions on Electron Devices*, vol. 48, no. 8, pp. 1627–1632, 2001.
- [24] J. Guo, J. Wang, E. Polizzi, S. Datta, and M. Lundstrom, "Electrostatics of nanowire transistors," *IEEE Transactions on Nanotechnology*, vol. 2, no. 4, pp. 329–334, 2003.
- [25] A. Svizhenko, M. P. Anantram, T. R. Govindan, B. Biegel, and R. Venugopal, "Two-dimensional quantum mechanical modeling of nanotransistors," *Journal of Applied Physics*, vol. 91, no. 4, pp. 2343–3255, 2002.
- [26] J. P. Clifford, D. L. John, L. C. Castro, and D. L. Pulfrey, "Electrostatics of partially gated carbon nanotube FETs," *IEEE Transactions on Nanotechnology*, vol. 3, no. 2, pp. 281–286, 2004.
- [27] R. Saito, G. Dresselhaus, and M. S. Dresselhaus, *Physical Property of Carbon Nanotubes*, Imperial College Press, London, UK, 1998.
- [28] J. Guo, S. Datta, M. Lundstrom, and M. P. Anantram, "Toward multi-scale modeling of carbon nanotube transistors," *International Journal for Multiscale Computational Engineering*, vol. 2, no. 2, pp. 76–96, 2004.

Research Article

Synthesis of SnO₂-ZnO Core-Shell Nanowires and Their Optoelectronic Properties

Ko-Ying Pan,¹ Yu-Hung Lin,¹ Po-Sheng Lee,¹ Jyh-Ming Wu,² and Han C. Shih^{1,3}

¹Department of Materials Science and Engineering, National Tsing Hua University, Hsinchu 300, Taiwan

²Department of Materials Science and Engineering, Feng Chia University, Taichung 407, Taiwan

³Institute of Materials Science and Nanotechnology, Chinese Culture University, Taipei 111, Taiwan

Correspondence should be addressed to Han C. Shih, hcshih@mx.nthu.edu.tw

Received 25 August 2011; Revised 2 November 2011; Accepted 2 November 2011

Academic Editor: Istvan Robel

Copyright © 2012 Ko-Ying Pan et al. This is an open access article distributed under the Creative Commons Attribution License, which permits unrestricted use, distribution, and reproduction in any medium, provided the original work is properly cited.

Zinc oxides deposited on Tin dioxide nanowires have been successfully synthesized by atomic layer deposition (ALD). The diameter of SnO₂-ZnO core-shell nanowires is 100 nm by ALD 200 cycles. The result of electricity measurements shows that the resistance of SnO₂-ZnO core-shell nanowires (ALD: 200 cycles) is 925 Ω, which is much lower than pure SnO₂ nanowires (3.6 × 10⁶ Ω). The result of UV light test shows that the recovery time of SnO₂-ZnO core-shell nanowires (ALD: 200 cycles) is 328 seconds, which is lower than pure SnO₂ nanowires (938 seconds). These results demonstrated that the SnO₂-ZnO core-shell nanowires have potential application as UV photodetectors with high photon-sensing properties.

1. Introduction

Tin dioxide (SnO₂) and zinc oxide (ZnO), world-renowned n-type multifunctional semiconductors, have wide direct band-gap energy: 3.6 and 3.37 eV at 300 K, respectively. Furthermore, because of the very large length-to-diameter and surface-to-volume ratios in nanoscale regime, the gas sensing and optoelectronic properties of one-dimensional SnO₂ and ZnO nanostructures are highly sensitive to adsorbed species on their own surface. Owing to special physical and chemical characteristics of one-dimensional SnO₂ and ZnO nanowires, plenty of nanocompounds based on them have been widely applied to many industrial places, such as field emission devices [1], lithium-ion batteries [2], optoelectronic devices [3–6], and gas sensors [6–10]. However, upgrading the optoelectronic sensitivity is still a challenge for SnO₂ nanostructure-based photodetectors.

In recent years, many literatures have demonstrated that nanocompounds of SnO₂ and ZnO which belong to a hetero-combination acted with good chemical and physical properties exceeding to their individual materials [11–13]. Most of all, a synthesis of core-shell nanostructure is a considered method for strongly improving sensing properties of SnO₂

nanowires since surface states affects the sensing properties significantly.

In this study, SnO₂-ZnO core-shell nanowires were synthesized by a step-by-step manufacture. First, SnO₂ nanowires were fabricated by thermal evaporation. Second, ZnO layers were deposited on SnO₂ nanowires by atomic layer deposition. Atomic layer deposition (ALD), a chemical vapor deposition, is a cutting-edge technique for the good controllable deposition of inorganic layers and has been commonly applied to semiconductor industries. In particular, the self-limiting gas-solid growth features of the ALD growth expedites the growth of thin films and nanomaterials with pretty accurate thickness and good uniformity. A few research of SnO₂-ZnO core-shell nanowires focuses on enhancement of optoelectronic sensing, so their optoelectronic properties under UV light were investigated.

2. Experimental

There are two steps in this fabrication of SnO₂-ZnO core-shell nanowires. In advance, an Au layer (about 30 Å), a catalyst in this fabrication, was coated on aluminum substrates by sputtering. In the first step, Tin oxide nanowires were

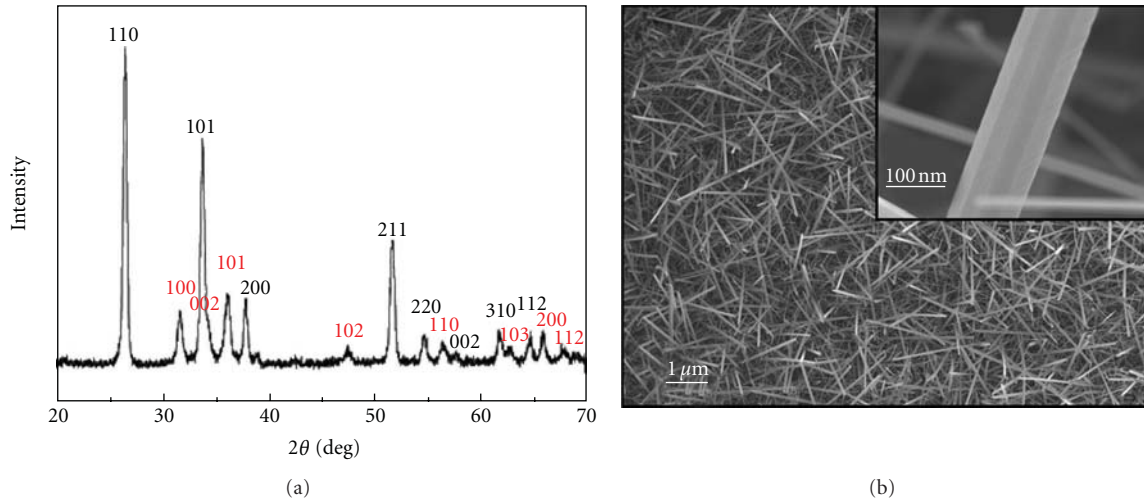


FIGURE 1: (a) XRD pattern (b) SEM image of SnO_2 -ZnO core-shell nanowires (ALD: 200 cycles).

fabricated on aluminum substrates by thermal evaporation. High quality 0.4 g Sn powders (Aldrich, purity 99.99%) and several aluminum substrates were situated in an Al boat and then placed the Al boat in the heating area of a quartz tube. In the growth of Sn nanowires, the pressure inside the quartz tube was kept up at 1 Torr by a rotary pump. The working conditions of this process were as follows. (1) Raising the temperature to 950°C with $20^\circ\text{C}/\text{min}$ was at a constant flow rate of 10 sccm Ar gas. (2) Maintaining the temperature at 950°C for 1 hour was at a constant flow rate of mixed gas of 10 sccm Ar and 1 sccm O_2 . (3) Cooling to the room temperature was under a constant flow rate of 10 sccm of Ar gas.

In the second step, a ZnO layer was coated on SnO_2 nanowires by atomic layer deposition (ALD) [14–16]. The precursors were DEZ ($\text{Zn}(\text{C}_2\text{H}_5)_2$, Aldrich, purity 98%) and H_2O (purity 99.999%) in 200 ALD reaction cycles. Every single cycle, a 60 ms DEZ pulse and a 60 ms H_2O pulse were sequentially delivered into the ALD chamber by 5 s of purging with N_2 (purity 99.9995%). The pressure of chamber was maintained 1 Torr in the ALD reaction.

The morphology, crystal structure, and chemical composition of the SnO_2 -ZnO core-shell nanowires were analyzed by a field emission-scanning electron microscope (FESEM, JEOL JSM-6900F), a MAC glancing incident X-ray spectrometer with an incident angle of 0.5° , a high-resolution transmission electron microscope (HRTEM, JEOL, JEM-2010), and X-ray photoelectron spectroscopy (XPS Perkin-Elmer Model PHI1600 system). In order to test the optoelectronic properties of SnO_2 -ZnO core-shell nanowires, the measurements of I-V curves via a constant voltage (5 V) and photoresponse curves under UV light ($\lambda = 365 \text{ nm}$ and intensity is $17.1 \text{ W}/\text{m}^2$) were handled.

3. Results and Discussion

Figure 1(a) shows the XRD $\theta - 2\theta$ diffraction pattern of the SnO_2 -ZnO core-shell nanowires obtained after 200 ALD

reaction cycles. Red numbers (100), (002), and (101) are the main planes in ZnO with hexagonal wurtzite structure, and this XRD pattern corresponds with JCPDS: 89-1397. The lattice constants of hexagonal wurtzite structure are as follows: $a = b = 3.253 \text{ \AA}$ and $c = 5.213 \text{ \AA}$. Black numbers are the main planes in SnO_2 with tetragonal rutile structure with lattice constants: $a = b = 4.737 \text{ \AA}$, $c = 3.187 \text{ \AA}$, and this XRD pattern matches up with JCPDS: 88-0287. Figure 1(b) is the SEM image of the SnO_2 -ZnO core-shell nanowires obtained after 200 ALD reaction cycles, and the enlarged image is in the upper right corner. According to these images, the abundant SnO_2 -ZnO core-shell nanowires with dimensions of 100–150 nm in diameters and several micrometers in length have been produced. These results demonstrate that the nanocompound is made of SnO_2 and ZnO without other materials, signifying that the high quality nanocompounds of SnO_2 -ZnO have been successfully prepared.

To further investigate the detailed microstructure of SnO_2 -ZnO core-shell nanowires, taking images by TEM was performed. Figures 2(a) and 2(b) show a low-magnification TEM image. The diameter of core-shell nanowires is 100 nm, and the thickness of ZnO shell layer is 25 nm. From Figure 2(c), the HRTEM image of core-shell SnO_2 -ZnO nanowires shows that the lattice spacing between (0002) is 0.28 nm, and the structure of ZnO that has hexagonal structure is corresponding. From Figure 2(d), the growth direction is [101], the lattice space is 0.26 nm, and the angle between [101] and $[-101]$ is 67.85° , which are consistent with the SnO_2 that has tetragonal rutile structure. According to these TEM images, no doubt the core-shell nanostructure is certainly formed via two-step method.

In order to identify the chemical composition of the SnO_2 -ZnO core-shell nanowires and check the quality of ZnO deposited on SnO_2 by ALD, the core-shell SnO_2 -ZnO nanowires were additionally characterized by XPS. Figure 3(a) shows that the binding energy of Zn ($2p_{3/2}$) and Zn ($2p_{1/2}$) are 1021.9 eV and 1044.9 eV, respectively. Figure 3(b) shows that the binding energy of O (1s) is

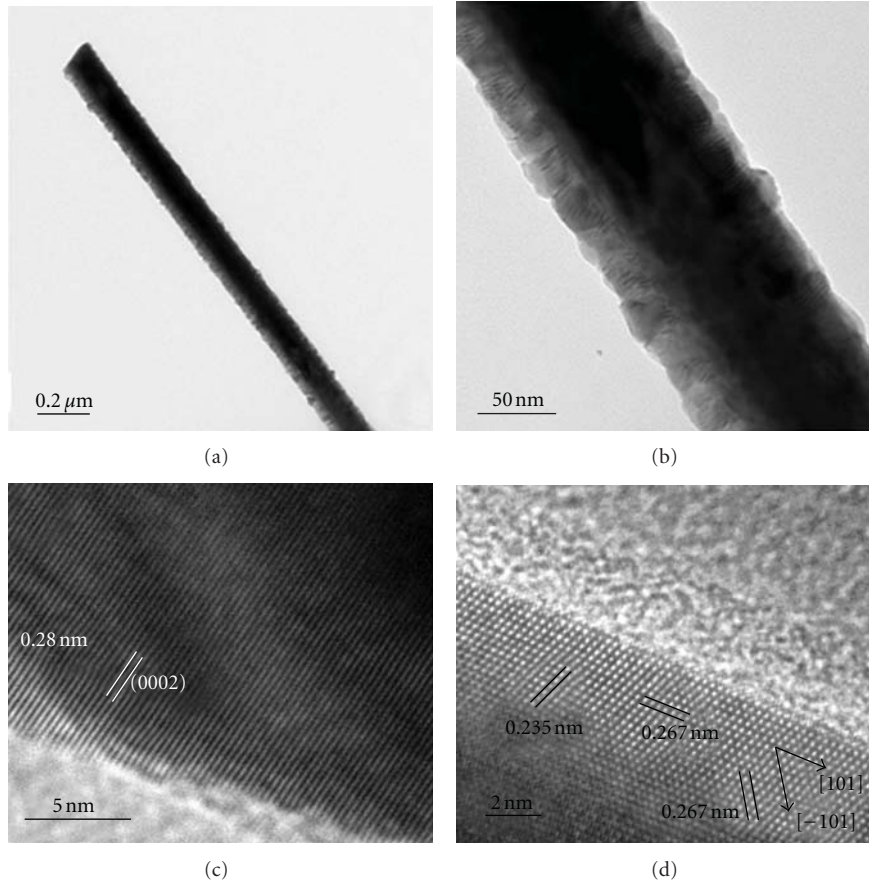


FIGURE 2: (a) and (b) Low-magnification TEM, (c) HRTEM image of a SnO₂-ZnO core-shell nanowires (ALD: 200 cycles), and (d) HRTEM image of a SnO₂ single nanowires.

530.9 eV. Figure 3(c) shows that binding energy of Sn ($3d_{3/2}$) and Sn ($3d_{5/2}$) is 495.1 eV and 487.5 eV. After integration of the area of three main elements “peaks by computer program”, the atomic percentages of oxygen, zinc, and tin are 55.27, 41.7, and 3.03, respectively. Judging from XPS analysis, because the atomic percentage of ZnO is large in this compound, ZnO crystalline shell is definitely deposited on SnO₂ nanowires by ALD.

By above material analyses, the confirmation of SnO₂-ZnO core-shell nanowires synthesized sequentially via thermal evaporation, and ALD was done. To determine the potential applicability of SnO₂-ZnO core-shell nanowires in this study to photodetectors, their I-V curves and UV photon-sensing properties were investigated. Figure 4 shows the current-voltage (I-V) curves of SnO₂-ZnO core-shell nanowires with ALD 200 cycles reaction (red line) and pure SnO₂ nanowires (black line) at room temperature and atmospheric pressure. Two curves show a good ohmic contact between the nanocompounds and Ag electrodes. The electrical resistivity can be expressed as $R = \rho \times L/A$, and the electrical resistivity of SnO₂-ZnO nanowires and pure SnO₂ nanowires can be solved as 925 Ω and $3.6 \times 10^6 \Omega$, respectively. The electrical resistivity of core-shell nanostructure is much lower than pure nanowires. Because of that ZnO film of core-shell SnO₂-ZnO nanowires is more

compact than SnO₂ nanowires, this effect is able to increase the film conductivity.

When setting up an electric circuit with core-shell nanostructures, there will be a strain in a heterointerface to keep from a deformation happened and decrease the total energy. Moreover, the band gap of core-shell materials will be reduced, and then the conductivity will be raised [17].

To investigate the application of SnO₂-ZnO core-shell nanostructure and pure SnO₂ nanowires for UV detectors, the optoelectronic response and recovery of the as-fabricated photodetectors were tested under emitted UV lamps ($\lambda = 365 \text{ nm}$). The optoelectronic test unveils that the current very quickly rises to a steady level under UV light (UV light is on) and then increasingly recovers to the initial state in the dark (UV light is off). Figures 5(a) and 5(b) show the period photoresponse curve of pure SnO₂ nanowires and SnO₂-ZnO core-shell nanowires (200 ALD cycles), respectively. In previous studies [18], the opinion of these photoresponse curves was discussed. When the UV light is off, the species of oxygen molecular structure are chemisorbed on the interfaces of nanostructures because oxygen molecules catch free electrons, that is, $\text{O}_{2(g)} + e^- \rightarrow \text{O}_{2(ad)}^-$. Therefore, a low conductivity depletion layer is formed near the surface of nanowires, and the nonmaterial's conductivity will be decreased. When UV light is on, electron-hole

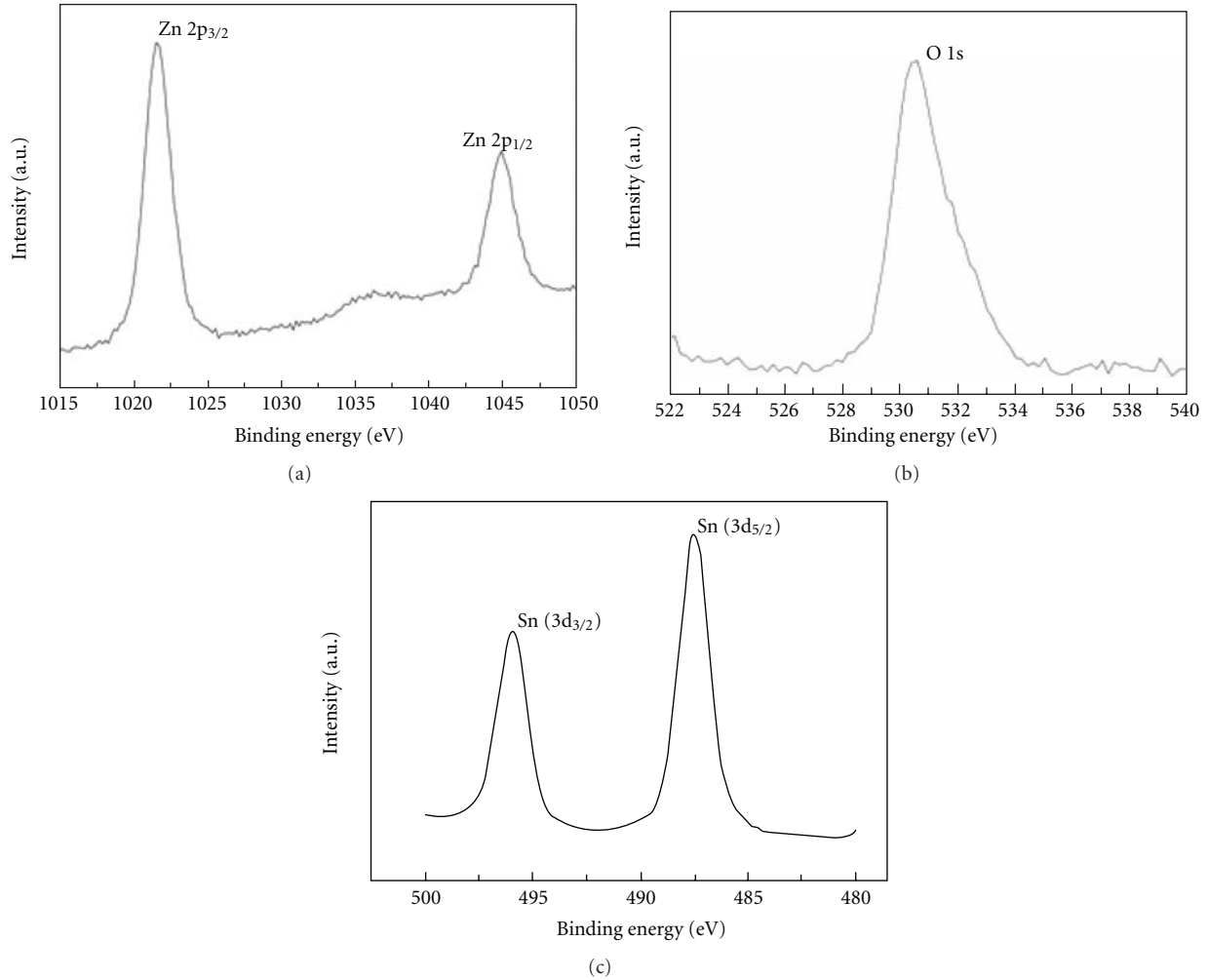


FIGURE 3: The XPS (a) Zn 2p (b) O 1S (c) Sn 3d spectrum.

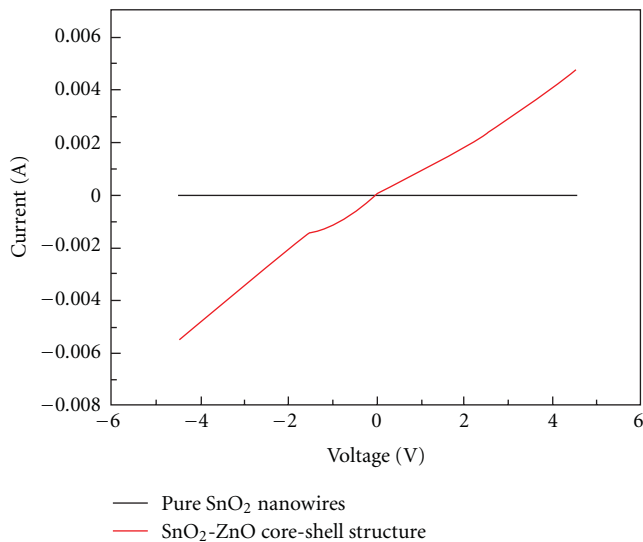


FIGURE 4: The I-V curve of SnO₂-ZnO core-shell nanowires (ALD: 200 cycles) and pure SnO₂ nanowires.

pairs follow this reaction, $h\nu \rightarrow e^- + h^+$, and will be happened in the nanowires. The photoinduced holes will relocate to the surface and recombine with the oxygen ions, that is, $h^+ + O_{2(ad)}^- \rightarrow O_{2(g)}$. At the same time, the photon-generated electronics are able to play free electrons and upgrade the electron conductance of nanowires. The photocurrent rapidly increases with the reduced depletion layer.

Figure 5(a) shows that since UV light is on, the current is 3.47×10^{-6} A. After 50 seconds, the current increases to 7.23×10^{-6} A. The slope is 0.0752. From Figure 5(b), since UV light is on, the current is 3.53×10^{-5} A. After 50 seconds, the current lifts to 5.35×10^{-5} A. The slope is 0.0364. Therefore, the device based on pure SnO₂ nanowires has a better sensitivity than based on SnO₂-ZnO core-shell nanowires. In terms of photosensitivity, the pure SnO₂ nanowires are little larger than the SnO₂-ZnO core-shell nanowires, and two depletion areas of core-shell nanostructure might be the cause for this phenomenon. However, the recovery time of core-shell SnO₂-ZnO nanowires is just 328 seconds, which is much shorter than that of pure SnO₂ nanowires

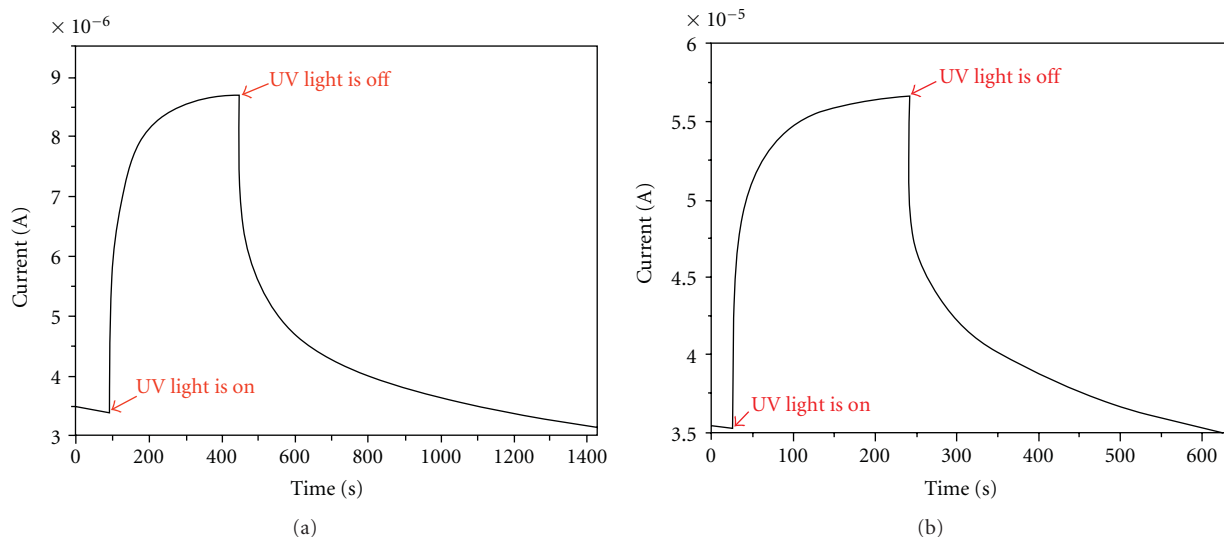


FIGURE 5: Photoresponse curves of (a) pure SnO₂ nanowires and (b) SnO₂-ZnO core-shell nanowires-based photodetectors.

(938 seconds). It is a reason that a superposition of the homo- and heterointerfaces formed at the junctions may be the root cause for the decreased recovery time compared with the detector judging from the nanowires without the shell layer [19, 20]. All in all, the SnO₂-ZnO core-shell nanowires have positive characteristics and applications in the manufacture of photodetectors.

4. Conclusion

SnO₂-ZnO core-shell nanowires have been successfully fabricated by a step-by-step process. First, SnO₂ nanowires were synthesized by thermal evaporation. Sequentially, ZnO shell layers were deposited by ALD. The SnO₂-ZnO core-shell nanowire-based photodetectors has the low electrical resistance (925 Ω) and the short recovery time (328 seconds), compared with pure SnO₂ nanowires. Thanks to excellent optoelectron abilities, the SnO₂-ZnO core-shell nanowires are the promising candidates as photodetectors.

References

- [1] Q. Wan, E. N. Dattoli, and W. Lu, "Transparent metallic Sb-doped SnO₂ nanowires," *Applied Physics Letters*, vol. 90, no. 22, Article ID 222107, 2007.
- [2] S. L. Chou, J. Z. Wang, C. Zhong, M. M. Rahman, H. K. Liu, and S. X. Dou, "A facile route to carbon-coated SnO₂ nanoparticles combined with a new binder for enhanced cyclability of Li-ion rechargeable batteries," *Electrochimica Acta*, vol. 54, no. 28, pp. 7519–7524, 2009.
- [3] P. S. Lee, Y. H. Lin, Y. S. Chang, J. M. Wu, and H. C. Shih, "Growth and characterization of thermally evaporated ATO nanowires," *Thin Solid Films*, vol. 519, no. 5, pp. 1749–1754, 2010.
- [4] Y. H. Lin, Y. C. Hsueh, C. C. Wang, J. M. Wu, T. P. Perng, and H. C. Shih, "Enhancing the photon-sensing properties of ZnO nanowires by atomic layer deposition of platinum," *Electrochemical and Solid-State Letters*, vol. 13, no. 12, pp. K93–K95, 2010.
- [5] Q. Kuang, Z. Y. Jiang, Z. X. Xie et al., "Tailoring the optical property by a three-dimensional epitaxial heterostructure: a case of ZnO/SnO₂," *Journal of the American Chemical Society*, vol. 127, no. 33, pp. 11777–11784, 2005.
- [6] Y. H. Lin, Y. C. Hsueh, P. S. Lee et al., "Preparation of Pt/SnO₂ core-shell nanowires with enhanced ethanol gas- and photon-sensing properties," *Journal of the Electrochemical Society*, vol. 157, no. 9, pp. K206–K210, 2010.
- [7] A. Kolmakov, Y. Zhang, G. Cheng, and M. Moskovits, "Detection of CO and O₂ using tin oxide nanowire sensors," *Advanced Materials*, vol. 15, no. 12, pp. 997–1000, 2003.
- [8] V. Kumar, S. Sen, K. P. Muthe, N. K. Gaur, S. K. Gupta, and J. V. Yakhmi, "Copper doped SnO₂ nanowires as highly sensitive H₂S gas sensor," *Sensors and Actuators B*, vol. 138, no. 2, pp. 587–590, 2009.
- [9] D. Wang, X. Chu, and M. Gong, "Gas-sensing properties of sensors based on single-crystalline SnO₂ nanorods prepared by a simple molten-salt method," *Sensors and Actuators B*, vol. 117, no. 1, pp. 183–187, 2006.
- [10] X. Wang, J. Zhang, and Z. Zhu, "Ammonia sensing characteristics of ZnO nanowires studied by quartz crystal microbalance," *Applied Surface Science*, vol. 252, no. 6, pp. 2404–2411, 2006.
- [11] I. S. Hwang, S. J. Kim, J. K. Choi et al., "Synthesis and gas sensing characteristics of highly crystalline ZnO-SnO₂ core-shell nanowires," *Sensors and Actuators B*, vol. 148, no. 2, pp. 595–600, 2010.
- [12] M. Shahid, I. Shakir, S. J. Yang, and D. J. Kang, "Facile synthesis of core-shell SnO₂/V₂O₅ nanowires and their efficient photocatalytic property," *Materials Chemistry and Physics*, vol. 124, no. 1, pp. 619–622, 2010.
- [13] Y. T. Yu and P. Dutta, "Examination of Au/SnO₂ core-shell architecture nanoparticle for low temperature gas sensing applications," *Sensors and Actuators B*, vol. 157, no. 2, pp. 444–449, 2011.
- [14] R. L. Puurunen, "Surface chemistry of atomic layer deposition: a case study for the trimethylaluminum/water process," *Journal of Applied Physics*, vol. 97, no. 12, Article ID 121301, pp. 1–52, 2005.

- [15] L. Niinistö, M. Ritala, and M. Leskelä, "Synthesis of oxide thin films and overlayers by atomic layer epitaxy for advanced applications," *Materials Science and Engineering B*, vol. 41, no. 1, pp. 23–29, 1996.
- [16] M. Leskelä and M. Ritala, "Atomic layer deposition (ALD): from precursors to thin film structures," *Thin Solid Films*, vol. 409, no. 1, pp. 138–146, 2002.
- [17] J. Schrier, D. O. Demchenko, L. W. Wang, and A. P. Alivisatos, "Optical properties of ZnO/ZnS and ZnO/ZnTe heterostructures for photovoltaic applications," *Nano Letters*, vol. 7, no. 8, pp. 2377–2382, 2007.
- [18] Y. H. Lin, C. C. Kuo, J. M. Wu, U. S. Chen, Y. S. Chang, and H. C. Shih, "Characterization and cathodoluminescence of beak-like SnO₂ nanorods," *Japanese Journal of Applied Physics*, vol. 47, no. 10, pp. 8141–8144, 2008.
- [19] S. W. Choi, J. Y. Park, and S. S. Kim, "Synthesis of SnO₂-ZnO core-shell nanofibers via a novel two-step process and their gas sensing properties," *Nanotechnology*, vol. 20, no. 46, Article ID 465603, 2009.
- [20] J. M. Wu and C. H. Kuo, "Ultraviolet photodetectors made from SnO₂ nanowires," *Thin Solid Films*, vol. 517, no. 14, pp. 3870–3873, 2009.

Research Article

Employing Photoassisted Ligand Exchange Technique in Layered Quantum Dot LEDs

Wenjia Hu,^{1,2} Shuai Gao,^{1,2} Paras N. Prasad,³ Jingkang Wang,² and Jian Xu¹

¹ Chemical Engineering and Technology, Tianjin University, Tianjin 300072, China

² Engineering Science and Machines, The Pennsylvania State University, University Park, PA 16802, USA

³ Institute for Lasers, Photonics and Biophotonics, University at Buffalo, The State University of New York, Buffalo, NY 14260, USA

Correspondence should be addressed to Jian Xu, jianxu@engr.psu.edu

Received 28 August 2011; Accepted 31 October 2011

Academic Editor: Fan Zhang

Copyright © 2012 Wenjia Hu et al. This is an open access article distributed under the Creative Commons Attribution License, which permits unrestricted use, distribution, and reproduction in any medium, provided the original work is properly cited.

We presented in this paper a photoassisted ligand exchange approach whereby light will be introduced to facilitate the replacement of oleic acid (OA) ligand molecules over PbSe quantum dots (QDs). The ligand-exchanged QDs were used to fabricate quantum dot light-emitting-diodes (QD-LEDs), which outperform the devices comprising the QDs without ligand-replacement.

1. Introduction

Colloidal semiconductor quantum dots (QDs), by virtue of the large tunability in their bandgap, high luminance efficiency, narrow spectral emission, and high photostability, are promising lumophores and sensitizers in next-generation optoelectronic devices, such as light emitting diodes (LEDs) [1], photo detectors [2], and solar cells [3, 4]. However, the surface of the QDs is often capped with long-chain ligand molecules, which are electrically insulating and thus hinder the electronic applications of the QDs [5]. Ligand exchange with shorter and more conductive surfactant molecules is necessary for improved device performance (Our work (Nanotechnology) or D.Sargent's work). we reported in this communication the use of a photoassisted ligand exchange approach to facilitate the dot-to-dot electron transport, which results in a significant improvement in the output emission of QD-LEDs.

2. Experiment Details

PbSe QDs were synthesized following the noncoordinating solvent technique developed by Yu et al. [6]. The as prepared PbSe QDs, 4.5 nm in diameter and nearly monodisperse, were stabilized with a capping layer of oleate molecules coordinated to the Pb atoms (Figure 1). Ligand exchange processing of the PbSe QDs was based on the

method proposed by Won et al. [7]. 3 mL tert-butyl N-(2-mercaptoethyl)carbamate(t-BOC) and 15 mg/mL PbSe QDs in hexane solution (5 mL) were mixed in centrifuge tubes, and then vortexed overnight under nitrogen. Because the $-S-R_n$ in t-BOC has higher polarity than $-O-CO-R_n$ in oleic acid, the surface ligands of PbSe QDs will be replaced by t-BOC. Following ligand replacement, the QDs were washed twice with methanol using a centrifuge and then redispersed in chloroform. By this simple treatment the 18-carbon-chain oleate molecules overcoating the PbSe QDs were replaced with 4-carbon-chain 2-Mercaptoethylamine surfactants.

The design of the QD-LEDs was illustrated in Figure 2. A multilayer structure was employed in the device fabrication, consisting of ITO/poly(3,4-ethylenedioxythiophene) poly(styrenesulfonate) (PEDOT/PSS) (25 nm)/hole transport layer (HTL) (45 nm)/2-Mercaptoethylamine capped PbSe QD (~3 monolayers)/electron transport layer(ETL) (50 nm)/Al (150 nm). In the device, ITO/PEDOT/PSS was used as the anode. The HTL was solution-cast deposited from poly-(N,N'-bis(4-butylphenyl)-N,N'-bis(phenyl)benzidine) (poly-TPD) in chlorobenzene solution. The emissive layer of the device contains the mixture of ligand-exchanged QDs and PAG (di-tert-butylphenyliodonium perfluorobutanesulfonate) that was spin deposited from the chloroform solution. Processing of the emissive layer also involves the consecutive UV exposure (265 nm, 5 mins) and annealing at 120°C for an extended period. Tris

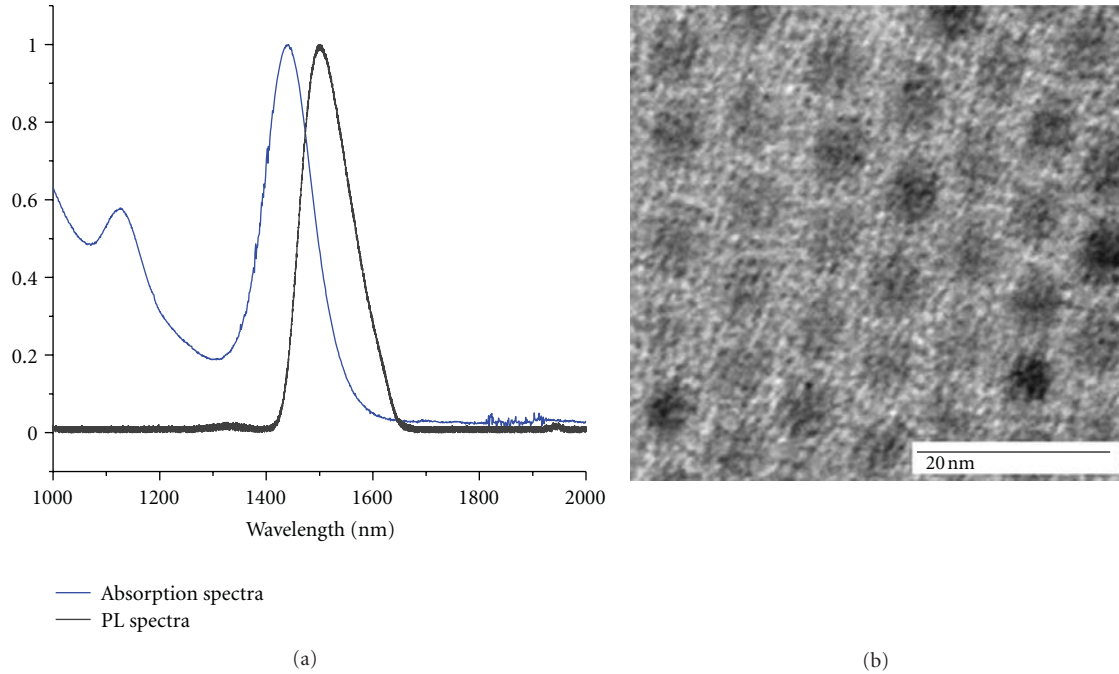


FIGURE 1: (a) Absorption and photoluminescence spectra of as prepared PbSe QDs; (b) TEM image of PbSe QDs with an average diameter of 4.5 nm.

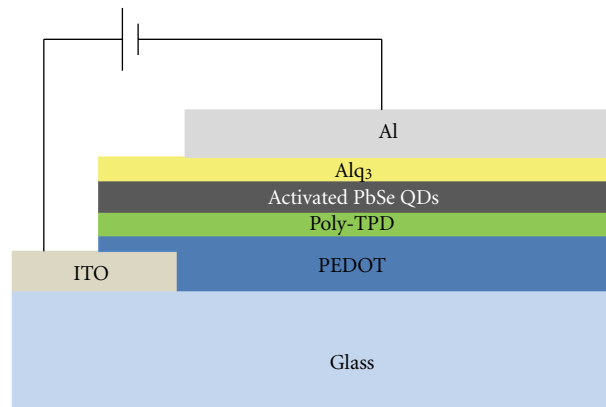


FIGURE 2: Schematic of a PbSe QD-LED device structure.

(8-hydroxyquinoline) aluminum (Alq_3) was evaporated over the QD layer as the ETL, and the shadow mask-evaporated aluminum film was used as the cathode.

The absorption spectra of the QD solution and films were recorded using a Perkin-Elmer Lambda 19 UV/VIS/NIR spectrometer. Photoluminescence (PL) spectra were measured by a CM110 Spectral-Products NIR spectrometer using a 980 nm diode laser module as the excitation source. The absorption and PL spectra were recorded at room temperature. The FTIR spectra of the QDs before and after ligand exchange were measured using a Bruker IFS 66/S FT-IR Spectrometer, A JEOL FasTEM-2010 transmission electron microscope (TEM) was used to image the crystal lattice of the QDs.

3. Result and Discussion

3.1. Surface Treatment of PbSe QDs. The PbSe QDs were stabilized with a capping layer of oleate molecules coordinated to the Pb atoms [8]. The 18-carbon long-chain structure renders the oleate molecules insulating and hinders the dot-to-dot transport of the free carriers in the QDs. Figure 3 illustrates the principle of changing the oleate molecules to the ones of shorter molecular chains and better conductivity: after initial treatment of t-BOC, the oleic acid ligands overcoating the PbSe QDs were replaced by t-BOC. Figure 4(a) displays the FTIR spectra before and after ligand exchange. Significant changes are clearly observed between the t-BOC-protected QDs and the oleic acid-capped QDs.

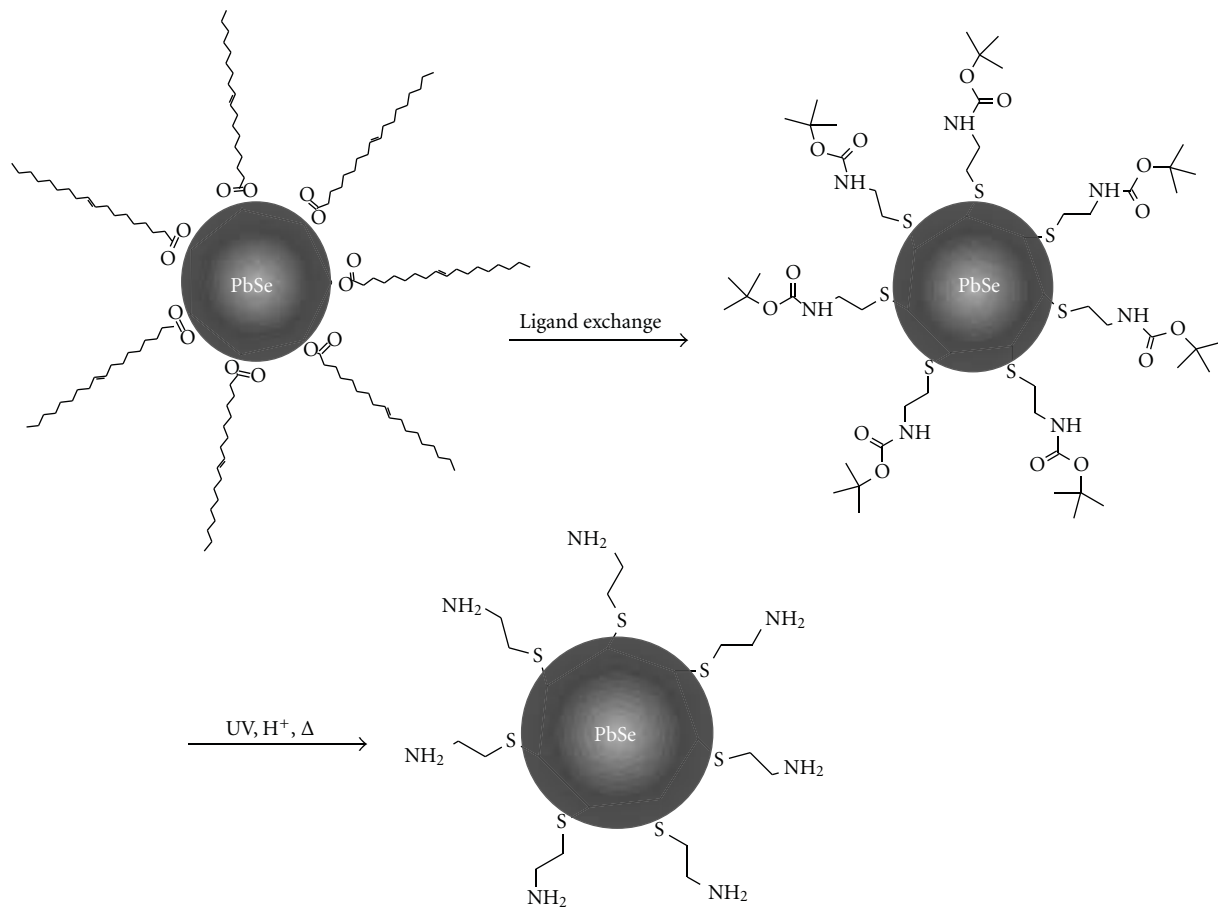


FIGURE 3: Scheme of ligand exchange process.

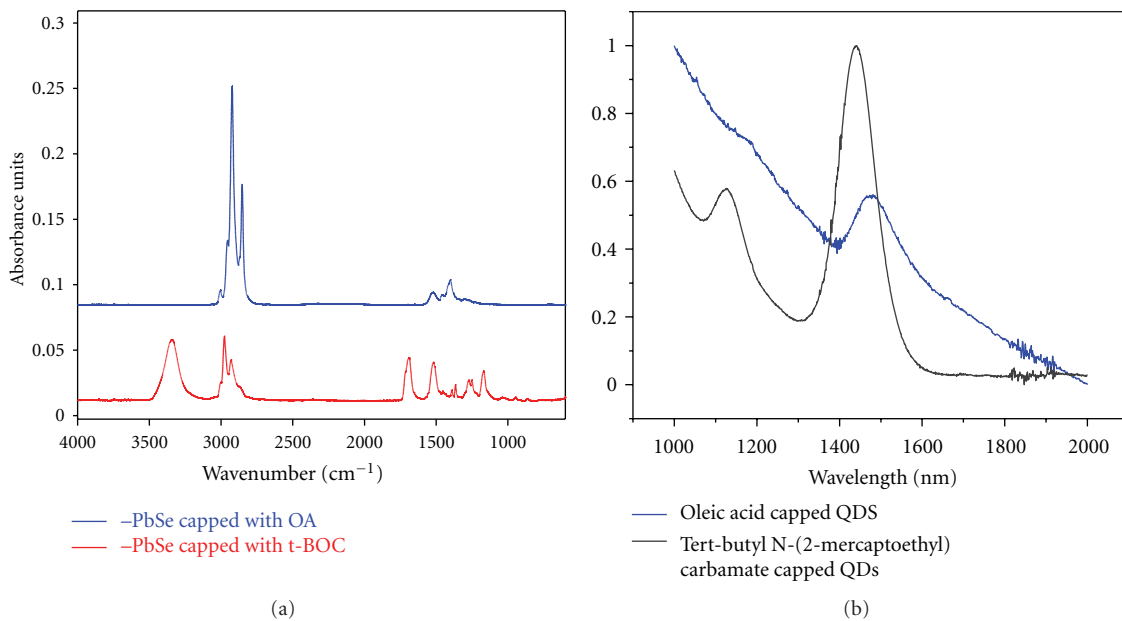


FIGURE 4: (a) FTIR spectra before and after ligand exchange. (b) Absorption spectra before and after ligand exchange.

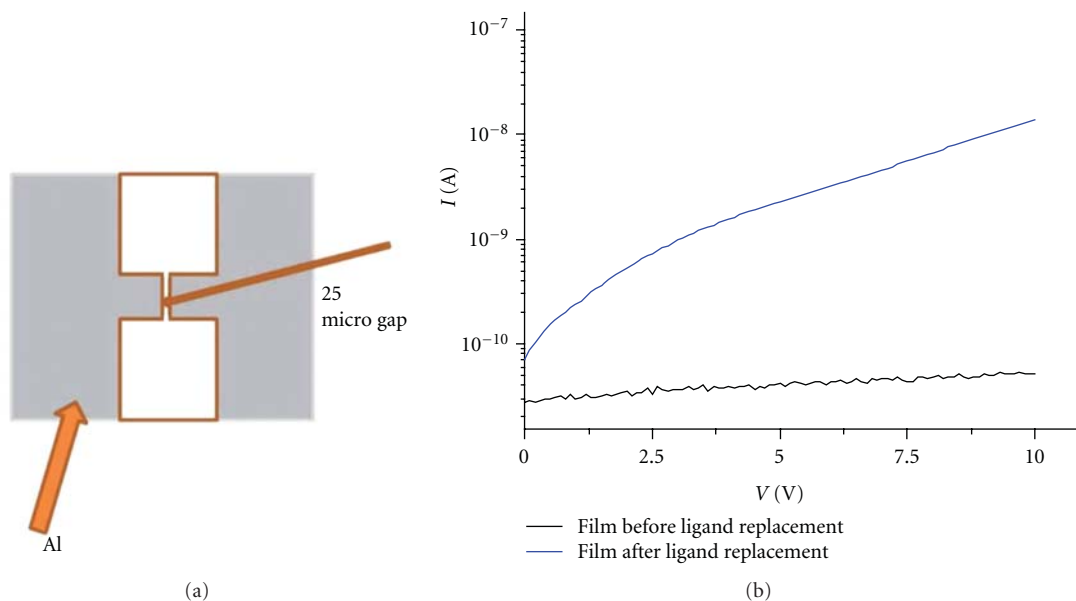


FIGURE 5: (a) The structure of the conductivity measurement. (b) I-V curve of the QDs before and after ligand exchange.

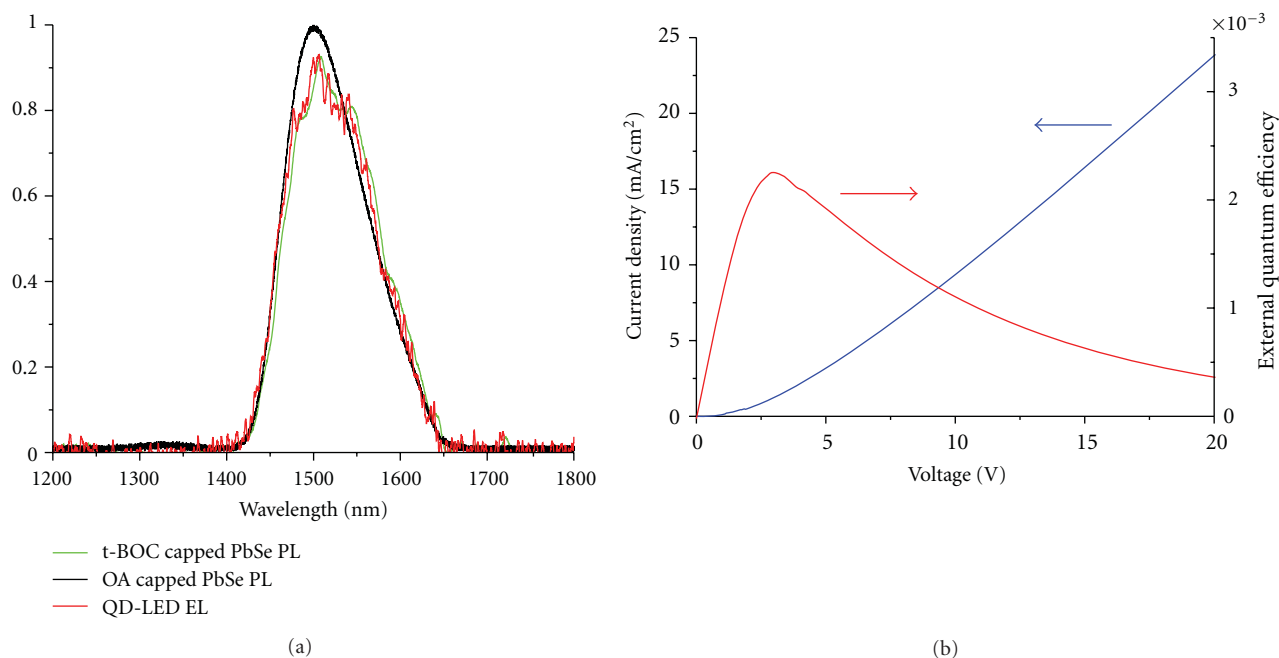


FIGURE 6: (a) PL spectra of the OA capped PbSe QDs (black) and the ligand-exchanged QDs (green); and EL spectrum of the QD-LED (red), (b) external quantum efficiency and current voltage plot for a PbSe QD-LED.

Specifically, the vibrational peak of the carbonyl hydrogen bonds below 3000 cm^{-1} decrease drastically as the long carbon chain was replaced by shorter carbon chain. The absorption peak at 3350 cm^{-1} arises, which can be attributed to the -NH vibrations of t-BOC. Figure 4(b) shows the absorption spectra of the QD solution. There is a slight red shift after ligand exchange due to the enhanced Stark effect that was induced by the variation of the surface-polarization energy during ligand replacement [9]. The new ligand t-BOC was

unstable. By reacting with the photochemically generated acid under UV irradiation, the chemical bond between -NH and -C=O cracked. Finally, the PbSe QDs were capped with 2-Mercaptoethylamine of a substantially reduced molecular chain length.

To measure the conductivity before and after ligand exchange, a gapped electrode structure was fabricated using fine gold filament as the shadow mask, as showed in Figure 5(a); PbSe QDs was drop-cast on top of the electrode gap

for the conduction measurement. Figure 5(b) compares the results of the conduction measurement for the samples with and without ligand exchange, showing that the conductivity of the ligand-exchanged PbSe QDs increased remarkably. This suggests that the ligand molecular length plays a key role for the carrier transport between the QDs under study.

3.2. PbSe QD-LED Characteristics. The NIR electroluminescence (EL) spectrum of the QD-LED closely resembles the photoluminescence (PL) of the ligand exchanged QDs as showed in Figure 6(a). It is noteworthy that the PL profile of the ligand-exchanged QDs exhibits a slight red shift from that of the as prepared PbSe QDs, which is consistent with the absorption spectra discussed previously.

For the sake of comparison, we have fabricated LED control samples using the PbSe QDs overcoated with oleate molecules. We did not observe any EL signal from the control samples. It is thus evident from our study that carrier transport across the QD surface was dramatically improved following the photoassisted ligand exchange process, which, in turn, leads to the enhanced injection and radiative recombination of electrons and holes in the nanoparticles. These experimental results proved that the ligand exchange method of the PbSe QDs strongly enhanced the injection and radiative recombination of electron and holes in the nanoparticle QDs in layered QD-LEDs. The accurate measurement of the QD-LED followed Steckel's method [10], the power efficiency of this device is no better than 0.1% (Figure 6(b)), implying that 99.9% of the power was converted to heat, while a large portion of the heat will be lost to the surrounding air by conduction and conversion process.

4. Conclusion

A photoassisted ligand exchange approach was employed to replace the oleic acid ligand on the surface of the QDs. The length of the carbon chain was successfully decreased by the photochemical reaction. Consequently, carrier transport across the QD surface was significantly enhanced. The surface-treated QDs were used to fabricate thin-film QD-LEDs, which results in improved LED performance over the untreated QD-LEDs.

Acknowledgments

The work at The Pennsylvania State University is being supported by the National Science Foundation under Grants of CMMI-0729263 and ECCS-0824186 and Army Research Office under Grant nos. 49653-EL and DURIP 2008-02-136.

References

- [1] Q. Sun, Y. A. Wang, L. S. Li et al., "Bright, multicoloured light-emitting diodes based on quantum dots," *Nature Photonics*, vol. 1, no. 12, pp. 717–722, 2007.
- [2] D. Qi, M. Fischbein, M. Drndić, and S. Šelmić, "Efficient polymer-nanocrystal quantum-dot photodetectors," *Applied Physics Letters*, vol. 86, no. 9, Article ID 093103, 2005.
- [3] I. Gur, N. A. Fromer, M. L. Geier, and A. P. Alivisatos, "Air-stable all-inorganic nanocrystal solar cells processed from solution," *Science*, vol. 310, no. 5747, p. 462, 2005.
- [4] Z. Tan, T. Zhu, M. Thein et al., "Integration of planar and bulk heterojunctions in polymer/nanocrystal hybrid photovoltaic cells," *Applied Physics Letters*, vol. 95, no. 6, Article ID 063510, 2009.
- [5] M. Law, J. M. Luther, Q. Song, B. K. Hughes, C. L. Perkins, and A. J. Nozik, "Structural, optical, and electrical properties of PbSe nanocrystal solids treated thermally or with simple amines," *Journal of the American Chemical Society*, vol. 130, no. 18, pp. 5974–5985, 2008.
- [6] W. W. Yu, J. C. Falkner, B. S. Shih, and V. L. Colvin, "Preparation and characterization of monodisperse PbSe semiconductor nanocrystals in a noncoordinating solvent," *Chemistry of Materials*, vol. 16, no. 17, pp. 3318–3322, 2004.
- [7] J. K. Won, J. K. Sung, K. S. Lee, M. Samoc, A. N. Cartwright, and P. N. Prasad, "Robust microstructures using UV photopatternable semiconductor nanocrystals," *Nano Letters*, vol. 8, no. 10, pp. 3262–3265, 2008.
- [8] I. Moreels, B. Fritzing, J. C. Martins, and Z. Hens, "Surface chemistry of colloidal PbSe nanocrystals," *Journal of the American Chemical Society*, vol. 130, no. 45, pp. 15081–15086, 2008.
- [9] Y. Zhang, Q. Dai, X. Li et al., "Formation of PbSe/CdSe Core/Shell nanocrystals for stable near-infrared high photoluminescence emission," *Nanoscale Research Letters*, vol. 5, no. 8, pp. 1279–1283, 2010.
- [10] J. S. Steckel, S. Coe-Sullivan, V. Bulović, and M. G. Bawendi, "1.1 to 1.55 μm tunable electroluminescence from PbSe quantum dots embedded within an organic device," *Advanced Materials*, vol. 15, no. 21, pp. 1862–1866, 2003.

Research Article

Facile Synthesis of Colloidal CuO Nanocrystals for Light-Harvesting Applications

Yee-Fun Lim, Joshua J. Choi, and Tobias Hanrath

School of Chemical and Biomolecular Engineering, Cornell University, Ithaca, NY 14853-1501, USA

Correspondence should be addressed to Tobias Hanrath, th358@cornell.edu

Received 25 May 2011; Accepted 14 July 2011

Academic Editor: Fan Zhang

Copyright © 2012 Yee-Fun Lim et al. This is an open access article distributed under the Creative Commons Attribution License, which permits unrestricted use, distribution, and reproduction in any medium, provided the original work is properly cited.

CuO is an earth-abundant, nontoxic, and low band-gap material; hence it is an attractive candidate for application in solar cells. In this paper, a synthesis of CuO nanocrystals by a facile alcoholothermal route is reported. The nanocrystals are dispersible in a solvent mixture of methanol and chloroform, thus enabling the processing of CuO by solution. A bilayer solar cell comprising of CuO nanocrystals and phenyl-C61-butyric acid methyl ester (PCBM) achieved a power conversion efficiency of 0.04%, indicating the potential of this material for light-harvesting applications.

1. Introduction

Solution-processable solar cell technologies can enable the realization of low-cost and high-throughput photovoltaic production [1]. While much work has previously focused on organic semiconductors [1], colloidal inorganic semiconductor nanocrystals (NCs) are starting to attract attention for photovoltaic applications [2]. NCs have the advantages of being solution-processable, capable of absorbing a large fraction of the solar spectrum, and tunable band-gap due to quantum-confinement effects [2]. While early NC solar cell work was based on CdSe [3] and CdTe [4], impressive results have been achieved with CuInSe₂ [5], PbSe [6–10], and PbS [11–15] NCs in recent years. In particular, Sargent and coworkers have reported a PbS NC/TiO₂ bi-layer solar cell with a power conversion efficiency (PCE) as high as 5.1% [15].

The above-mentioned materials may be good test-beds for studies of NCs as photovoltaic materials but may not be feasible candidates for wide-spread deployment due to toxicity and availability—Cd and Pb are toxic heavy metals, while In and Te are among the least abundant elements in the Earth's crust [16]. It is thus desirable to explore other alternative solar cell materials. Copper- and iron-based semiconductors have emerged as attractive materials from an analysis by Wadia et al. based on abundance and cost [17].

For instance, Wu et al. [18] recently reported a Cu₂S NC-based solar cell with a promising PCE of 1.6%. Copper (I) oxide (Cu₂O) and copper (II) oxide (CuO) are also attractive candidates for light-harvesting applications due to their band gap energies of 1.4 eV (indirect) for CuO [19] and 2.0 eV (direct) for Cu₂O [20] that are quite close to the ideal band-gap for a single junction photovoltaic cell estimated from detailed balance [21]. Cu₂O has been investigated as a solar cell material for several decades [22], with recent reports of PCE up to 2.0% [23–25]. CuO has been employed in photo-electrochemical cells [26, 27] and as a cathode for dye-sensitized solar cells [28]. The use of CuO as the active layer in solid state solar cells has, to the best of our knowledge, not yet been investigated, and is the focus of this work. From a detailed balance analysis, CuO with a band gap of 1.4 eV can reach an ultimate solar cell efficiency of almost 30%, significantly higher than the 20% limit for Cu₂O (2.0 eV band gap) [21].

Copper oxide NC syntheses via various routes have been reported in the literature [29–44]. Relatively few of these reports, however, discuss the dispersibility of copper oxide NCs in common solvents [41–44], which is critical for solution-based processing of NC thin film absorber layers. In particular, Yuhas and Yang [43] and Hung et al. [44] reported solar cells based on films spin-coated from Cu₂O NC solutions, with PCE from 0.05% to 0.14%. In this

paper, the synthesis of colloidal CuONCs by a facile alcoholthermal method is reported. The NCs are characterized by transmission electron microscopy (TEM), X-ray diffraction (XRD), Fourier transform infrared spectroscopy (FTIR), and UV-visible absorption spectroscopy. Finally, as a proof of concept, a bilayer solar cell-based on CuO and phenyl-C₆₁-butyric acid methyl ester (PCBM) is demonstrated.

2. Experimental

2.1. Synthesis of CuONCs. 0.29 g of copper (II) acetate (Sigma Aldrich) was added to 30 mL of reagent alcohol (Sigma Aldrich) under vigorous stirring. 1 mL of deionized (DI) water was added, and the mixture was heated to 75°C. In a separate container, 1.3 mL of 25% tetramethylammonium hydroxide (TMAH) in methanol (Sigma Aldrich) was added to 10 mL of reagent alcohol. After 15 minutes of stirring, when the copper acetate has fully dissolved, the TMAH solution was gradually added over 5 minutes in regular intervals. The reaction was allowed to proceed at 75°C for 60 minutes, and the resultant product was collected by precipitation with hexane and then centrifuging at 3750 rpm for 5 minutes.

2.2. NC Characterization. TEM samples were prepared by drop-casting very dilute NC suspensions in methanol onto carbon grids (Electron Microscopy Sciences), and images were taken using an FEI T12 Spirit TEM. X-ray diffraction was performed on a Bruker General Area Detector Diffraction System (GADDS). A Thermo Scientific Nicolet iS10 FT-IR spectrometer was used to perform FTIR spectroscopy on NC samples drop-casted from methanol. These NCs have been washed and centrifuged three times with reagent alcohol to get rid of unreacted precursors. UV-visible absorption spectroscopy was performed using a Shimadzu UV-3101PC UV/Vis/Near-IR Spectrophotometer. All film thickness measurements were done using a Tencor P10 Profilometer.

2.3. Solar Cell Fabrication and Testing. Solar cells were fabricated on prepatterned indium tin oxide (ITO) coated glass substrates (Kintec, Hong Kong), which were cleaned by sonication in a mild detergent, rinsed in deionized water, dried in a nitrogen stream, and treated with a 10-minute UV-ozone exposure. CuO NCs were dispersed in a solvent mixture of 2 : 1 chloroform and methanol at a concentration of ~10 mg mL⁻¹, and then spin-coated on top of the ITO at 2000 rpm to give a film ~40 nm thick. A cell with a thicker CuO layer (~70 nm) was also fabricated by performing the spin-coating step 3 times. This is possible because the underlying layer is not completely dissolved during the spin-coating of subsequent layers. PCBM solution (20 mg mL⁻¹ in chloroform) was then spin-coated on top of the CuO at 2000 rpm to give a film ~120 nm thick. Finally, 4 Å of CsF and 400 Å of Al were thermally evaporated under high vacuum (~10⁻⁶ Torr) to form the cathode for the devices. A shadow mask was used in the evaporation to define a device-active area of 3 mm². Control PCBM-only solar cells (without CuO) were also fabricated.

Device current-voltage curves were obtained with a Keithley 236 source-measurement-unit (SMU) in the dark and as well as under AM 1.5 100 mW cm⁻² illumination from a Solar Light 16S-002 solar simulator. Light output power was calibrated using a Newport 818P-010-12 thermopile high power detector, which has a flat response over a broad spectral range. EQE measurements were performed using a Newport 1000 W xenon lamp coupled to an Oriol Cornerstone 260 1/4 m monochromator as the light source, a Keithley 236 SMU to measure short circuit current, and a Newport 918D-UV3-OD3 low power detector to monitor the light intensity.

3. Results and Discussion

The CuONC synthesis is modified from a previously reported method for the synthesis of soluble zinc oxide NCs [9, 45]. Copper (II) acetate, Cu(OAc)₂, was dissolved in reagent alcohol and then reacted with tetramethylammonium hydroxide (TMAH) to form copper (II) hydroxide. CuO was then formed through heating:

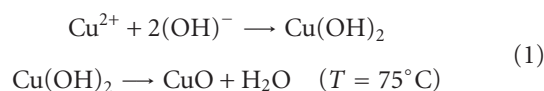


Figure 1(a) shows TEM image of CuO NCs, in which it can be seen that they have a rather large size distribution of around 4-5 nm. The relatively broad size distribution of the CuONCs is likely the result of the nucleation and growth dynamics of the reaction. Unlike the “hot-injection” synthesis [46], the simplified alcoholthermal method lacks a single well-defined nucleation event leading to broader NC diameter distributions. X-ray diffractograms (Figure 1(b)) of the NCs are consistent with the literature values for CuO (JPCD no. 05-0661). It was observed that the addition of a small amount of deionized (DI) water (3% by volume) during the CuO synthesis produced NCs with more well-defined and narrower XRD peaks as compared to NCs synthesized without water. In previously reported syntheses of ZnO nanoparticles with zinc acetate in alcohol [47, 48], it was observed that the role of water was to increase the concentration of Zn²⁺ ions in the solution, since zinc acetate is more soluble in water than alcohol [47, 48]. Thus, it seems reasonable to arrive at a similar conclusion for the CuO synthesis, that the role of water is to promote the forward reaction due to a higher concentration of Cu²⁺ ions in the solution. Fits of the XRD peaks to the Scherrer equation for the NCs synthesized with water gave a CuONC size of (5.1 ± 0.8) nm, which is consistent with the average NC size discerned from the TEM image.

Importantly, the CuO NCs can be dispersed in a 2 : 1 solvent mixture of chloroform and methanol (see inset in Figure 1(a)). To understand the dispersion behavior, the NC surface chemistry and surface bound species were investigated using infrared spectroscopy. Figure 2 shows an FTIR spectrum of drop-casted CuO NCs. The peak at 1560 cm⁻¹ is rather difficult to assign since both the water H-O-H scissoring vibration and the carboxylate anion asymmetrical stretching fall within this range [49], but both should be

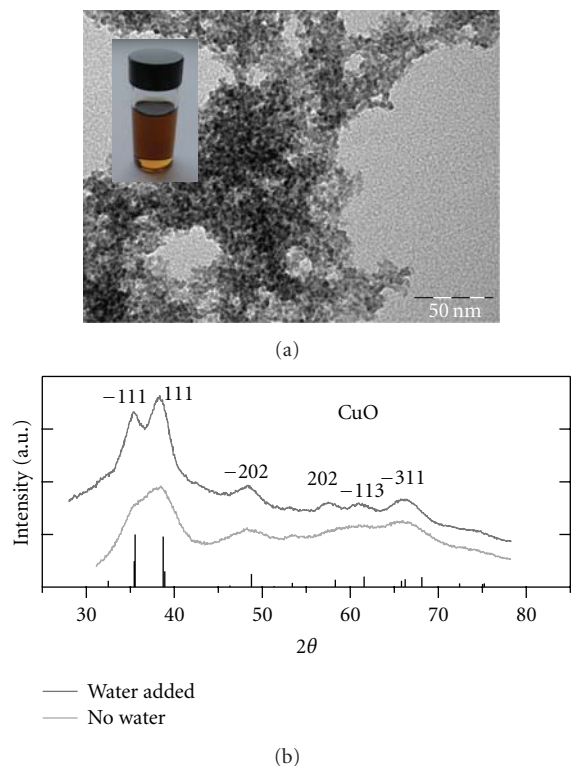


FIGURE 1: (a) TEM image of CuO NCs, (b) X-ray diffractograms of CuO NCs, with comparison between 2 syntheses: one with water added and the other without any water. The black lines represent literature values for CuO (JPCD# 05-0661). Inset shows a dispersion of CuO NCs in a solvent mixture of methanol and chloroform.

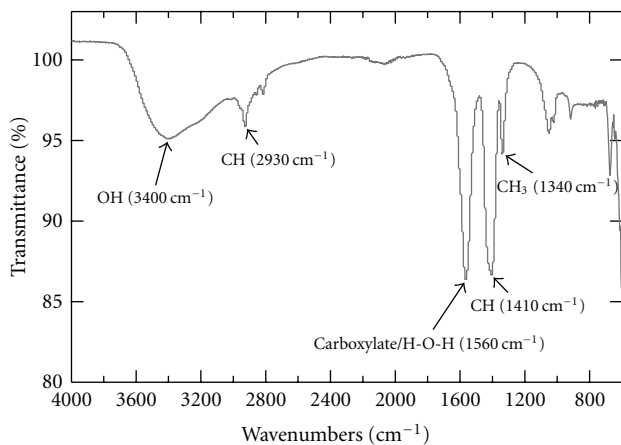


FIGURE 2: FTIR spectrum of CuO NCs.

represented since they are both present in the reaction. The data thus suggests that acetate (accounting for both the carboxylate and CH peaks), hydroxide, and water molecules from the synthesis are adsorbed onto the NC surfaces. The presence of both polar and organic groups explains why the CuO NCs can be readily dispersed in the chloroform and methanol mixture.

Figure 3(a) shows the absorption spectra of CuO (80 nm) and PCBM (120 nm) films spin-casted from dispersions in their respective solvents. The CuO film absorption data was used to generate Tauc plots to determine the energy gap of the NCs (Figures 3(b) and 3(c)), which indicate a direct energy-gap at 3.07 eV and an indirect energy-gap at 1.40 eV. The latter value is similar to the value for the indirect bulk band-gap reported in the literature [19]. While there have been reports of quantum confinement observed in CuO nanostructures [33, 35], the authors did not perform an indirect energy-gap fit to their data; hence it is difficult to make meaningful comparisons.

As a proof of concept of the potential applications of the CuO NCs, a bilayer solar cell comprising of CuO and a fullerene derivative, phenyl- C_{61} -butyric acid methyl ester (PCBM), was fabricated. A single layer of CuO is unsuitable as the active layer, since the NC film contains cracks and pinholes and will result in a short-circuited device. This is similar to what has been reported about PbSe NC films, which require multiple sequential depositions of NCs and cross-linking to fill up the cracks [6]. PCBM is chosen since it is the acceptor of choice in solution-processable polymer solar cells [50], and its good film forming property allows it to cover up cracks in the CuO film. The literature value energy levels of the conduction and valence bands of CuO [19] and the lowest unoccupied molecular orbital (LUMO) and highest occupied molecular orbital (HOMO) of PCBM [51] are such that CuO and PCBM form a type II semiconductor heterojunction; hence they are suitable as a donor and acceptor pair. Figure 4(a) shows a schematic of the device stack with indium tin oxide (ITO) forming the anode and CsF/Al as the cathode, as well as the literature values for the semiconductor energy levels [19, 51, 52]. Assignment of bulk CuO energy levels is supported by the small difference in NC optical band-gap relative to the literature (bulk) values [19].

Figure 4(b) shows the device current density voltage (J - V) curves both in the dark and light (under AM 1.5 100 $mW\ cm^{-2}$ illumination) of a bi-layer cell with a ~ 40 nm thick CuO layer. The device is characterized by a V_{OC} of 0.44 V, J_{SC} of 0.24 $mA\ cm^{-2}$, fill factor (FF) of 0.38, and a power conversion efficiency (PCE) of 0.040%. As a control, a PCBM-only cell (without CuO) was fabricated and tested (also shown in Figure 4(b)). It shows a much lower J_{SC} of 0.03 $mA\ cm^{-2}$ and PCE of 0.011%, although it gave a higher V_{OC} of 0.78 V and slightly higher FF of 0.41. Meanwhile, a bi-layer cell with a thicker CuO (~ 70 nm) layer is characterized by poorer J_{SC} (0.15 $mA\ cm^{-2}$), FF (0.35), and PCE (0.024%) compared to the cell with thinner CuO (refer to Table 1 for a summary of device results). These results lead to the conclusion that efficient charge collection is only taking place in the thin CuO layer near the interface, and additional CuO layer thickness does not contribute to the photocurrent while possibly adding to series resistance and recombination as indicated by the poorer FF. Improvements in the charge collection from CuO NC absorber layers will therefore require better charge transport characteristics within the NC layer. One possible route to improving the charge collection is to use semiconductor nanowires (such

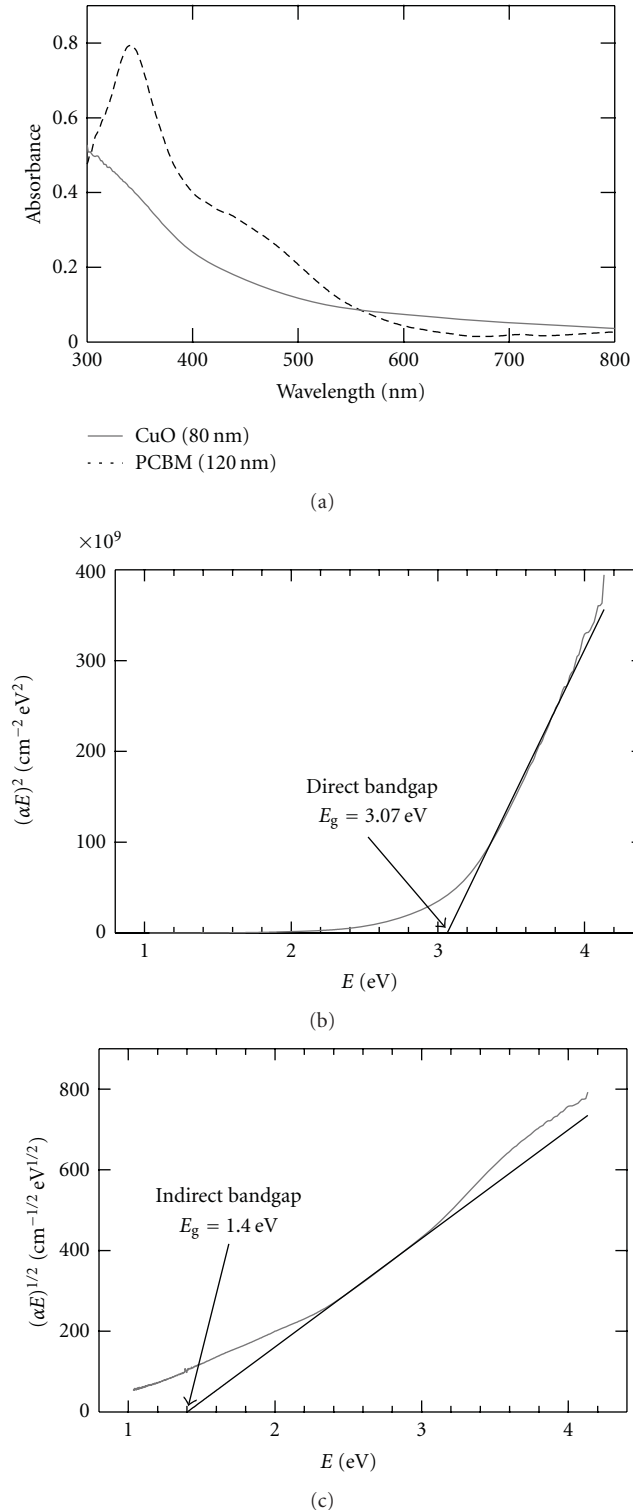


FIGURE 3: Optical properties of CuO NCs: (a) UV-Visible absorption spectra for spin-casted CuO and PCBM films (b) Tauc plot for the direct CuO band-gap fit (c) Indirect band-gap Tauc plot fit.

as n-type ZnO or TiO₂) as the acceptor material, and the CuO NCs are then infiltrated into the gaps of the nanowires. Such device architectures have the advantage of separating

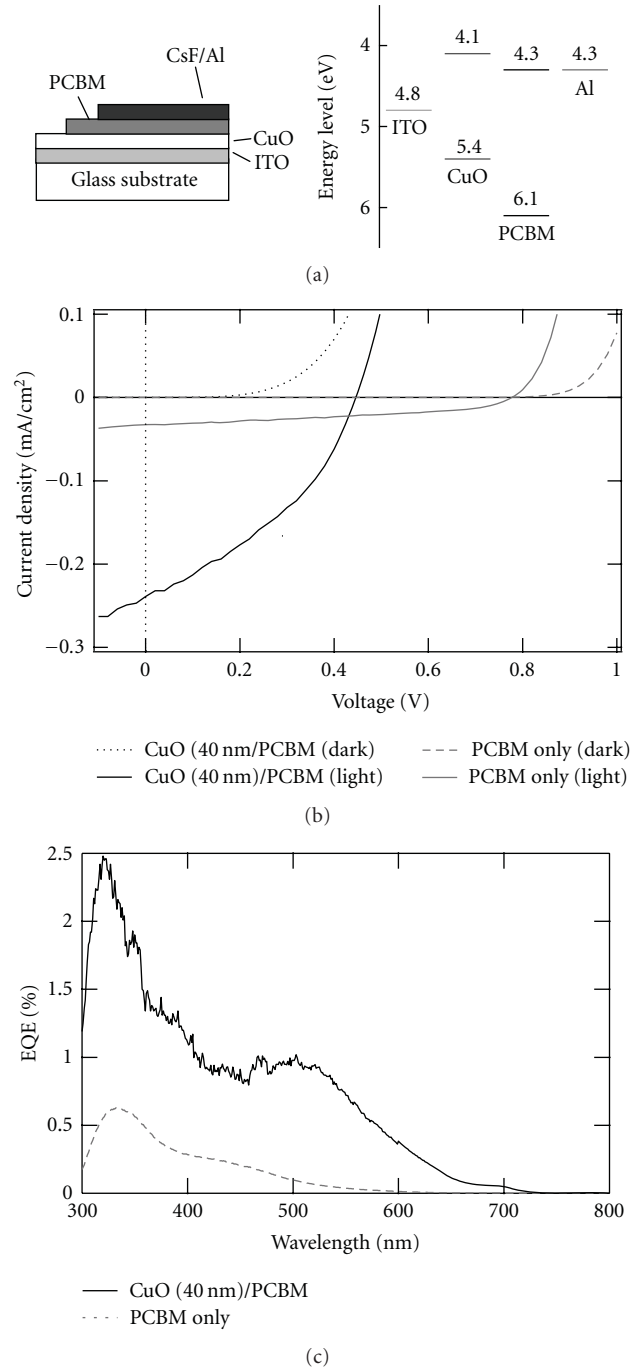


FIGURE 4: Performance of a CuO/PCBM bilayer solar cell: (a) Device stack and energy level diagram, (b) J - V curves in the dark and light (AM 1.5 100 mW cm⁻²), (c) EQE comparison between the bilayer cell and a PCBM only cell.

the light absorption and charge collection pathways so that both processes can be efficient [8].

External quantum efficiency (EQE) spectra of the devices are shown in Figure 4(c). The bi-layer cell shows a superior EQE to the PCBM-only cell, and the improved EQE at higher wavelengths beyond 550 nm can be attributed to the contribution from the CuO by taking into account the

TABLE 1: Summary of solar cell device results.

Active layer	V_{OC} (V)	J_{SC} (mA/cm ²)	Fill Factor	PCE (%)
CuO (40 nm)/PCBM	0.44	0.24	0.38	0.040
CuO (70 nm)/PCBM	0.46	0.15	0.35	0.024
PCBM only	0.78	0.03	0.41	0.011

absorption spectra of both materials (Figure 3(a)). Since J_{SC} is the integration of the EQE across the solar spectrum, the higher J_{SC} observed in the bi-layer cell is clearly due to its superior EQE.

4. Conclusions

A synthesis of CuONCs by a facile alcohothermal route has been presented. The CuO NCs are soluble in a chloroform/methanol mixture, thus enabling the processing of these materials by solution. A bi-layer CuO and PCBM solar cell achieved a power conversion efficiency of 0.04%, which is 4 times higher than the control PCBM-only cell, indicating the potential of these CuONCs for light-harvesting applications.

Acknowledgments

This work was funded by the KAUST-Cornell Center for Energy and Sustainability. The authors thank Dr. Jacek Jasieniak (CSIRO, Australia) for inspiration for the copper oxide synthesis and helpful comments on the paper, William Baumgardner and John Grazul for assistance with TEM imaging, and Dr. Maura Weathers for assistance with XRD. Device fabrication and testing was performed partly in the laboratory of Professor George Malliaras, while nanocrystal characterization was done using equipment in the Cornell Center for Materials Research (CCMR), Cornell Center for Nanoscale Systems (CNS), Cornell Nanoscale Science & Technology Facility (CNF), and the KAUST-Cornell Center for Energy and Sustainability. Y. F. Lim acknowledges a research fellowship from A*STAR, Singapore. J. J. Choi acknowledges support from NSF IGERT fellowship.

References

- [1] C. J. Brabec and J. R. Durrant, "Solution-processed organic solar cells," *MRS Bulletin*, vol. 33, no. 7, pp. 670–675, 2008.
- [2] J. Tang and E. H. Sargent, "Infrared colloidal quantum dots for photovoltaics: fundamentals and recent progress," *Advanced Materials*, vol. 23, no. 1, pp. 12–29, 2011.
- [3] W. U. Huynh, J. J. Dittmer, and A. P. Alivisatos, "Hybrid nanorod-polymer solar cells," *Science*, vol. 295, no. 5564, pp. 2425–2427, 2002.
- [4] I. Gur, N. A. Fromer, M. L. Geier, and A. P. Alivisatos, "Materials science: air-stable all-inorganic nanocrystal solar cells processed from solution," *Science*, vol. 310, no. 5747, pp. 462–465, 2005.
- [5] Q. Guo, S. J. Kim, M. Kar et al., "Development of CuInSe₂ nanocrystal and nanoring inks for low-cost solar cells," *Nano Letters*, vol. 8, no. 9, pp. 2982–2987, 2008.
- [6] J. M. Luther, M. Law, M. C. Beard et al., "Schottky solar cells based on colloidal nanocrystal films," *Nano Letters*, vol. 8, no. 10, pp. 3488–3492, 2008.
- [7] K. S. Leschkies, T. J. Beatty, M. S. Kang, D. J. Norris, and E. S. Aydil, "Solar cells based on junctions between colloidal Pbse nanocrystals and thin ZnO films," *ACS Nano*, vol. 3, no. 11, pp. 3638–3648, 2009.
- [8] K. S. Leschkies, A. G. Jacobs, D. J. Norris, and E. S. Aydil, "Nanowire-quantum-dot solar cells and the influence of nanowire length on the charge collection efficiency," *Applied Physics Letters*, vol. 95, no. 19, Article ID 193103, 2009.
- [9] J. J. Choi, Y. F. Lim, M. B. Santiago-Berrios et al., "PbSe Nanocrystal Excitonic Solar Cells," *Nano Letters*, vol. 9, no. 11, pp. 3749–3755, 2009.
- [10] C. Y. Kuo, M. S. Su, Y. C. Hsu, H. N. Lin, and K. H. Wei, "An organic hole transport layer enhances the performance of colloidal PbSe quantum dot photovoltaic devices," *Advanced Functional Materials*, vol. 20, no. 20, pp. 3555–3560, 2010.
- [11] J. M. Luther, J. Gao, M. T. Lloyd, O. E. Semonin, M. C. Beard, and A. J. Nozik, "Stability assessment on a 3% bilayer PbS/ZnO quantum dot heterojunction solar cell," *Advanced Materials*, vol. 22, no. 33, pp. 3704–3707, 2010.
- [12] J. J. Choi, W. Wenger, R. Hoffman et al., "Solution-processed nanocrystal quantum dot tandem solar cells," *Advanced Materials*, vol. 23, no. 28, pp. 3144–3148, 2011.
- [13] S. W. Tsang, H. Fu, J. Ouyang et al., "Self-organized phase segregation between inorganic nanocrystals and PC₆₁BM for hybrid high-efficiency bulk heterojunction photovoltaic cells," *Applied Physics Letters*, vol. 96, no. 24, Article ID 243104, 2010.
- [14] R. Debnath, J. Tang, D. A. Barkhouse et al., "Ambient-processed colloidal quantum dot solar cells via individual pre-encapsulation of nanoparticles," *Journal of the American Chemical Society*, vol. 132, no. 17, pp. 5952–5953, 2010.
- [15] A. G. Pattantyus-Abraham, I. J. Kramer, A. R. Barkhouse et al., "Depleted-heterojunction colloidal quantum dot solar cells," *ACS Nano*, vol. 4, no. 6, pp. 3374–3380, 2010.
- [16] P. H. Stauffer and J. W. Hendley II, "Rare Earth Elements—Critical Resources for High Technology," USGS Fact Sheet 087-02, 2011, <http://pubs.usgs.gov/fs/2002/fs087-02>.
- [17] C. Wadia, A. P. Alivisatos, and D. M. Kammen, "Materials availability expands the opportunity for large-scale photovoltaics deployment," *Environmental Science and Technology*, vol. 43, no. 6, pp. 2072–2077, 2009.
- [18] Y. Wu, C. Wadia, W. Ma, B. Sadler, and A. P. Alivisatos, "Synthesis and photovoltaic application of copper(I) sulfide nanocrystals," *Nano Letters*, vol. 8, no. 8, pp. 2551–2555, 2008.
- [19] F. P. Koffyberg and F. A. Benko, "A photoelectrochemical determination of the position of the conduction and valence band edges of p-type CuO," *Journal of Applied Physics*, vol. 53, no. 2, pp. 1173–1177, 1982.
- [20] G. Nagasubramanian, A. S. Gioda, and A. J. Bard, "Semiconductor electrodes—37. Photoelectrochemical behavior of p-type Cu/sub 2/O in acetonitrile solutions," *Journal of the Electrochemical Society*, vol. 128, no. 10, pp. 2158–2164, 1981.
- [21] W. Shockley and H. J. Queisser, "Detailed balance limit of efficiency of p-n junction solar cells," *Journal of Applied Physics*, vol. 32, no. 3, pp. 510–519, 1961.
- [22] B. P. Rai, "Cu₂O solar cells: a review," *Solar Cells*, vol. 25, no. 3, pp. 265–272, 1988.

- [23] T. Minami, H. Tanaka, T. Shimakawa, T. Miyata, and H. Sato, "High-efficiency oxide heterojunction solar cells using Cu_2O sheets," *Japanese Journal of Applied Physics*, vol. 43, no. 7A, pp. L917–L919, 2004.
- [24] T. Minami, T. Miyata, K. Ihara, Y. Minamino, and S. Tsukada, "Effect of ZnO film deposition methods on the photovoltaic properties of $\text{ZnO-Cu}_2\text{O}$ heterojunction devices," *Thin Solid Films*, vol. 494, no. 1-2, pp. 47–52, 2006.
- [25] A. Mittiga, E. Salza, F. Sarto, M. Tucci, and R. Vasanthi, "Heterojunction solar cell with 2% efficiency based on a Cu_2O substrate," *Applied Physics Letters*, vol. 88, no. 16, Article ID 163502, 2006.
- [26] K. H. Yoon, W. J. Choi, and D. H. Kang, "Photoelectrochemical properties of copper oxide thin films coated on an n-Si substrate," *Thin Solid Films*, vol. 372, no. 1, pp. 250–256, 2000.
- [27] Y. S. Chaudhary, A. Agrawal, R. Shrivastav, V. R. Satsangi, and S. Dass, "A study on the photoelectrochemical properties of copper oxide thin films," *International Journal of Hydrogen Energy*, vol. 29, no. 2, pp. 131–134, 2004.
- [28] S. Anandan, X. Wen, and S. Yang, "Room temperature growth of CuO nanorod arrays on copper and their application as a cathode in dye-sensitized solar cells," *Materials Chemistry and Physics*, vol. 93, no. 1, pp. 35–40, 2005.
- [29] C. H. Kuo and M. H. Huang, "Morphologically controlled synthesis of Cu_2O nanocrystals and their properties," *Nano Today*, vol. 5, no. 2, pp. 106–116, 2010.
- [30] M. Cao, C. Hu, Y. Wang, Y. Guo, C. Guo, and E. Wang, "A controllable synthetic route to Cu , Cu_2O , and CuO nanotubes and nanorods," *Chemical Communications*, vol. 9, no. 15, pp. 1884–1885, 2003.
- [31] W. Wang, Z. Liu, Y. Liu, C. Xu, C. Zheng, and G. Wang, "A simple wet-chemical synthesis and characterization of CuO nanorods," *Applied Physics A: Materials Science and Processing*, vol. 76, no. 3, pp. 417–420, 2003.
- [32] Y. Chang and H. C. Zeng, "Controlled synthesis and self-assembly of single-crystalline CuO nanorods and nanoribbons," *Crystal Growth and Design*, vol. 4, no. 2, pp. 397–402, 2004.
- [33] J. Zhu, H. Chen, H. Liu, X. Yang, L. Lu, and X. Wang, "Needle-shaped nanocrystalline CuO prepared by liquid hydrolysis of $\text{Cu}(\text{OAc})_2$," *Materials Science and Engineering A*, vol. 384, no. 1-2, pp. 172–176, 2004.
- [34] Y. Yu, F. P. Du, J. C. Yu, Y. Y. Zhuang, and P. K. Wong, "One-dimensional shape-controlled preparation of porous Cu_2O nano-whiskers by using CTAB as a template," *Journal of Solid State Chemistry*, vol. 177, no. 12, pp. 4640–4647, 2004.
- [35] H. Fan, L. Yang, W. Hua et al., "Controlled synthesis of monodispersed CuO nanocrystals," *Nanotechnology*, vol. 15, no. 1, pp. 37–42, 2004.
- [36] C. Lu, L. Qi, J. Yang et al., "One-pot synthesis of octahedral Cu_2O nanocages via a catalytic solution route," *Advanced Materials*, vol. 17, no. 21, pp. 2562–2567, 2005.
- [37] P. He, X. Shen, and H. Gao, "Size-controlled preparation of Cu_2O octahedron nanocrystals and studies on their optical absorption," *Journal of Colloid and Interface Science*, vol. 284, no. 2, pp. 510–515, 2005.
- [38] J. Zhang, J. Liu, Q. Peng, X. Wang, and Y. Li, "Nearly monodisperse Cu_2O and CuO nanospheres: Preparation and applications for sensitive gas sensors," *Chemistry of Materials*, vol. 18, no. 4, pp. 867–871, 2006.
- [39] J. Y. Ho and M. H. Huang, "Synthesis of submicrometer-sized Cu_2O crystals with morphological evolution from cubic to hexapod structures and their comparative photocatalytic activity," *Journal of Physical Chemistry C*, vol. 113, no. 32, pp. 14159–14164, 2009.
- [40] K. X. Yao, X. M. Yin, T. H. Wang, and H. C. Zeng, "Synthesis, self-assembly, disassembly, and reassembly of two types of Cu_2O nanocrystals uniaxially with 001 or 110 planes," *Journal of the American Chemical Society*, vol. 132, no. 17, pp. 6131–6144, 2010.
- [41] M. Yin, C. K. Wu, Y. Lou et al., "Copper oxide nanocrystals," *Journal of the American Chemical Society*, vol. 127, no. 26, pp. 9506–9511, 2005.
- [42] T. Kida, T. Oka, M. Nagano, Y. Ishiwata, and X. G. Zheng, "Synthesis and application of stable copper oxide nanoparticle suspensions for nanoparticulate film fabrication," *Journal of the American Ceramic Society*, vol. 90, no. 1, pp. 107–110, 2007.
- [43] B. D. Yuhas and P. Yang, "Nanowire-based all-oxide solar cells," *Journal of the American Chemical Society*, vol. 131, no. 10, pp. 3756–3761, 2009.
- [44] L. L. Hung, C. K. Tsung, W. Huang, and P. Yang, "Room-temperature formation of hollow Cu_2O nanoparticles," *Advanced Materials*, vol. 22, no. 17, pp. 1910–1914, 2010.
- [45] W. J. E. Beek, M. M. Wienk, M. Kemerink, X. Yang, and R. A. J. Janssen, "Hybrid zinc oxide conjugated polymer bulk heterojunction solar cells," *Journal of Physical Chemistry B*, vol. 109, no. 19, pp. 9505–9516, 2005.
- [46] C. B. Murray, D. J. Norris, and M. G. Bawendi, "Synthesis and characterization of nearly monodisperse CdE ($\text{E} = \text{sulfur}$, selenium , tellurium) semiconductor nanocrystallites," *Journal of the American Chemical Society*, vol. 115, no. 19, pp. 8706–8715, 1993.
- [47] E. A. Meulenkaamp, "Synthesis and growth of ZnO nanoparticles," *Journal of Physical Chemistry B*, vol. 102, no. 29, pp. 5566–5572, 1998.
- [48] M. S. Tokumoto, S. H. Pulcinelli, C. V. Santilli, and V. Briois, "Catalysis and temperature dependence on the formation of ZnO nanoparticles and of zinc acetate derivatives prepared by the sol-gel route," *Journal of Physical Chemistry B*, vol. 107, no. 2, pp. 568–574, 2003.
- [49] R. M. Silverstein and F. X. Webster, *Spectrometric Identification of Organic Compounds*, John Wiley & Sons, New York, NY, USA, 1998.
- [50] C. J. Brabec, S. Gowrisanker, J. J. M. Halls, D. Laird, S. Jia, and S. P. Williams, "Polymer-fullerene bulk-heterojunction solar cells," *Advanced Materials*, vol. 22, no. 34, pp. 3839–3856, 2010.
- [51] Y. K. Jin, K. Lee, N. E. Coates et al., "Efficient tandem polymer solar cells fabricated by all-solution processing," *Science*, vol. 317, no. 5835, pp. 222–225, 2007.
- [52] K. Sugiyama, H. Ishii, Y. Ouchi, and K. Seki, "Dependence of indium-tin-oxide work function on surface cleaning method as studied by ultraviolet and x-ray photoemission spectroscopies," *Journal of Applied Physics*, vol. 87, no. 1, pp. 295–298, 2000.

Research Article

Gold Nanoparticle Sensor for the Visual Detection of Pork Adulteration in Meatball Formulation

M. E. Ali,¹ U. Hashim,¹ S. Mustafa,² Y. B. Che Man,² and Kh. N. Islam³

¹Institute of Nano Electronic Engineering, Universiti Malaysia Perlis, Kangar, Perlis 01000, Malaysia

²Halal Products Research Institute, Universiti Putra Malaysia, UPM Serdang, Selangor 43400, Malaysia

³Department of Preclinical Sciences, Faculty of Veterinary Medicine, Universiti Putra Malaysia, UPM Serdang, Selangor 43400, Malaysia

Correspondence should be addressed to S. Mustafa, shuhaimi@biotech.upm.edu.my

Received 4 April 2011; Accepted 23 April 2011

Academic Editor: Ting Zhu

Copyright © 2012 M. E. Ali et al. This is an open access article distributed under the Creative Commons Attribution License, which permits unrestricted use, distribution, and reproduction in any medium, provided the original work is properly cited.

We visually identify pork adulteration in beef and chicken meatball preparations using 20 nm gold nanoparticles (GNPs) as colorimetric sensors. Meatball is a popular food in certain Asian and European countries. Verification of pork adulteration in meatball is necessary to meet the Halal and Kosher food standards. Twenty nm GNPs change color from pinkish-red to gray-purple, and their absorption peak at 525 nm is red-shifted by 30–50 nm in 3 mM phosphate buffer saline (PBS). Adsorption of single-stranded DNA protects the particles against salt-induced aggregation. Mixing and annealing of a 25-nucleotide (nt) single-stranded (ss) DNA probe with denatured DNA of different meatballs differentiated well between perfectly matched and mismatch hybridization at a critical annealing temperature. The probes become available in nonpork DNA containing vials due to mismatches and interact with GNPs to protect them from salt-induced aggregation. Whereas, all the pork containing vials, either in pure and mixed forms, consumed the probes totally by perfect hybridization and turned into grey, indicating aggregation. This is clearly reflected by a well-defined red-shift of the absorption peak and significantly increased absorbance in 550–800 nm regimes. This label-free low-cost assay should find applications in food analysis, genetic screening, and homology studies.

1. Introduction

Detection of selective DNA sequences is the key step in non-aggregated, genetic screening [1–3], food analysis [4–7], environmental monitoring, and forensic investigations [8]. Most of the sequence detecting assays, available at hand, rely on polymerase chain reaction (PCR) followed by electrophoretic visualization of PCR products [4–6, 8]. Although the use of PCR effectively amplifies DNA from single copy to easily detectable quantities, it is an expensive technique in the platforms of reagent and instrumental costs [3, 9]. Moreover, authentication of PCR products may further need identification of specific sequences within it by RFLP analysis [4, 6], southern blotting or sequencing [8, 9]. Therefore use of PCR is unwarranted where sample scarcity is not a concern.

The distinct surface plasmon resonance (SPR) characters of aggregated and biodiagnostics GNPs are interesting as

they can be monitored by absorption spectroscopy and also visually [3]. Researchers have long exploited these distinctive optical properties of colloidal GNPs for sensing specific oligonucleotide sequences to address a wide range of biological issues such as biodiagnostics, genetics, and food analysis [2, 3, 10–19]. However, those studies are limited to a cross-linking mechanism with synthetic probes and targets. A cross-link-based DNA detection scheme requires surface modification of GNPs to immobilize two DNA probes. The immobilized probes are further needed to be interlinked by a complementary target to realize aggregation [10, 16, 19].

Detection of nucleotide sequences by a noncross-linking method is particularly interesting [2, 3, 16]. It does not involve any modification chemistry and target hybridization is considerably fast. Li and Rothberg [2] pioneered this work by detecting selective sequences and single nucleotide mismatch in PCR amplified DNA with 13 nm-GNPs. Mismatch detection is a challenging but necessary task for the early

diagnosis of cancers and other hereditary problems [2, 3]. However, spectroscopic supports in their findings were not adequate. In our last report, we have shown 40 nm GNPs can be used for visual identification of specific sequences and mismatches in PCR-products and also in nonamplified genomic DNA. We validated our visual findings by absorption spectroscopy [3]. In the current report, we use 20 nm GNPs for visual identification of pork adulteration in meatball formulations. We demonstrate that 20nm colloidal particles produce more pronounced changes in color and absorption spectra than those of 40 nm counterparts. The absorption peak at 525 nm changes its position and appears in a new location between 555–580 nm depending on the degree of aggregation in 3 mM PBS (60 mM NaCl, pH 7.4). Stronger absorbance also remarkably appeared between 550–800 nm, making the identification more obvious. The detection limit (DL) of genomic DNA in heterogeneous mixture is also significantly reduced than that of 40-nm counterpart [3].

Meatball is a special type of restructured comminuted meat products [20, 21]. It is a favorite food in certain Asian countries such as Malaysia and Indonesia and also some European countries [20, 21]. Pork is a potential adulterant in beef and chicken meatballs due to its availability at cheaper prices. The mixing of pork or its derivatives in the Halal and Kosher foods is a serious matter as it is not permissible by the respective religious laws [20–22]. Unconscious consumption of pork may also ignite allergic reactions in certain individuals [4, 5]. Additionally, its high content of cholesterol and saturated fats are a concern for people with diabetes and cardiovascular diseases.

2. Materials and Methods

2.1. Swine Specific Probe Design. A 25 nt swine probe (567-(5′)-TAC CGC CCT CGC AGC CGT ACA TCT C-(3′)-591) is designed by comparing *Sus scrofa* cytochrome b (cytb) gene (GenBank: GU135837.1) with *Bos taurus* (cow; GenBank: EU807948.1) and *Gallus gallus* (chicken; GenBank: EU839454.1) cytb genes by ClustalW multiple sequence alignment program (<http://www.genome.jp/tools/clustalw/>). NCBI BLAST (<http://www.ncbi.nlm.nih.gov/nucleotide/blast>) analysis against nonredundant nucleotide collection confirms the probe is unique for the pig as no other species shows similarities with it. The probe is purchased from the first BASE, Selangor, Malaysia.

2.2. Synthesis of Colloidal Gold Nanoparticles. Colloidal GNPs are synthesized by the citrate method described in bibliography [23]. The resultant particles are characterized by Hitachi 7100 transmission electron microscope (TEM) (Figure 1) and PerkinElmer Lambda 25 UV-vis spectrophotometer (Figure 2). The concentration and particles number are determined according to Haiss et al. [24]. All chemicals are procured from Sigma-Aldrich, USA, in the highest analytical grades and are used without further purification. All solutions are prepared in 18.2 MΩ water (Sartorius)

immediately before use. All glass wares are cleaned with piranha solution and are oven dried prior to use.

2.3. Preparation of Meatballs and DNA Extraction. Meatballs are prepared according to Rahman et al. [21] either with pure or mixed emulsified meats of pork, beef, and chicken, along with the addition of starch, seasonings, and salts in certain ratios. All the meatballs are cooked in boiling water for 20 min prior to DNA extraction. DNA extraction is performed from 100 mg of cooked meatball of each formulations using MasterPure DNA Purification Kit (Epicenter Biotechnologies, USA) as per the manufacturer instructions. The DNA concentration is determined with a biophotometer (Eppendorf, Germany) based on triplicate readings. The purity (A_{260}/A_{280}) of all DNA samples used in all experiments is 1.95–2.0.

2.4. Detection of Single-Stranded and Double-Stranded DNA. In four separate vials, labeled as ((a)–(d); Figure 2)), 100 μ L of 1.8 nM colloidal GNPs is taken. Thirty microliters (30 μ L) of 25-mer single-stranded (ss-) and double stranded (ds-) oligoprobes of 100 nM (1st BASE, Malaysia) are added into vials (c) and (d). Volume in vial (b) is adjusted with water (18.2 MΩ). All vials, except dsDNA containing one (d), are incubated in a water bath at 50°C for 3 min to facilitate ssDNA adsorption onto GNPs [2]. Vial (d), which contains dsDNA, is incubated at 25°C to avoid temperature-induced dehybridization of the complementary strands [3]. Then 300 μ L of 10 mM PBS (0.2 M NaCl, pH 7.4) is added into each tube except vial (a) where the volume is homogenized with water. All tubes are vortexed immediately. Colloidal suspension in PBS (b) and dsDNA (d) turns into grey-purple within 3 min or immediately. However, GNPs in DI water (a) and ssDNA exposed vial (c) remain undisturbed. They retain their characteristic pinkish-red color. After 10 min, sufficient water is added into each vial to adjust the final volume to 1 mL and is characterized by transmission electron microscopy (Figure 1) and absorption spectroscopy (Figure 2). Thus the final concentration of probe, GNPs, and PBS buffer is made to 3 nM, 180 pM, and 3 mM, respectively. Stability of ssDNA-incubated colloidal particles in 3 mM PBS is studied for seven days keeping them at 4°C and is found unchanged.

2.5. Pork Identification in Beef and Chicken Meatballs. In order to detect pork contamination in processed meat products, meatballs are prepared with emulsified mixed meats of pork-beef, pork-chicken, and chicken-beef binary mixtures in 1 : 1 (w/w) ratios. Pure meatballs are formulated with pure meats of each species under identical conditions. After 20 min of cooking in boiling water, DNA extractions are performed. One hundred microliters (100 μ L) of mixed genomic DNA (300 μ gml⁻¹) is taken in vials ((b)–(d); Figure 3)). Equal portion of pure genomic DNA of pork, beef, and chicken is taken in vials (a), (e), and (f). All tubes are exposed to 30 μ L of 100 nM swine probe (25 nt; inset of Figure 3) at 95°C for 3 min to allow denaturation. All mixtures are cooled down to 50°C for 2 min to favor

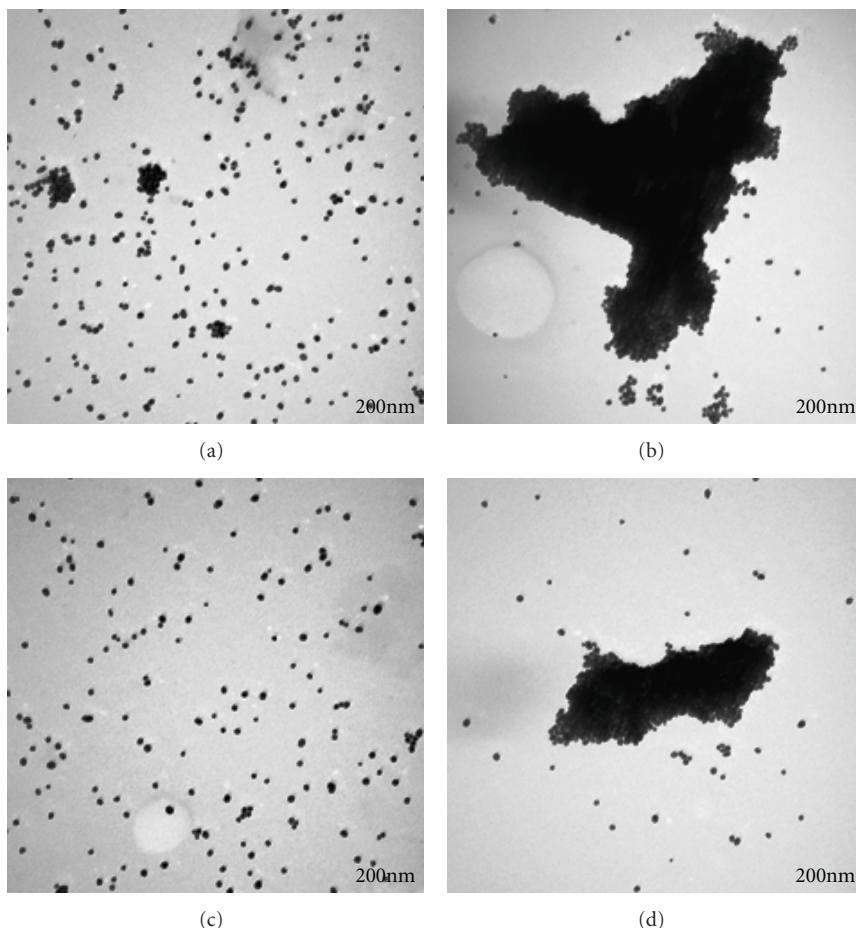


FIGURE 1: TEM images of colloidal particles before and after salt-induced aggregation. Shown are 180 pM gold colloids in DI water (a), in 3 mM PBS (b), in 3 mM PBS after 3-minute incubation in 3 nM ssDNA probe at 50°C (c), and in 3 mM PBS after the same-time incubation in equimolar 25-bp dsDNA at 25°C (d). All images are shown at a magnification of 100,000 times.

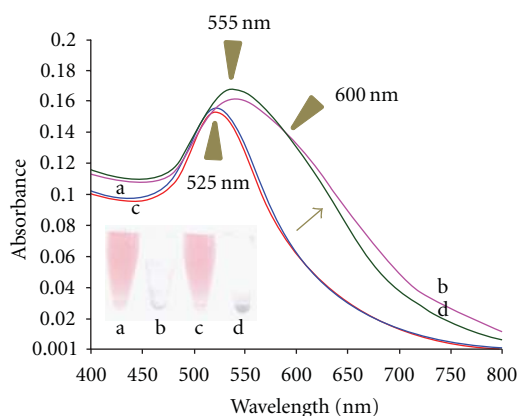


FIGURE 2: Absorption spectra of aggregated and non-aggregated GNPs. Shown are absorption spectra of 180 pM gold colloids in DI water (blue curve (a)), in 3 mM PBS (pink curve (b)), and in equimolar PBS after incubation with 3 nM ssDNA probes (red curve (c)), and with the equimolar dsDNA probes (green curve (d)). The vials in the inset shows the color photographs of the solutions in DI water (a), PBS buffer (b), PBS buffer plus ssDNA (c) and PBS buffer plus dsDNA (d).

perfectly matched annealing and mismatched nonannealing. Subsequently, 100 μL of 1.8 nM gold colloids is added to each vial and mixed for 2 min by mild shaking to allow adsorption of unhybridized probe onto GNP-surfaces. Finally, 300 μL of 10 mM PBS is added to induce aggregation of colloidal particles. All the swine DNA containing vials ((a)–(c)), either in pure (a) or mixed forms (b) and (d), immediately turn into purple-grey. However, the rest of the vials ((d)–(f)) that contain other species (chicken or beef) retain the characteristic color of colloidal particles. The final volume is adjusted to 1 mL with water and is characterized by absorption spectroscopy. Thus the final concentration of GNP, probe, genomic DNA and PBS is made to 180 pM, 3 nM, 30 $\mu\text{g mL}^{-1}$, and 3 mM.

2.6. Determination of LOD. To determine LOD, raw pork and beef are mixed in a ratio of 1:99, 3:97, 5:95, 10:90, and 15:85 (w/w). All mixtures are emulsified and meatballs are prepared. DNA is extracted from cooked meatballs of each formulation. One hundred microliters (100 μL) of mixed DNA (400 $\mu\text{g mL}^{-1}$) is taken into five separate vials ((a)–(e); Figure 4). All vials are exposed to 15 μL of 100 nM

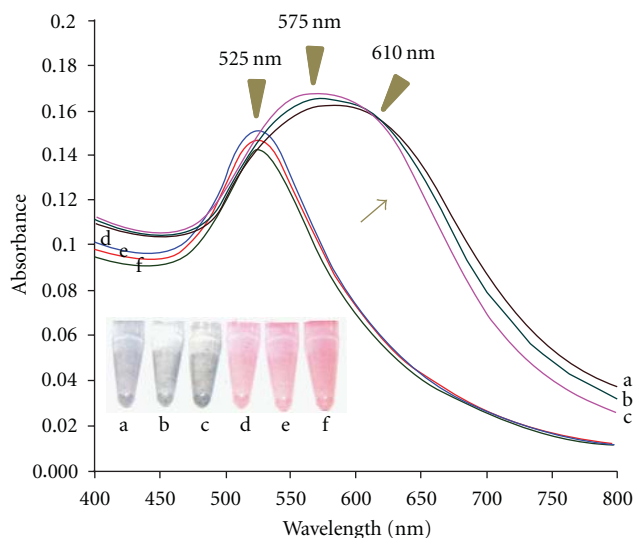


FIGURE 3: Identification of swine DNA in mixed meatballs. Vials ((a)–(f)) represent color of GNPs in genomic DNA extracted from meatballs prepared with pure pork (a), 1 : 1 (w/w) mixtures of pork-beef (b), pork-chicken (c), chicken-beef (d), pure beef (e), and pure chicken (f). The corresponding absorption spectra are labeled by respective alphabets. All vials are incubated at 95°C for 3 min and annealed at 50°C for 2 min before adding the colloidal particles and PBS. The top inset is the comparison of probe sequences with shown species. Mismatch bases are demonstrated by red.

swine probe (25 nt; Inset of Figure 3) at 95°C for 3 min and then annealed at 50°C for 2 min. After that 50 μL of 1.8 nM gold colloids is added to each vial and incubated for 2 min with mild shaking. Finally, 100 μL of 10 mM PBS is added to each vial. Vials ((a)–(c)) retain the pinkish-red color of monomeric GNPs with an increasing trend of fading. The fading of color proportionates the portion of pork in each vial. Vials (d) and (e) clearly turn into purple-grey, indicating clumping of colloidal particles. The final volume is made to 1 mL with water and is characterized by absorption spectroscopy. Thus the final concentration of probe, GNPs, mixed genomic DNA, and PBS is made to 1.5 nM, 90 pM, 40 $\mu\text{g}\text{mL}^{-1}$, and 1 mM. The concentration of swine DNA in vials ((a)–(e)) is calculated to be 0.4, 1.2, 2.0, 4.0, and 6.0 $\mu\text{g}\text{mL}^{-1}$.

3. Results and Discussion

3.1. Characterization of Gold Nanoparticles and Detection of DNA. The formation of gold nanoparticles is confirmed by TEM images (Figure 1) and UV-vis spectra (Figure 2). The size of the particles (diameter: 20 ± 5 nm) is assigned according to previously established methods [2, 3]. TEM images revealed that most of the particles are spherical in shape and homogeneously distributed throughout the bulk

solution in water (a) and in ssDNA incubated 3 mM PBS (c), clearly showing particle isolation. A minor fraction of the particles are appeared in small groups sitting side by side or one on another in water (a), showing a very low level of aggregation in DI water. This is consistent with the findings of Li and Rothberg [2]. Negative coatings of citrate ions on GNP-surfaces electrostatically repel one other, keeping them separated. ssDNA adsorbed onto GNPs surfaces by van Waals interactions and adds negative charges on GNP surfaces with the exposed phosphate groups [2, 3]. Thus the GNPs are stabilized against salt-induced aggregation when they are previously exposed to ssDNA [3].

However, the huge aggregates of GNPs become obvious after the addition of salts (3 mM PBS; b) that induces clogging of particles by screening the repulsive negative charges on particle surfaces [2]. Particles aggregation is also found in dsDNA, containing 3 mM PBS (d). However, the size of the aggregates appeared to be smaller. This is probably due to the partial protection provided by a small fraction of ssDNA which is frequently present in dsDNA solution [3].

Unlike ssDNA, dsDNA cannot protect the particles from salt-induced aggregative stresses [2, 3]. This is contrary to the conventional wisdom as both of them are highly negatively charged due to the constituent phosphate back-bone. However, when the nitrogenous bases of uncoiled ssDNA face the

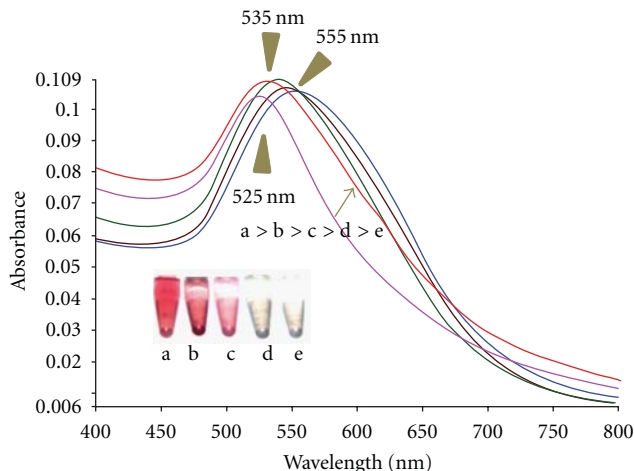


FIGURE 4: Determination of LOD for pork in ready-to-eat beef meatballs. In the inset, vials ((a)–(e)) demonstrate the color of gold nanoparticles in 1% (a), 3% (b), 5% (c), 10% (d), and 15% (e) pork DNA extracted from processed pork-beef meatballs. The corresponding absorption spectra are shown with alphabetical labels. The LOD is shown to be 10% ($4 \mu\text{g mL}^{-1}$) of swine DNA in mixed meatball preparation (vial (d) and spectrum (d)).

citrate-coated GNPs, they adsorb onto their surfaces, adding negative charges and enhancing intermolecular repulsion. On the other hand, dsDNA is highly stable and seldom uncoils to expose constituent bases [2].

Figure 2 shows the UV-vis spectra of isolated and aggregated $20 \pm 5 \text{ nm}$ -GNPs in DI water (a), and in PBS (b). The color of colloidal GNPs are very sensitive to the degree of their aggregation which can be easily induced by adding electrolytes such as salts [2]. The aggregated and non-aggregated forms of the particles can be easily distinguished by absorption spectroscopy and also visually [2, 3]. The monomeric sol exhibits pinkish red-color in DI water (a) and produces an intense surface plasmon resonance (SPR) peak at 525 nm. This is consistent with the previously reported findings [2, 3, 23, 25]. The particles aggregate immediately in 3 mM PBS (60 mM NaCl, pH 7.4) as shown in TEM image (Figure 1(b)). This is reflected by a visually detectable dramatic change in color from pinkish-red (a) to grey-purple (b).

The visually detected changes in color is strongly supported by the remarkable features in UV-vis spectrum ((spectrum (b)) of the aggregated particles. The collective plasmon peak is intensified and appears in a new position between 550 and 580 nm (Figures 2–4), depending on the degree of aggregation and concentration of GNPs. The position of this peak is more and more red-shifted with an increment of particles clumping and particle concentration. The absorption is significantly increased throughout the 550–800 nm regimes, a feature that is indicative of particles coagulation [2]. These features in absorption spectra show strong relevance with the pioneering work of Li and Rothberg [2] and Ali et al. [3]. His group detected specific sequences in PCR products by a non-cross-linking method using 13 nm GNPs. They studied the temperature

and length-dependent adsorption of ssDNA on colloidal particles and observed collective plasmon peak of aggregated 13 nm particles near 700 nm. In our last report, we did not observe any collective peak of aggregated 40 nm gold particles. However, we reported strong absorption between 600–800 nm in aggregated form. As the optical properties of GNPs are size dependent [2, 3, 12, 13], the new position of the collective plasmon peak of 20 nm particles between 550–580 nm is acceptable.

We observe that 20 nm GNPs do not change color in PBS (the inset of Figure 2(c)) if they are previously exposed to sufficient (3 nM) ssDNA at a reasonable temperature (50°C). Temperature is implicated to break down secondary structure of ssDNA and facilitates their adsorption onto GNP-surfaces by van der Waals interactions [2]. Thus the water-exposed phosphate groups of ssDNA add negative charges on particle-surfaces and protect them from salt-induced aggregation. dsDNA is highly negatively charged as phosphate groups on their back-bone are exposed to aqueous media and nitrogenous bases are shielded interior by the helical structure. Consequently, it does not adsorb onto the negatively charged GNPs [2]. Thus the particles do not get any support from dsDNA to survive in salt-induced stress in PBS. This is clearly revealed by the drastic changes in color (d) and absorption spectrum (d). This is also confirmed by relevant TEM image of Figure 1(d).

3.2. Detection of Pork Adulteration in Mixed Meatballs. In order to detect pork adulteration in beef and chicken meatballs, we design a 25 nt swine probe that bears full matching with swine cytb and 13 nt and 14 nt mismatching with the bovine and chicken cytb genes (Figure 3: inset). Thus the mismatching with bovine and chicken genes is 52% and 56%, respectively. The presence of mismatch bases has a remarkable effect on hybridization [2, 3, 9, 12, 13, 16]. Mismatches reduce melting temperature (T_m) significantly, making hybridization difficult [2, 3]. Therefore, it is highly unlikely for the probe to hybridize with bovine and chicken DNAs that contain more than 50% mismatch nucleotides at or near temperature where perfectly match hybridization is possible [2, 3]. Consequently, the probe should be available to interact with GNPs if it is annealed with bovine and chicken genes at or near its melting temperature (64°C).

We mix the probe with an excess of pure and mixed genomic DNAs of pork, beef and chicken extracted from ready to consume meatballs of respective species as shown in Figure 3. We denature the mixtures at 95°C to induce strand separation of all genomic DNAs [4–8]. Afterwards, we cool down the mixtures to $50\text{--}60^\circ\text{C}$ to allow complementary base-pairing between the strands and the probe. Previous studies demonstrated shorter DNA hybridizes before the longer counterparts due to steric reasons [2]. Thus the limited probe should be completely engulfed by the excess genomic DNA if it bears complementary targets within it. However, the probe does not hybridize with mismatch bearing targets if they are not forced to do so by the excessive reduction of annealing temperature.

The inset of Figure 3 clearly shows that the probe is consumed completely by the pork DNA in pure (vial (a)) or

mixed forms (vials (b) and (c)). Thus the colloidal particles in all pork containing vials ((a)–(c)) experience clogging upon the addition of salts as they are not protected by the ssDNA probe. This is clearly depicted by the dramatic change of color from pinkish-red to grey purple. The UV-vis spectra demonstrate a huge red-shift of ~ 100 nm and appearance of a collective plasmon peak at 575 nm, confirming the visually determined result. However, probe is not engulfed at all by the huge mismatch ($>50\%$) containing beef or chicken DNA either in pure (vials (e) & (f)) or mixed formulation (vial (d)). Thus the probe is available in vials ((d)–(f)) to adsorb onto GNPs surfaces to provide them withstanding strength in salt solution. Consequently GNPs of these vials do not undergo aggregation upon the addition of equimolar PBS. This is clearly revealed by their retention of characteristic pinkish-red color and plasmon peak of isolated colloidal particles at 525 nm.

3.3. Determination of LOD. The absorption spectra and visually detected color of GNPs in various percentages of pork containing beef meatballs are shown in Figure 4.

It is very clear from visually observed results as well as spectroscopic data that 1% pork containing vial (a) retains almost 100% original color of colloidal particles (pink curve: spectrum (a)). However, original pinkish-red color of GNPs in 3–5% pork containing vials ((b) and (c)) considerably disappeared, reflecting partial aggregation. This is confirmed by the appearance of collective plasmon peak near 535 nm and considerably stronger absorption between 550 and 650 nm ((red curve: spectrum (b) and green curve: spectrum (c)). On the other hand, 10% and 15% pork containing vials ((d) and (e)) change color from pinkish-red to purple-grey simulating aggregation. Absorption spectra of vials (d) and (e) display the collective surface plasmon features of 20 nm aggregated particles between 550 and 700 nm with a collective plasmon peak near 555 nm. Concentration of swine DNA in 10% pork containing vial is $4 \mu\text{g mL}^{-1}$. Thus the determined LOD is $4 \mu\text{g mL}^{-1}$ swine DNA in processed beef meatballs. It is observed that some of the particles (~ 3 – 5%) retain their colors in vials (d) and (e) that contain 10% and 15% swine DNA. These are most likely the unconsumed probe-bound particles that withstand the salinity stresses.

3.4. Efficacy and Limitation of the Current Assay. The current assay directly determines swine-specific sequences in a population of nonamplified mixed genomic DNA. The mixed population of genomic DNA is obtained from meatballs, prepared with the emulsified meats of chicken, beef, and pork. The method is capable of detecting target sequences just by visually observed color change of GNPs. The visually determined results are sufficient to make a concrete decision. However, it can be further authenticated by a relatively inexpensive and easily available absorption spectroscopy. This eliminates any sort of color blindness errors that may arise from visual findings. Sensitivity of the assay is also improved as revealed by a low LOD ($4 \mu\text{g mL}^{-1}$).

Both the color and absorption spectra of 20 nm GNPs are more remarkable than the earlier report [3], making

them a more suitable candidate for the analysis of targets in processed meat products. In earlier report, we have shown absorption peak of 40 nm colloidal particles at 530 nm fall down commensurating the degree of aggregation [3]. However, the current study has shown the absorption peak of 20 nm particles change its position and appears in a new position proportioning particle clumping. Absorption between 550–800 nm regimes is also significantly increased following aggregation. Thus a well-defined change in the peak position of aggregated and non-aggregated particles can be easily detected avoiding any ambiguity. These features probably make 20 nm counterparts more sensitive than 40 nm particles.

The LOD of the assay is higher than that of the real-time and conventional PCR [5–7]. However, PCR-based methods need comparatively longer targets which are reported to break down during the chemical and physical stresses of food processing, causing template crisis in PCR assay [9]. On the other hand, the present assay uses DNA target (25 nt) that is comparable with the size of a typical PCR-primer [5–7]. As shorter targets are more stable than the longer one [7], the method can be applied to analyze highly degraded samples where PCR may lose its candidacy. The probe design is also much simpler than that of a PCR assay. Moreover, PCR-electrophoresis is a clumsy technique and sometimes needs self-authentication by RFLP-analysis [4], sequencing, or blotting [8]. The LOD of the assay can be decreased by using increased amount of DNA mixtures to ensure sufficient targets for the probe. Using increased amount of targets is not problematic in food analysis because here sample scarcity is not a concern.

The presence of single stranded nucleic acids (DNA or RNA) interferes with target detection by sticking to GNPs and interfering particle aggregation. However, by using appropriate purification technique [26], the single-stranded nucleic acid can be easily removed from the degraded samples.

The method cannot provide quantitative information of the target DNA. TaqMan fluorogenic probe can detect, quantify, and amplify specific sequences by real-time PCR without the need of electrophoresis and blot analysis [7]. However, the TaqMan probe, real-time PCR, and the master-mix used in real-time PCR are highly expensive and ordinary laboratories cannot afford them. On the other hand, UV-vis spectroscopy is available in most laboratories and can authenticate the visually identified results of colloidal gold.

4. Conclusion

A rapid (less than 10 min), reliable, and cheap method for the selective detection of target DNA sequences in processed meat products is developed. It does not need any instrument or surface modification chemistry and directly detects target DNA in nonamplified mixed genomic DNA. The procedure is very simple and relies on the color change of 20-nm GNPs following salt addition. The visual finding is solid and can be further confirmed by an inexpensive, available, and reliable technique, absorption spectroscopy which incurs

only the instrumental cost and reusable cuvette. The use of absorption spectroscopy increases sensitivity and eliminates any sort of color-blindness error or ambiguity in visual detection by producing well-defined bands of aggregated and non-aggregated colloidal particles. The assay needs a shorter probe whose design is simpler than PCR primers. The method is applicable to analyze extensively degraded sample which may not be possible by PCR which require longer targets.

Acknowledgments

This paper is supported by Grants “RUGS No. 9031” to Professor. Y. B. Che Man and “MOSTI No. 05-01-35-SF-1030” to Prof. U. Hashim and “The University of Malaysia, Perlis (UniMAP) Graduate Assistantship” to M. E. Ali.

References

- [1] J. Rees, “Complex disease and the new clinical sciences,” *Science*, vol. 296, no. 5568, pp. 698–701, 2002.
- [2] H. Li and L. J. Rothberg, “Label-free colorimetric detection of specific sequences in genomic DNA amplified by the polymerase chain reaction,” *Journal of the American Chemical Society*, vol. 126, no. 35, pp. 10958–10961, 2004.
- [3] M. E. Ali, U. Hashim, S. Mustafa et al., “Nanoparticle sensor for label free detection of swine DNA in mixed biological samples,” *Nanotechnology*, vol. 22, no. 19, Article ID 195503, 2011.
- [4] Y. B. Che Man, A. A. Aida, A. R. Raha, and R. Son, “Identification of pork derivatives in food products by species-specific polymerase chain reaction (PCR) for Halal verification,” *Food Control*, vol. 18, no. 7, pp. 885–889, 2007.
- [5] N. Z. Ballin, F. K. Vogensen, and A. H. Karlsson, “Species determination—can we detect and quantify meat adulteration?” *Meat Science*, vol. 83, no. 2, pp. 165–174, 2009.
- [6] C. Murugaiah, Z. M. Noor, M. Mastakim, L. M. Bilung, J. Selamat, and S. Radu, “Meat species identification and Halal authentication analysis using mitochondrial DNA,” *Meat Science*, vol. 83, no. 1, pp. 57–61, 2009.
- [7] M. Rojas, I. González, M. A. Pavón et al., “Novel TaqMan real-time polymerase chain reaction assay for verifying the authenticity of meat and commercial meat products from game birds,” *Food Additives and Contaminants*, vol. 27, no. 6, pp. 749–763, 2010.
- [8] J. M. Butler, *Forensic DNA Typing-Biology, Technology and Genetics of STR Markers*, Elsevier, New York, NY, USA, 2nd edition, 2005.
- [9] M. E. Ali, U. Hashim, S. Mustafa et al., “Nanobiosensor for detection and quantification of swine specific DNA sequences in degraded mixed meats,” vol. 2011, Article ID 781098, *Journal of Nanomaterials*. In press.
- [10] C. A. Mirkin, R. L. Letsinger, R. C. Mucic, and J. J. Storhoff, “A DNA-based method for rationally assembling nanoparticles into macroscopic materials,” *Nature*, vol. 382, no. 6592, pp. 607–609, 1996.
- [11] R. Elghanian, J. J. Storhoff, R. C. Mucic, R. L. Letsinger, and C. A. Mirkin, “Selective colorimetric detection of polynucleotides based on the distance-dependent optical properties of gold nanoparticles,” *Science*, vol. 277, no. 5329, pp. 1078–1081, 1997.
- [12] B. Dubertret, M. Calame, and A. J. Libchaber, “Single-mismatch detection using gold-quenched fluorescent oligonucleotides,” *Nature Biotechnology*, vol. 19, no. 4, pp. 365–370, 2001.
- [13] D. J. Maxwell, J. R. Taylor, and S. Nie, “Self-assembled nanoparticle probes for recognition and detection of biomolecules,” *Journal of the American Chemical Society*, vol. 124, no. 32, pp. 9606–9612, 2002.
- [14] Y. W. C. Cao, R. Jin, and C. A. Mirkin, “Nanoparticles with Raman spectroscopic fingerprints for DNA and RNA detection,” *Science*, vol. 297, no. 5586, pp. 1536–1540, 2002.
- [15] B. S. Gaylord, A. J. Heeger, and G. C. Bazan, “DNA hybridization detection with water-soluble conjugated polymers and chromophore-labeled single-stranded DNA,” *Journal of the American Chemical Society*, vol. 125, no. 4, pp. 896–900, 2003.
- [16] K. Sato, K. Hosokawa, and M. Maeda, “Rapid aggregation of gold nanoparticles induced by non-cross-linking DNA hybridization,” *Journal of the American Chemical Society*, vol. 125, no. 27, pp. 8102–8103, 2003.
- [17] C. Jung, H. Y. Mun, T. Li, and H. G. Park, “A simple gold nanoparticle-mediated immobilization method to fabricate highly homogeneous DNA microarrays having higher capacities than those prepared by using conventional techniques,” *Nanotechnology*, vol. 20, no. 3, Article ID 035607, 2009.
- [18] S. Oaew, N. Karoonuthaisiri, and W. Surareungchai, “Sensitivity enhancement in DNA hybridization assay using gold nanoparticle-labeled two reporting probes,” *Biosensors and Bioelectronics*, vol. 25, no. 2, pp. 435–441, 2009.
- [19] D. T. Nguyen, D.-J. Kim, and K.-S. Kim, “Controlled synthesis and biomolecular probe application of gold nanoparticles,” *Micron*, vol. 42, pp. 207–227, 2011.
- [20] H. Purnomo and D. Rahardiyan, “Indonesian traditional meatball,” *International Food Research Journal*, vol. 15, no. 2, pp. 101–108, 2008.
- [21] A. Rahman, Sismindary, Y. Erwanto, and Y. B. Che Man, “Analysis of pork adulteration in beef meatball using Fourier transform infrared (FTIR) spectroscopy,” *Meat Science*, vol. 88, no. 1, pp. 91–95, 2011.
- [22] J. M. Regenstein, M. M. Chaudry, and C. E. Regenstein, “The kosher and halal food laws,” *Comprehensive Reviews in Food Science and Food Safety*, vol. 2, pp. 111–127, 2003.
- [23] K. C. Grabar, R. G. Freeman, M. B. Hommer, and M. J. Natan, “Preparation and characterization of Au colloid monolayers,” *Analytical Chemistry*, vol. 67, no. 4, pp. 735–743, 1995.
- [24] W. Haiss, N. T. K. Thanh, J. Aveyard, and D. G. Fernig, “Determination of size and concentration of gold nanoparticles from UV-vis spectra,” *Analytical Chemistry*, vol. 79, no. 11, pp. 4215–4224, 2007.
- [25] M. O. Nutt, K. N. Heck, P. Alvarez, and M. S. Wong, “Improved Pd-on-Au bimetallic nanoparticle catalysts for aqueous-phase trichloroethene hydrodechlorination,” *Applied Catalysis*, vol. 69, no. 1-2, pp. 115–125, 2006.
- [26] J. M. Egly and J. L. Plassat, “Separation of single-stranded from double-stranded nucleic acids using acriflavin-agarose chromatography,” *Journal of Chromatography*, vol. 243, no. 2, pp. 301–306, 1982.

Research Article

Fluorescent Properties of ZnO Nanostructures Fabricated by Hydrothermal Method

Zhiwei Dong,^{1,2} Bing Han,³ Shixiong Qian,² and Deying Chen¹

¹National Key Laboratory of Tunable Lasers, Institute of Optical-Electronics, Harbin Institute of Technology, Harbin 150001, China

²State Key Laboratory of Applied Surface Physics and Department of Physics, Fudan University, Shanghai 200433, China

³College of Physics, Jilin University, Changchun 130001, China

Correspondence should be addressed to Zhiwei Dong, dong19809@163.com

Received 29 March 2011; Accepted 23 April 2011

Academic Editor: Ting Zhu

Copyright © 2012 Zhiwei Dong et al. This is an open access article distributed under the Creative Commons Attribution License, which permits unrestricted use, distribution, and reproduction in any medium, provided the original work is properly cited.

ZnO nanorods with mean diameter 200 nm on different substrates were fabricated by hydrothermal method. Fluorescent properties of fabricated ZnO nanorods were researched by both linear and nonlinear excitation using femtosecond lasers. The damage threshold of productions on Si substrate irradiated under intense femtosecond pulses was found much higher than that on Zn plate. Raman spectrum was also applied to investigate relative optical properties. The A_{1L} optical mode was found to be important to the fluorescent properties of ZnO materials.

1. Introduction

ZnO is a kind of II-VI compound wide band gap semiconductor with a direct band gap of 3.37 eV and a large exciton binding energy about 60 meV at room temperature, which makes it a potential candidate for the room temperature ultraviolet (UV) laser diodes [1, 2]. Researches on the fabrication of ZnO materials show that different kinds of nanostructures can be got through controlling fabrication methods or conditions [3–5]. Among the fabrication methods, hydrothermal has been found to be economical and flexible to realize various kinds of nanostructures such as nanorods and nanoflowers [6–9]. Most of the researches about hydrothermal fabrication were focused on the relationship between fabrication conditions and the configuration of the productions [10–13]. Special investigations on the effects of fabrication conditions on the optical properties of ZnO nanostructures are meaningful. But as far as we know, these researches are still few.

Besides, owing to the development of laser technology, the emergence of ultrafast laser, especially the femtosecond (fs) laser source with low repetition rate, makes it possible to get extremely intense field above TW/cm^2 which ensures us to explore the interaction between condensed matters and

intense field. Recently, researches on the nonlinear excitation of ZnO with intense laser pulses have been done, and the nonlinear properties, especially the basic mechanisms of multiphoton absorption-induced fluorescent emission in ZnO, are proven to be meaningful [14–20]. This calls for the ZnO materials with high quality that is stable under the intense field of ultrafast pulses [21]. However, most of the ZnO materials used in these experiments are fabricated by molecular beam epitaxy (MBE), metal-organic chemical vapor deposition (MOCVD), or magnetron sputtering [22–25]. Special researches on the fluorescent properties of hydrothermal ZnO are quite few.

In this paper, we fabricated ZnO nanorods with mean diameter 200 nm on different substrates through hydrothermal at 90°C. The fabrication conditions including the concentrations of reactants, pH value, and substrate properties on the fluorescent properties of the productions were discussed by applying Raman spectra and fluorescent spectra under linear and nonlinear excitation conditions.

2. Experimental

The details of the fabrication of ZnO materials are as follows. The Si or Zn plate substrates were first precleaned by

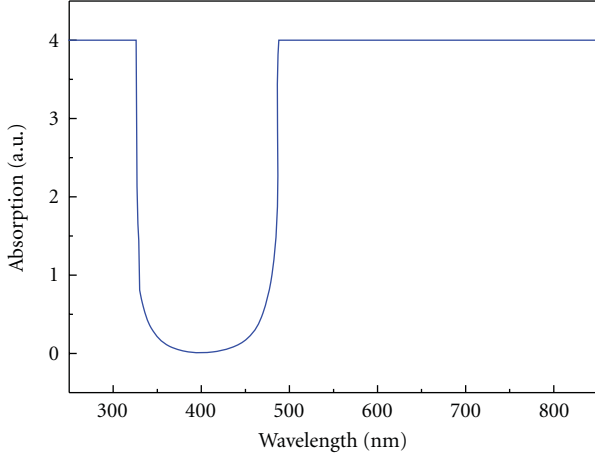
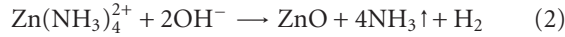
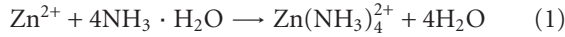


FIGURE 1: Absorption spectrum of the blue glass used in the measurement of fluorescent spectra under nonlinear excitation.

ultrasonic. Then, the reactant solution with zinc chloride solution (0.1 M) and ammonia used to adjust the PH value were mixed, round, and poured into a Teflon vessel. After the substrates were put into it, the vessel was heated to 90°C for 4 hours and then cooled down naturally; the products were washed with deionized water for several times and dried. Scanning electron microscopy (SEM) was introduced to characterize the products. The main reactions occurred in the vessel can be expressed as follows [9]:



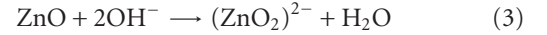
The fluorescent properties of fabricated nanostructures were recorded when the productions were excited by Xe lamp at 327 nm. The nonlinear excitation laser source used in this experiment was a Ti:sapphire laser (Spectra-Physics, Spitfire) operating at repetition rate of 1 kHz with output pulses centred around 800 nm and full width at half maximum of 150 fs. The nonlinear fluorescent spectra were recorded by a spectrometer with a blue glass placed in front to filter the excitation laser. The absorption spectrum of the blue glass is shown in Figure 1. The Raman spectra were recorded by a Raman spectrometer with an argon laser at 514.5 nm as the excitation source.

3. Results and Discussion

Figure 2(a) illustrates the products on the Zn plate when the content of the zinc chloride is 0.1 M and PH value is 11 in the reactant solution. The productions show nanorods with the mean diameter about 200 nm from the SEM image. And they form balls with the size in micrometer. We investigated the effects of reactant solution by changing the content of zinc chloride or PH value. When the content of the zinc chloride decreased, the amount of the products decreased accordingly. Figure 2(b) shows the SEM image of the products when the content of the zinc chloride is 0.07 M. No nanostructures

were found on the substrate. According to (1) and (2), when the concentration of zinc chloride is low, the reactions move to the left which means that ZnO cannot be formed in this condition.

The optical properties of the productions were first researched by fluorescent spectra under linear excitation. Figure 3 is the fluorescent spectra of fabricated nanostructures on Zn substrate with different PH values of the reactant solution excited at 327 nm. The intense peak at near the ultraviolet region corresponds to the band-edge emission of ZnO which indicates that the nanostructures produced were ZnO. Usually, there is a broad peak at around 550 nm in the fluorescent spectra of the hydrothermal fabricated ZnO material which is caused by defects induced in the fabrication process [26–29]. Compared with the UV emission, this peak is weak in the fluorescent spectra especially when the PH value of the reactant solution is 11 as shown in the blue line in Figure 3, implying good optical properties of the fabricated ZnO under this condition. When the PH value of the solution increased further, too much OH^- in the reactant solution may cause defects in the ZnO which can be expressed as follows:



The fluorescent spectrum of the products fabricated under PH value of 12 on Zn plate is shown in the red dashed line in Figure 3. The broad peak around 550 nm enhances evidently which confirms the supposition above. The remaining $(\text{ZnO}_2)^{2-}$ due to the incomplete cleaning step may also be another origin of this broad peak in the fluorescent spectra.

The fluorescent properties under nonlinear excitation conditions were investigated applying femtosecond pulses. The productions on Zn plate were found unstable under the intense excitation field, and no fluorescent spectrum was recorded under our experimental conditions. Figure 4 shows the fluorescent spectrum of the productions on Si plate irradiated under 800 nm femtosecond pulses. The peak at 400 nm was found moving together with the tuning of the excitation laser, and it kept locating at just half of the wavelength of the excitation laser. It was attributed to the second harmonic signal (SHG) of the excitation laser. The peak at the blue side of the SHG is the band-edge emission of ZnO which is mainly caused by the exciton-exciton collision or the recombination of the electron-hole plasma (EHP) [21]. This peak increased quite prominently compared with SHG, and the spectral width of this peak decreased to only 2 nm when the excitation intensity reached 0.2 TW/cm², indicating that stimulated emission emerged under this excitation condition. This shows that we fabricated ZnO nanorods through hydrothermal with high quality that can realize stimulated emissions at room temperature under intense nonlinear excitation. The experimental results show that the damage threshold of ZnO nanorods irradiated under intense femtosecond pulses fabricated on Si substrate is much higher than that on Zn plate which is considered relative to the surface properties of the substrates for the surface

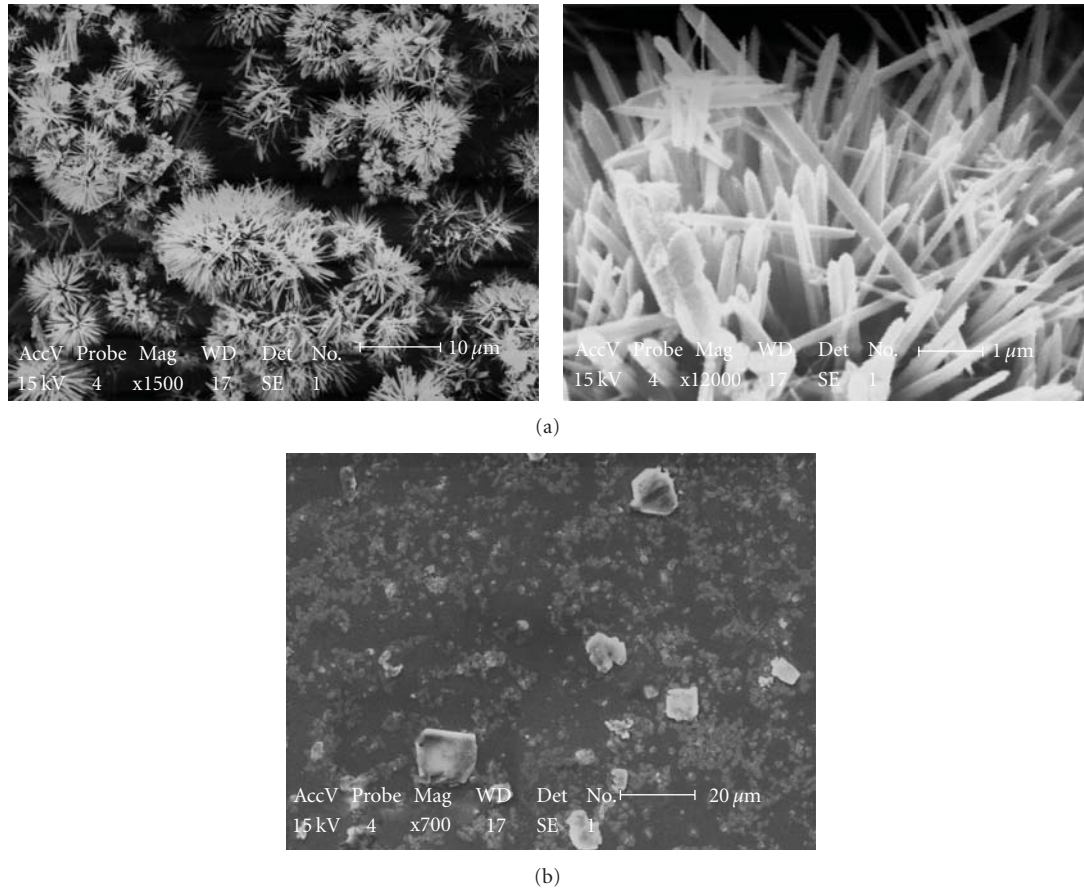


FIGURE 2: (a) SEM images of ZnO nanostructures on Zn substrate with different scales when the Zn^{2+} content is 0.1 M. (b) SEM image of fabricated ZnO on Zn substrate fabricated by hydrothermal method with low Zn^{2+} content 0.07 M.

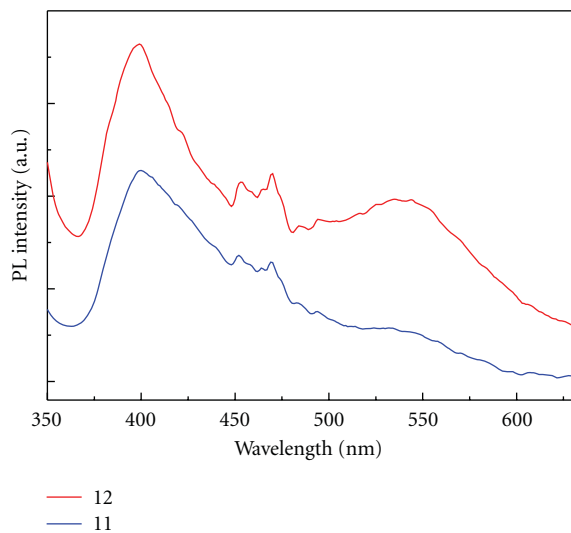


FIGURE 3: Fluorescent spectra of ZnO nanostructures fabricated with different PH values on Zn substrate excited at 327 nm (the red curve is moved upwards).

of the Si plate was much glazed than that of the Zn plate used in the experiment and the substrate softened when Zn is

heated above 90°C , because both Si and ZnO are cubic crystal structure, however, Zn is hexagonal crystal structure. The difference in their crystal structures is another reason that Si substrate benefits the formation of ZnO with high quality.

To further investigate the optical properties of ZnO on different substrates, we measured the Raman spectra of the ZnO nanostructures as shown in Figure 5 with the red and blue line responses to the result of products on Si and Zn plate, respectively. There are several Raman peaks in the region of $50\text{--}1400\text{ cm}^{-1}$. The obvious sharp peaks at 100 and 438 cm^{-1} correspond to E_2 mode which confirm the formation of ZnO, the wide peak around 1140 cm^{-1} is A_1 mode, while the relative weak peak at 331 and 378 cm^{-1} corresponds to A_1 and A_{1T} mode, respectively [30]. Compared with that on Zn substrate, the A_{1L} mode which locates at 576 cm^{-1} only emerges in the case of Si as substrate. Considering the results under nonlinear excitation, we regard that the A_{1L} optical mode is important to the fluorescent properties of ZnO materials. Compared with transverse optical modes, the coupling between longitudinal optical modes and electromagnetic field is more efficient especially for low-order optical modes [31]. This is why A_{1L} optical mode is important to the fluorescent properties of productions. The experimental results show that Si substrate benefits the formation of A_{1L} optical mode compared with Zn plate.

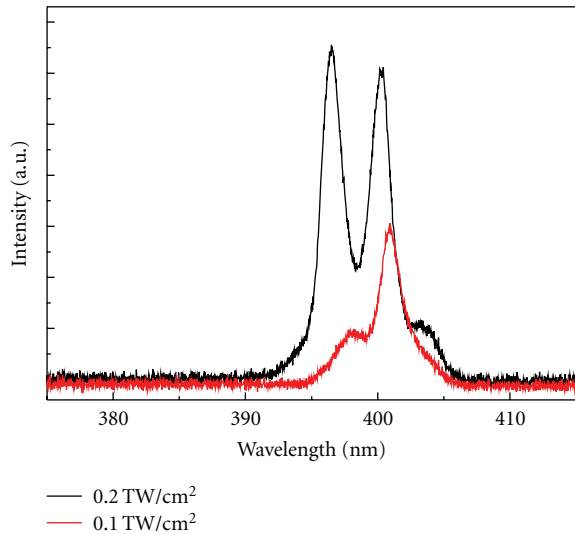


FIGURE 4: Fluorescent spectrum of fabricated ZnO nanostructure on Si substrate excited at 800 nm applying femtosecond pulses under different excitation intensities.

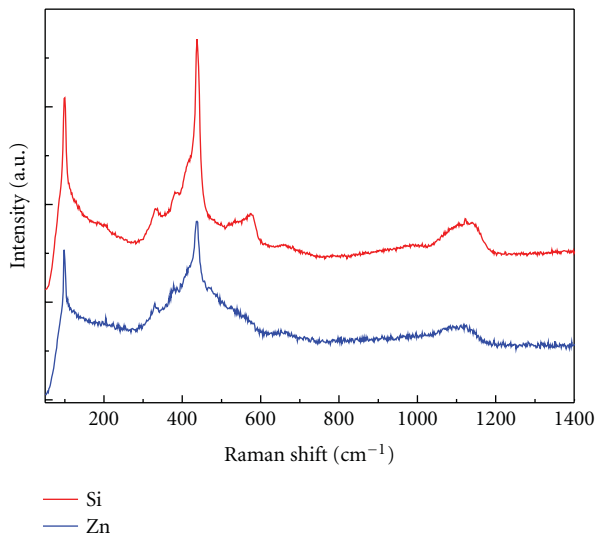


FIGURE 5: Raman spectra of fabricated ZnO nanostructures on Si and Zn substrates (the red curve is moved upwards).

4. Conclusions

In summary, ZnO nanorods have been fabricated by hydrothermal method on Zn and Si substrates. The effects of fabrication conditions including the concentrations of reactants, PH value, and substrates on the fluorescent properties of fabricated ZnO material have been researched. The optimized fabrication conditions were found, and stimulated emissions in the hydrothermal fabricated ZnO nanorods were realized at room temperature under intense nonlinear excitation. The A_{1L} optical mode was found important to the fluorescent properties of ZnO materials by analyzing the Raman spectra of the productions on Si and Zn substrates.

Acknowledgments

The authors gratefully acknowledge the financial support from National Natural Science Foundation of China (no. 11004042), the Research Fund for the Doctoral Program of Higher Education (RFDP20102302120022), China Postdoctoral Science Foundation (20090451006), Development Program for Outstanding Young Teachers in Harbin Institute of Technology (HITQJNS.2009.003), and relative foundation from Heilongjiang province and Harbin city (2011RFQXG003).

References

- [1] M. H. Huang, S. Mao, H. Feick et al., "Room-temperature ultraviolet nanowire nanolasers," *Science*, vol. 292, no. 5523, pp. 1897–1899, 2001.
- [2] P. Yu, Z. K. Tang, G. K. Wong et al., "Room-temperature gain spectra and lasing in microcrystalline ZnO thin films," *Journal of Crystal Growth*, vol. 184–185, pp. 601–604, 1998.
- [3] L. Vayssieres, "Growth of arrayed nanorods and nanowires of ZnO from aqueous solutions," *Advanced Materials*, vol. 15, no. 5, pp. 464–466, 2003.
- [4] A. Wei, C. X. Xu, X. W. Sun, W. Huang, and G. Q. Lo, "Field emission from hydrothermally grown ZnO nanoinjectors," *Journal of Display Technology*, vol. 4, no. 1, pp. 9–12, 2008.
- [5] J. M. Szarko, J. K. Song, C. W. Blackledge et al., "Optical injection probing of single ZnO tetrapod lasers," *Chemical Physics Letters*, vol. 404, no. 1–3, pp. 171–176, 2005.
- [6] H. Zhang, D. Yang, Y. J. Ji, X. Ma, J. Xu, and D. Que, "Low temperature synthesis of flowerlike ZnO nanostructures by cetyltrimethylammonium bromide-assisted hydrothermal process," *Journal of Physical Chemistry B*, vol. 108, no. 13, pp. 3955–3958, 2004.
- [7] A. Wei, X. W. Sun, C. X. Xu, Z. L. Dong, M. B. Yu, and W. Huang, "Stable field emission from hydrothermally grown ZnO nanotubes," *Applied Physics Letters*, vol. 88, no. 21, Article ID 213102, 2006.
- [8] C. X. Xu, A. Wei, X. W. Sun, and Z. L. Dong, "Aligned ZnO nanorods synthesized by a simple hydrothermal reaction," *Journal of Physics D*, vol. 39, no. 8, pp. 1690–1693, 2006.
- [9] A. Wei, X. W. Sun, C. X. Xu et al., "Growth mechanism of tubular ZnO formed in aqueous solution," *Nanotechnology*, vol. 17, no. 6, pp. 1740–1744, 2006.
- [10] H. D. Li, S. F. Yu, S. P. Lau et al., "High-temperature lasing characteristics of ZnO epilayers," *Advanced Materials*, vol. 18, no. 6, pp. 771–774, 2006.
- [11] H. Cao, J. Y. Wu, H. C. Ong, J. Y. Dai, and R. P. H. Chang, "Second harmonic generation in laser ablated zinc oxide thin films," *Applied Physics Letters*, vol. 73, no. 5, pp. 572–574, 1998.
- [12] G. I. Petrov, V. Shcheslavskiy, V. V. Yakovlev, I. Ozerov, E. Chelnokov, and W. Marine, "Efficient third-harmonic generation in a thin nanocrystalline film of ZnO," *Applied Physics Letters*, vol. 83, no. 19, pp. 3993–3995, 2003.
- [13] X. Zhang, H. Fang, S. Tang, and W. Ji, "Determination of two-photon-generated free-carrier lifetime in semiconductors by a single-beam Z-scan technique," *Applied Physics B*, vol. 65, no. 4–5, pp. 549–554, 1997.
- [14] E. V. Chelnokov, N. Bituryn, I. Ozerov, and W. Marine, "Two-photon pumped random laser in nanocrystalline ZnO," *Applied Physics Letters*, vol. 89, no. 17, Article ID 171119, 2006.

- [15] Y. F. Zhang, R. E. Russo, and S. S. Mao, "Femtosecond laser assisted growth of ZnO nanowires," *Applied Physics Letters*, vol. 87, no. 13, Article ID 133115, 3 pages, 2005.
- [16] D. Li, Y. H. Leung, A. B. Djurišić et al., "Different origins of visible luminescence in ZnO nanostructures fabricated by the chemical and evaporation methods," *Applied Physics Letters*, vol. 85, no. 9, pp. 1601–1603, 2004.
- [17] W. Z. Xu, Z. Z. Ye, D. W. Ma et al., "Quasi-aligned ZnO nanotubes grown on Si substrates," *Applied Physics Letters*, vol. 87, no. 9, Article ID 093110, 3 pages, 2005.
- [18] I. H. Lee, K. J. Yee, K. G. Lee, E. Oh, D. S. Kim, and Y. S. Lim, "Coherent optical phonon mode oscillations in wurtzite ZnO excited by femtosecond pulses," *Journal of Applied Physics*, vol. 93, no. 8, pp. 4939–4941, 2003.
- [19] R. Prasanth, L. K. Van Vugt, D. A. Vanmaekelbergh, and H. C. Gerritsen, "Resonance enhancement of optical second harmonic generation in a ZnO nanowire," *Applied Physics Letters*, vol. 88, no. 18, Article ID 181501, 2006.
- [20] C. F. Zhang, Z. W. Dong, G. J. You et al., "Observation of two-photon-induced photoluminescence in ZnO microtubes," *Applied Physics Letters*, vol. 87, no. 5, Article ID 051920, 2005.
- [21] Z. W. Dong, C. F. Zhang, K. J. Liu, Y. L. Yan, H. Deng, and S. X. Qian, "Multi-photon excitation in ZnO materials," *Frontiers of Physics in China*, vol. 3, no. 2, pp. 181–190, 2008.
- [22] P. Fons, K. Iwata, S. Niki, A. Yamada, and K. Matsubara, "Growth of high-quality epitaxial ZnO films on α -Al₂O₃," *Journal of Crystal Growth*, vol. 201, pp. 627–632, 1999.
- [23] J. H. Lin, Y. J. Chen, H. Y. Lin, and W. F. Hsieh, "Two-photon resonance assisted huge nonlinear refraction and absorption in ZnO thin films," *Journal of Applied Physics*, vol. 97, no. 3, Article ID 033526, 2005.
- [24] Y. Liu, C. R. Gorla, S. Liang et al., "Ultraviolet detectors based on epitaxial ZnO films grown by MOCVD," *Journal of Electronic Materials*, vol. 29, no. 1, pp. 69–74, 2000.
- [25] K. K. Kim, J. H. Song, H. J. Jung, W. K. Choi, S. J. Park, and J. H. Song, "The grain size effects on the photoluminescence of ZnO/ α -Al₂O₃ grown by radio-frequency magnetron sputtering," *Journal of Applied Physics*, vol. 87, no. 7, pp. 3573–3575, 2000.
- [26] K. K. Kim, J. H. Song, H. J. Jung et al., "Photoluminescence and heteroepitaxy of ZnO on sapphire substrate (0001) grown by rf magnetron sputtering," *Journal of Vacuum Science and Technology A*, vol. 18, no. 6, pp. 2864–2868, 2000.
- [27] J. B. Liang, J. W. Liu, Q. Xie, S. Bai, W. Yu, and Y. Qian, "Hydrothermal growth and optical properties of doughnut-shaped ZnO microparticles," *Journal of Physical Chemistry B*, vol. 109, no. 19, pp. 9463–9467, 2005.
- [28] J. J. Wu, H. I. Wen, C. H. Tseng, and S. C. Liu, "Well-aligned ZnO nanorods via hydrogen treatment of ZnO films," *Advanced Functional Materials*, vol. 14, no. 8, pp. 806–810, 2004.
- [29] F. S. Wen, W. L. Li, J. H. Moon, and J. H. Kim, "Hydrothermal synthesis of ZnO: Zn with green emission at low temperature with reduction process," *Solid State Communications*, vol. 135, no. 1–2, pp. 34–37, 2005.
- [30] R. P. Wang, G. Xu, and P. Jin, "Size dependence of electron-phonon coupling in ZnO nanowires," *Physical Review B*, vol. 69, no. 11, Article ID 113303, 2004.
- [31] T. L. Phan, R. Vincent, D. Cherns, N. H. Dan, and S. C. Yu, "Enhancement of multiple-phonon resonant Raman scattering in Co-doped ZnO nanorods," *Applied Physics Letters*, vol. 93, no. 8, Article ID 082110, 2008.

Research Article

Study of Structural and Optical Properties of Zinc Oxide Rods Grown on Glasses by Chemical Spray Pyrolysis

Erdal Sonmez,¹ Serdar Aydin,¹ Mehmet Yilmaz,¹ Mustafa Tolga Yurtcan,¹ Tevhit Karacali,² and Mehmet Ertugrul²

¹Physics Department, Education Faculty, University of Atatürk, 25240 Erzurum, Turkey

²Electrical and Electronics Engineering Department, University of Atatürk, 25240 Erzurum, Turkey

Correspondence should be addressed to Erdal Sonmez, esonmez@atauni.edu.tr

Received 29 March 2011; Accepted 11 April 2011

Academic Editor: Ting Zhu

Copyright © 2012 Erdal Sonmez et al. This is an open access article distributed under the Creative Commons Attribution License, which permits unrestricted use, distribution, and reproduction in any medium, provided the original work is properly cited.

We have investigated morphological and optical properties of zinc oxide rods. Highly structured ZnO layers comprising with well-shaped hexagonal rods were prepared by spray pyrolysis deposition of zinc chloride aqueous solutions at $\sim 550^\circ\text{C}$. The rods were characterized by X-ray diffraction, scanning electron microscopy, atomic force microscopy, photoluminescence, and ultraviolet and visible absorption spectroscopy measurements. The deposition of the 0.1 mol/L solution at $\sim 550^\circ\text{C}$ resulted in crystals with a diameter of 400–1000 nm and length of 500–2000 nm. Sharp near-band edge emission peaks, centered at 3844 and 3680 Å, dominated the PL spectra of ZnO at 300 K and 6.2 K, respectively. In addition to this, absorption coefficient was determined by absorption measurement. X-ray diffraction, scanning electron microscopy and atomic force microscopy, results suggest that ZnO rods, prepared by spray pyrolysis, have high crystalline quality. This is desirable in nanotechnology applications.

1. Introduction

Zinc oxide (ZnO) is a commercially important material utilized in paints, rubber, catalysts, sensors, varistors, and so forth. ZnO exhibits semiconducting, piezoelectric, and pyroelectric properties [1, 2]. Nanostructured ZnO has a potential for application in nanotechnology [3, 4]. Structural, morphological, optical, and electrical properties of ZnO can be changed drastically by its doping with various metal cations [5]. Furthermore, ZnO thin films have recently been studied as an active channel material in thin film transistors [6, 7]. Chemically, ZnO is a simple compound; morphologically, however, this material is very rich in terms of the geometry of its particles. Many researchers focused on the investigation of the relationship between the synthesis route of ZnO on one side, due to their large exciton binding energy of ~ 60 meV at room temperature [8–13]. ZnO particles were largely prepared by using “wet” chemistry or pyrolysis, whereas the vacuum techniques prevailed in making thin ZnO films. The starting zinc compound, chemical composition of solvent, nature of the precipitating agent, pH, temperature, and time of aging influence the size and geometrical shape of ZnO particles [14].

In the past years, the ZnO micro/nanostructures with different shapes were synthesized by various approaches reported by many research groups. These methods include chemical vapor transport and condensation [15, 16], thermal evaporation [17], metal organic chemical vapor deposition [18], hydrothermal method [19], sol-gel method [20, 21], electrochemical deposition [22, 23], ion beam-assisted deposition [24], laser ablation [25], and sputter deposition [26].

In this study, ZnO rods were prepared by chemical spray pyrolysis technique. The spray pyrolysis is an attractive method to obtain thin films, since it has been proved to be a simple and inexpensive method and it is particularly useful for large area of nanotechnology applications. In addition, chemical spray pyrolysis has the advantage over the other methods in that it does not consume much time and is a cost-effective, catalyst, and template-free method to prepare ZnO nanostructures. Here, we report the direct growth of zinc oxide rods on glass substrate [27–30] by a chemical spray pyrolysis method. We have also studied the structural, morphological, and optical properties of the films with the aim of understanding physical properties of the obtained ZnO rods.

2. Experimental

ZnO rods were grown by a chemical spray pyrolysis technique. The spray solution was prepared dissolving ZnCl_2 (2.7256 g) in 200 mL distilled water. The initial pH value of solution was measured as 6. The starting solution was atomized at a frequency of 1.63 MHz by an ultrasonic nebulizer and by using dry air. The solution was mixed with magnetic mixer. Mixing process lasted for 30 min. The nozzle-substrate distance was maintained at 10 cm with 45 degree, and the substrate temperature was fixed at $\sim 550^\circ\text{C}$ by TET-612 temperature controller device on the metallic hot plate surface, because a flat ZnO film evolves into the structured layer consisting of single-crystalline hexagonal elongated prisms at growth temperatures close to $\sim 500^\circ\text{C}$ and above [27]. The temperature of the metallic plate surface was totally stable. The substrates are normal microscope glasses which were cut with the dimensions of $10 \times 10 \times 1$ mm. Before loading into the system, the substrates were washed with detergent and then completely rinsed in methanol, acetone, and deionized water, respectively, and dried in air. Then, the substrates were progressively heated up to the required temperature, before being sprayed on. At this temperature, it was observed that the glass substrate became soft. The 5-6 μm diameter droplets were carried onto heated glass substrates. The flow rate of air used as a carrier gas was 2 mL/min. The duration of the film deposition was about 100 min. The colour of ZnO film was white, and it had very good adhesion to glass substrates. The structural characterization of the films was carried out by X-ray diffraction (XRD) measurements using a Rigaku D/Max-IIIC diffractometer with $\text{CuK}\alpha 1$ radiation ($\lambda = 1.5418 \text{ \AA}$), at 30 kV, 10 mA. Surface morphology was examined by a JEOL JSM5610 model scanning electron microscope operating at 24 kV. The diameter and length of the rods were measured by a scanning electron microscope (SEM). In addition, morphology was also determined by atomic force microscopy (AFM). The optical characterization of the films was carried out by photoluminescence (PL) with an He-Cd ion laser as a light source using an excitation wavelength of 325 nm. So absorption coefficient was determined by UV-VIS absorption (UV) spectroscopy measurement.

3. Result and Discussion

3.1. Structural Properties. XRD patterns of the grown ZnO samples are shown in Figure 1. The diffraction pattern of grown sample shows a peak corresponding to (002) plane-reflection together with highly diminished peaks corresponding to other planes of wurtzite ZnO structure. The high intensity of (002) plane as compared with other planes clearly suggests the preferential growth of rods along the *c*-axis direction. The XRD pattern shows increase in the intensities of peaks due to reflections from all crystallographic planes of (100), (002), (101), (102), and (110) of wurtzite ZnO structure with predominant counts for (002) plane.

Taking SEM and AFM into consideration, we see that ZnO structures are spreading uniformly onto the sample surface, and vertically increasing from the axis *c* in Figures

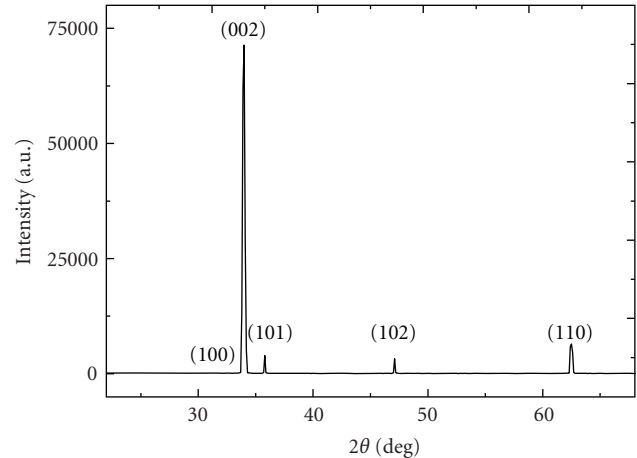
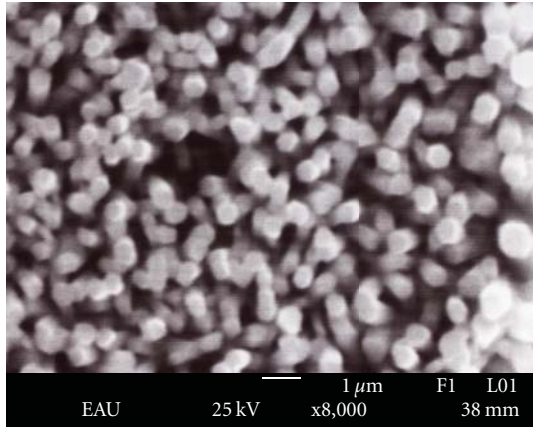


FIGURE 1: XRD pattern of ZnO rods deposited on glass substrate.

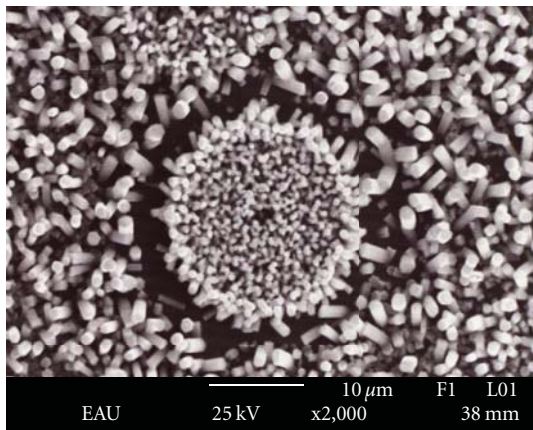
2 and 3. The length of the ZnO rods is between 500 and 2000 nm, and the diameter changes between 400 and 1000 nm. The diameter and length of the ZnO rods acquired by SEM were confirmed by graphs acquired by means of AFM. These cross-section graphics are important that the same length or diameter is achieved on the plane sample. AFM results are in compliance with the SEM investigation. Additionally, the reason of the sunflower-like structures in the SEM pictures is unknown, but we thought that the reason of these structures may be related to the temperature gradient on the glass substrates (Figure 2(b)).

3.2. Optical Properties. Figure 4(a) was acquired from the room temperature PL spectra of the synthesized ZnO rods. Two peaks are observed in this figure: exciton peak in the left side and donor-acceptor peak in the right side. Figure 4(b) was acquired from the cryogenic PL spectra. Two peaks are observed in the spectrum at 6.2 K: one is a strong, dominated, and high-intensity peak at 3680 \AA in the UV region; the other is a suppressed and weak band at 5500 \AA in the visible region.

The UV emission is also called as near-band edge emission and originated by the recombination of the free excitons. The green band in the visible region, known as deep level emission, is generally explained by the radiative recombination of the photo-generated hole with the electrons which belong to ionized oxygen vacancies [31]. In our case, the UV emission is dominated over the green level emission. The weak peak is a result of donor acceptor pairs (DAPs) which can cause emission at room temperature. These DAPs are made up of dislocations or impurity in crystal. In general, the UV peak at room temperature is attributed to near band-edge (NBE) free exciton transition from the localized level below the conduction band to the valance band [32]. The emissions which are produced by DAP are decreasing by the temperature decrease because activity is decreasing by the temperature. The sharply peak is made up of exciton doublets which are not decomposed at the room temperature. According to PL data which is obtained in 6.2 K, the sharp peaks' duration increases at



(a)



(b)

FIGURE 2: SEM images of ZnO rods. (a) Hexagonal ZnO nanorods. (b) The result from temperature gradient-dependent structure deformation.

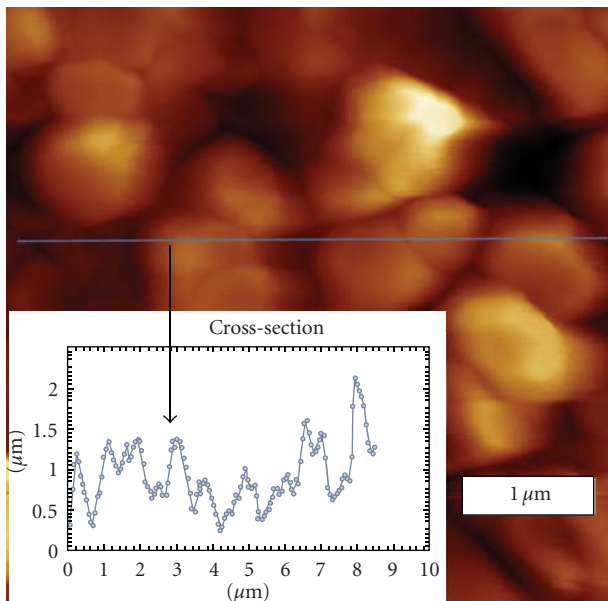
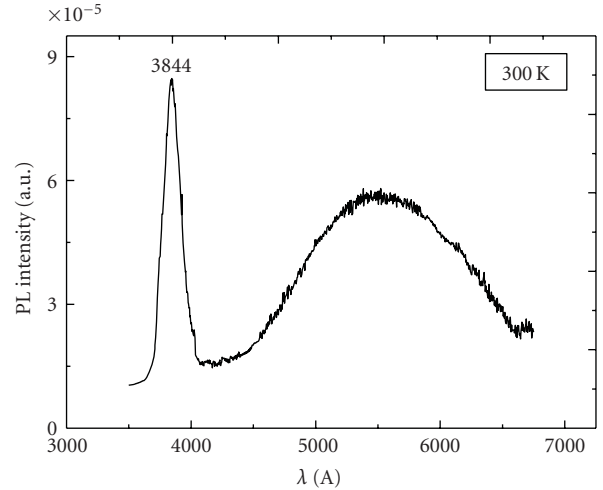
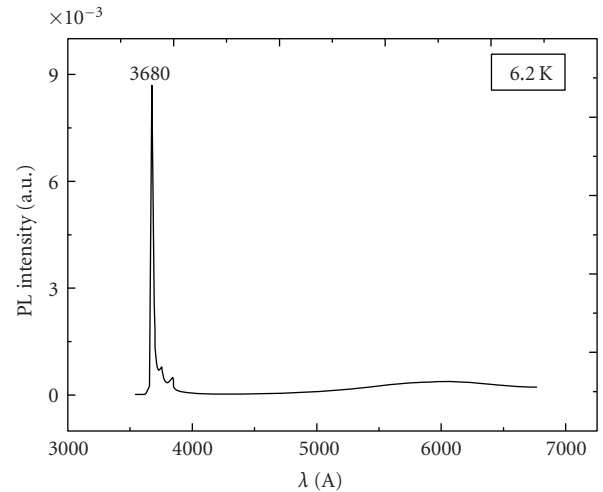


FIGURE 3: AFM image and cross-section graphic of the ZnO rods.



(a)



(b)

FIGURE 4: PL spectra of ZnO rods at (a) 300 K and (b) 6.2 K.

temperature decrease, so peak intensity increases and slides to the left side because decrement of temperature widens the band gap. The other peak seems like decreasing because of the increase of sharp peaks' intensity. It has been reported that the improvement in the crystal quality such as low structural defects, oxygen vacancies, zinc interstitials, and decrease in the impurities may cause the appearance of a sharp and strong UV emission and a suppressed and weak green emission [33]. So the presence of a strong UV emission and a weak green emission from the synthesized ZnO rods indicated that the grown structures have good crystal quality with less structural defects [34]. The absorption coefficient is one of the intrinsic parameters of the ZnO rods that was determined by fitting the absorption spectrum with an appropriate Beer-Lambert Law. The thickness of the ZnO rods was verified by the cross-section graphic of the AFM (Figure 3) and SEM images (Figure 2). The value of the energy and absorption coefficient calculation was carried out for the ZnO rods. It was found that the value of the energy is

3.35 eV and the absorption coefficient is 145125 cm^{-1} for the largest peak.

4. Conclusion

In this study, the ZnO rods on glass substrate were obtained by the ultrasonic spray pyrolysis method. The microstructures of ZnO rods were characterized by SEM, AFM images, and XRD patterns. Optical properties were obtained by PL spectrometer and UV-Vis measurements. Sharp near-band edge (NBE) emission peaks centered at 3844 and 3680 Å dominated the PL spectra of ZnO at 300 K and 6.2 K, respectively. In addition, structural analysis showed that the rods are *c*-axis-orientated ZnO wurzite crystals. The ZnO rods produced at optimum substrate temperature of $\sim 550^\circ\text{C}$ exhibited single phase of ZnO with preferred (002) orientation. Diameter and length of size ZnO rods were 500–2000 and 400–2000 nm, respectively. It was found that ZnO rods with good structural and morphological properties can be produced on glass. These results indicate that spray pyrolysis methods are a viable technique for producing high-quality ZnO rods for optical devices. At the same time, it is important to discuss the implementation of the presented results in this study for optoelectronic applications. The main issue in nanotechnology is to get devices in small size. The present work will contribute to the understanding of related photoluminescence, optical, structural, and morphological properties of ZnO nanomaterials.

References

- [1] Z. L. Wang, "Nanostructures of zinc oxide," *Materials Today*, vol. 7, no. 6, pp. 26–33, 2004.
- [2] N. Tamaekong, C. Liewhiran, A. Wisitsoraat, and S. Phanichphant, "Flame-spray-made undoped zinc oxide films for gas sensing applications," *Sensors*, vol. 10, no. 8, pp. 7863–7873, 2010.
- [3] Y. H. Heo, D. P. Norton, L. C. Tien et al., "Low temperature ($< 100^\circ\text{C}$) patterned growth of ZnO nanorod arrays on Si," *Materials Science and Engineering R-Reports*, vol. 47, no. 1–2, pp. 1–47, 2004.
- [4] M. J. Height, L. Madler, S. E. Pratsinis, and F. Krumeich, "Nanorods of ZnO made by flame spray pyrolysis," *Chemistry of Materials*, vol. 18, no. 2, pp. 572–578, 2006.
- [5] D. P. Norton, Y. W. Heo, M. P. Ivill et al., "ZnO: growth, doping & processing," *Materials Today*, vol. 7, no. 6, pp. 34–40, 2004.
- [6] E. Fortunato, P. Barquinha, A. Pimentel et al., "Recent advances in ZnO transparent thin film transistors," *Thin Solid Films*, vol. 487, no. 1–2, pp. 205–211, 2005.
- [7] E. Fortunato, P. Barquinha, A. Pimentel et al., "Fully transparent ZnO thin-film transistor produced at room temperature," *Advanced Materials*, vol. 17, no. 5, pp. 590–594, 2005.
- [8] S. Choopun, R. D. Vispute, W. Noch et al., "Oxygen pressure-tuned epitaxy and optoelectronic properties of laser-deposited ZnO films on sapphire," *Applied Physics Letters*, vol. 75, no. 25, pp. 3947–3949, 1999.
- [9] Y. Li, G. W. Meng, L. D. Zhang, and F. Phillipp, "Ordered semiconductor ZnO nanowire arrays and their photoluminescence properties," *Applied Physics Letters*, vol. 76, no. 15, pp. 2011–2014, 2000.
- [10] L. Guo, S. Yang, C. Yang et al., "Highly monodisperse polymer-capped ZnO nanoparticles: preparation and optical properties," *Applied Physics Letters*, vol. 76, no. 20, pp. 2901–2903, 2000.
- [11] R. Wu, C. Xie, H. Xia, J. Hu, and A. Wang, "The thermal physical formation of ZnO nanoparticles and their morphology," *Journal of Crystal Growth*, vol. 217, no. 3, pp. 274–280, 2000.
- [12] Y. Lia, X. L. Chen, H. Li, M. He, and Z. Y. Qiao, "Fabrication of zinc oxide nanorods," *Journal of Crystal Growth*, vol. 233, no. 1–2, pp. 5–7, 2001.
- [13] B. K. Meyer, H. Alves, D. M. Hofmann et al., "Bound excitation and donor-acceptor pair recombination ZnO," *Physica Status Solidi B*, vol. 241, no. 2, pp. 231–260, 2004.
- [14] S. Music, A. Saric, and S. Popovic, "Dependence of the microstructural properties of ZnO particles on their synthesis," *Journal of Alloys and Compounds*, vol. 448, no. 1–2, pp. 277–283, 2008.
- [15] K. Keis, E. Magnusson, H. Lindstrom, S. E. Lindquist, and A. Hagfeldt, "A 5% efficient photoelectrochemical solar cell based on nanostructured ZnO electrodes," *Solar Energy Materials and Solar Cells*, vol. 73, no. 1, pp. 51–58, 2002.
- [16] D. Voss, "Condensed-matter physics: switch-hitter materials tantalize theorists," *Science*, vol. 292, no. 5524, pp. 1987–1990, 2001.
- [17] M. H. Huang, Y. Wu, H. Feick, N. Tran, E. Weber, and P. Yang, "Catalytic growth of zinc oxide nanowires by vapor transport," *Advanced Materials*, vol. 13, no. 2, pp. 113–116, 2001.
- [18] W. Lee, M. C. Jeong, and J. M. Myoung, "Catalyst-free growth of ZnO nanowires by metal-organic chemical vapour deposition (MOCVD) and thermal evaporation," *Acta Materialia*, vol. 52, no. 13, pp. 3949–3957, 2004.
- [19] Z. R. Dai, Z. W. Pan, and Z. L. Wang, "Novel nanostructures of functional oxides synthesized by thermal evaporation," *Advanced Functional Materials*, vol. 13, no. 1, pp. 9–24, 2003.
- [20] L. E. Greene, M. Law, J. Goldberger et al., "Low-temperature wafer-scale production of ZnO nanowire arrays," *Angewandte Chemie—International Edition*, vol. 42, no. 26, pp. 3031–3034, 2003.
- [21] S. E. Ahn, J. S. Lee, H. Kim et al., "Photoresponse of sol-gel-synthesized ZnO nanorods," *Applied Physics Letters*, vol. 84, no. 975, pp. 5022–5024, 2004.
- [22] Y. C. Wang and M. H. Hon, "Preparation of nanosized ZnO arrays by electrophoretic deposition," *Electrochemical and Solid-State Letters*, vol. 5, no. 4, pp. C53–C55, 2002.
- [23] M. J. Zheng, "Fabrication and optical properties of large-scale uniform zinc oxide nanowire arrays by one-step electrochemical deposition technique," *Chemical Physics Letters*, vol. 363, no. 1–2, pp. 123–128, 2002.
- [24] W. Li, D. S. Mao, Z. H. Zheng et al., "ZnO/Zn phosphor thin films prepared by IBED," *Surface and Coatings Technology*, vol. 128–129, no. 1, pp. 346–350, 2000.
- [25] Y. Sun, G. M. Fuge, and M. N. R. Ashfold, "ZnO/Zn phosphor thin films prepared by IBED," *Chemical Physics Letters*, vol. 396, no. 1–3, pp. 21–26, 2004.
- [26] W. Chiou, W. Wu, and J. Ting, "Growth of single crystal ZnO nanowires using sputter deposition," *Diamond and Related Materials*, vol. 12, no. 10–11, pp. 1841–1844, 2003.
- [27] U. Alver, T. Kilinc, E. Bacaksiz et al., "Synthesis and characterization of spray pyrolysis Zinc Oxide microrods," *Thin Solid Films*, vol. 515, no. 7–8, pp. 3448–3451, 2007.
- [28] V. V. Kireev, L. N. Dem'yanets, L. E. Li, and V. V. Artemov, "Growth of thin ZnO films by ultrasonic spray pyrolysis," *Inorganic Materials*, vol. 46, no. 2, pp. 154–162, 2010.

- [29] A. Khoury, R. al Asmar, M. Abdallah, G. El Hajj Moussa, and A. Foucaran, "Comparative study between zinc oxide elaborated by spray pyrolysis, electron beam evaporation and rf magnetron techniques," *Physica Status Solidi A*, vol. 207, no. 8, pp. 1900–1904, 2010.
- [30] Z. L. Wang, "Zinc oxide nanostructures: growth, properties and applications," *Journal of Physics Condensed Matter*, vol. 16, no. 16, pp. R829–R858, 2004.
- [31] K. Vanheusden, C. H. Seager, W. L. Warren, D. R. Tallant, and J. A. Voigt, "Mechanisms behind green photoluminescence in ZnO phosphor powders," *Journal of Applied Physics*, vol. 79, no. 10, pp. 7983–7990, 1996.
- [32] S. Cho, J. Ma, Y. Kim, Y. Sun, G. K. L. Wong, and J. B. Ketterson, "Photoluminescence and ultraviolet lasing of polycrystalline ZnO thin films prepared by the oxidation of the metallic Zn," *Applied Physics Letters*, vol. 75, no. 18, pp. 2761–2763, 1999.
- [33] D. M. Bagnall, Y. F. Chen, Z. Zhu, T. Yao, M. Y. Shen, and T. Goto, "High temperature excitonic stimulated emission from ZnO epitaxial layers," *Applied Physics Letters*, vol. 73, no. 8, pp. 1038–1042, 1998.
- [34] A. Umar, S. H. Kim, Y.-S. Lee, K. S. Nahm, and Y. B. Hahn, "Catalyst-free large-quantity synthesis of ZnO nanorods by a vapor-solid growth mechanism: structural and optical properties," *Journal of Crystal Growth*, vol. 282, no. 1-2, pp. 131–136, 2005.